NUMERICAL MODELING AND OPTIMIZATION OF OPEN-OCEAN AERATION SYSTEMS

by

Jonathan Totten

Submitted in partial fulfillment of the requirements
for the degree of Master of Applied Science

at

Dalhousie University
Halifax, Nova Scotia
April 2018

For Crackle and Stallone

Table of Contents

List of Tables

List of Figures

ix

Abstract

The coastal regions of Nova Scotia are prone to warmer ocean temperatures resulting in lower dissolved oxygen (DO) levels during the summer months. DO levels below 6 mg/L lead to reduced feed conversion, growth, and welfare of Atlantic salmon in open-ocean pens. An aeration system that allows for the delivery of supplemental oxygen to open-ocean aquaculture pens during conditions of low DO has the potential to improve key performance indicators of Atlantic salmon. A transient one-dimensional bubble plume model coupled with an ambient environment model was developed and validated using hydrodynamic and mass transfer case studies. The model was used to develop heuristics for the number of diffusers, spacing of diffusers, and the volume of air and oxygen-enriched air to maintain DO levels above the recommended minimum of 6 mg/L. Six trilobed diffusers using air are required to maintain the DO in an open-ocean pen above 6 mg/L.

List of Abbreviations and Symbols Used

Abbreviations

Ar	Argon
CO_2	Carbon dioxide
CFD	Computational fluid dynamics
DO	Dissolved oxygen
DN	Dissolved nitrogen
O_2	Oxygen
ODEs	Ordinary differential equations
N_2	Nitrogen

Symbols

A_b	Bubble interfacial area	m^2
A_s	Cross-sectional area	m^2
a	Ratio of the air-water interfacial area to volume	m^{-1}
B	Buoyancy	$kg\ m\ s^{-1}$
C_a	Concentration of dissolved gas in the ambient water	mol/m^3
C_i	Concentration of dissolved gas in the plume water	mol/m^3
C_p	Plume O_2 concentration being detrained	mol/m^3
C_d	Drag coefficient	-
C^*	Saturation concentration	mol/m^3
D_i	Diffusivity	m^2/s
DO_{avg}	Volume averaged DO concentration	mol/m^3
DO_{fish}	Oxygen consumption rate by Atlantic salmon	mol/s
d_b	Bubble diameter	m
d_h	Hydraulic diameter	m
E_c	Aerator energy cost	$/h
E_r	Electricity rate	$/kWh
F_p	Pressure factor	-
Fr	Froude number	-

F_s	Salinity factor	-
f	Friction factor	-
g	Acceleration due to gravity	m/s^2
g'	Reduced gravity	m/s^2
h	Convective heat transfer coefficient	W m^{-2} K^{-1}
H	Height above diffuser	m
H_d	Pressure depth	m
K	Henry's law constant	mol m^3 Pa^{-1}
k	Convective liquid-film mass transfer coefficient	m/s
L	Pipe length	m
M	Momentum	m^4/s^2
MW	Molecular weight	g/mol
m_g	Total mass of gaseous species	kg
$\dot{m}$	Mass flow rate of gas	kg/s
N	Number of diffusers	-
$\dot{N}$	Species molar flow rate	mol/s
N_b	Number of bubbles	s^{-1}
Nu	Nusselt number	-
n	Polytropic exponent	-
$\dot{n}$	Molar gas flow rate	mol/s
n_E	Number of plume function horizontal slices	-
n_Z	Number of ambient function horizontal slices	-
OTR	Oxygen transfer rate	kgO$_2$/h
P	Total pressure	Pa
P_d	Diffuser pressure pipe	Pa
P_i	Partial pressure	Pa
P_p	Pipe pressure drop	Pa
P_w	Vapour pressure of water	Pa
Pr	Prandtl number	-
P^*	Dimensionless pressure	-
Q	Liquid volumetric flow	m^3/s

q_d	Detrainment	m^2/s
q_e	Entrainment	m^2/s
R	Universal gas constant	$m^3\ Pa\ K^{-1}\ mol^{-1}$
Re	Reynolds number	-
R_{pen}	Open-ocean pen radius	m
R_p	Aeration radius	m
r	Radius	m
S	Salinity	g/kg
Sc	Schmidt number	-
Sh	Sherwood number	-
SAE	Standard aeration efficiency	kgO_2/kWh
T	Temperature	K
T^*	Dimensionless temperature	-
t	Time	s
u	Centerline plume velocity	m/s
u_e	Entrainment velocity	m/s
u_t	Bubble terminal velocity	m/s
u_t^*	Swarm corrected bubble terminal velocity	m/s
V	Aeration volume	m^3
$\dot{V}$	Gas volumetric flow	m^3/s
V_b	Bubble volume	m^3
W	Fish body weight	g
$\dot{W}$	Power	kW
y	Gas phase composition	mol
Z	Compressibility factor	-

Greek Letters

α	Entrainment coefficient	-
β	Entrainment coefficient dimensionless parameter	-
γ	Momentum amplification factor	-
ε	Gas phase fraction or pipe roughness	m^3 gas/m^3 total or m
η	Compressor efficiency	-

κ	Thermal conductivity	W m^{-1} K^{-1}
λ	Width between momentum and buoyancy profiles	-
μ	Viscosity	Pa s
ρ	Density	kg/m^3

Subscripts

O_2	Oxygen
N_2	Nitrogen
0	Source
a	Ambient
b	Bubble
c	Current
g	Gas
i	Dispersed phase
I	Individual
j	Continuous phase
l	Liquid
L	Loss
p	Plume
t	Total
w	Water
end	Time integration end
$start$	Time integration start
std	Standard conditions
sw	Seawater

Acknowledgments

First, I would like to thank my supervisors, Dr. Adam Donaldson and Dr. Jan Haelssig, for all their support and guidance over the course of the project.

I would also like to thank my committee members, Dr. Stephen Kuzak and Dr. Dominic Groulx, for reviewing the thesis and providing insightful feedback and advice.

Finally, I would like to thank my family, friends, and wife, Stephanie, for their love and support.

Chapter 1: Introduction

1.1 Socio-Economic Impact of Aquaculture

The oceans of the world were once considered sources of unlimited food supply as they cover approximately 71% of the earth's surface with a maximum sustainable yield of wild marine species of 100 billion kilograms per year (Lawson, 2012). The limits for sustainable harvesting of wild resources in these bodies of water is rapidly approaching as the world's population continues to grow. It is predicted that by the year 2030, the world's population will increase from 7.6 to 8.5 billion (United Nations, 2015). At this alarming growth rate, the world's population will exceed its capacity for food production. The United Nations Food and Agriculture Organization forecasts a global seafood shortage of 50 to 80 billion kilograms by 2030 (RSPCA, 2017). A solution to the growing food shortage is controlled aquaculture. Controlled aquaculture production is the most rapidly expanding food industry in the world that can ensure a steady and regular supply of food to the growing population (Lawson, 2012). The Atlantic salmon aquaculture industry is the leader in finfish production with a worldwide production in 2016 exceeding one billion kilograms per year. The largest producers of Atlantic salmon are Norway, Chile, Scotland, and Canada. Canada is currently the fourth largest producer of farmed Atlantic salmon in the world, producing 170 million kilograms with the Atlantic provinces accounting for approximately 40% of this in 2016 (Gardner Pinfold, 2016). Annual global production of Atlantic salmon through aquaculture production has grown dramatically from 1980 to 2016 (Figure 1.1) from 5.28 million kilograms to 2.33 billion kilograms, as a result of the decreased costs of controlled Atlantic salmon aquaculture compared to that of catching wild stock (FAO, 2017).
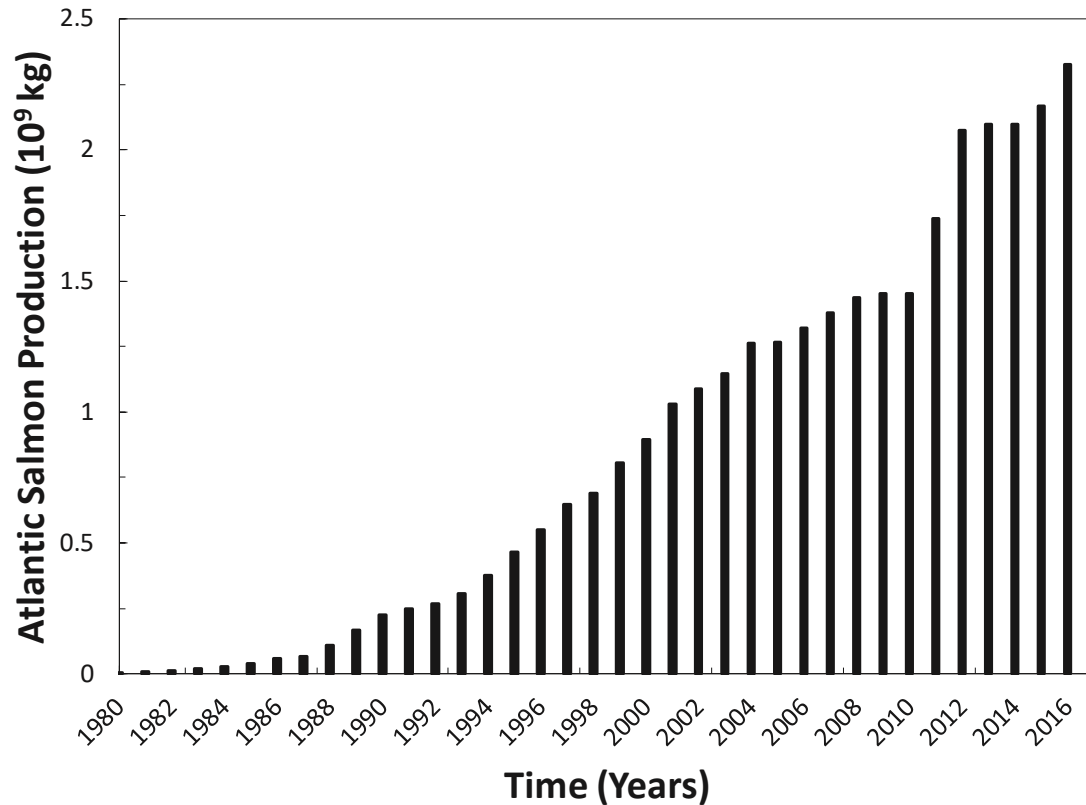
Figure 1.1: Yearly global aquaculture production of Atlantic salmon in billion kilograms from 1980 to 2016 (FAO, 2017)

Aquaculture in Nova Scotia is an established, environmentally sound and growing industry consisting of 44 companies that contribute approximately $60 million CAD per year to the local economy (Department of Fisheries & Aquaculture, 2017). The aquaculture industry in Nova Scotia is also becoming an increasingly important economic contributor to rural regions in the province, employing over 600 Nova Scotians (Department of Fisheries & Aquaculture, 2017). The Atlantic salmon and rainbow trout production in 2014 accounted for 82% of the Nova Scotian aquaculture production, resulting in 6.8 million kg and $50 million CAD (Department of Fisheries & Aquaculture, 2017). However, one of the main challenges faced by the industry is related to the seasonal fluctuations that alter dissolved oxygen (DO) levels in the aquaculture pens. The number of marine and land-based aquaculture farms in Nova Scotia is illustrated in Figure 1.2.
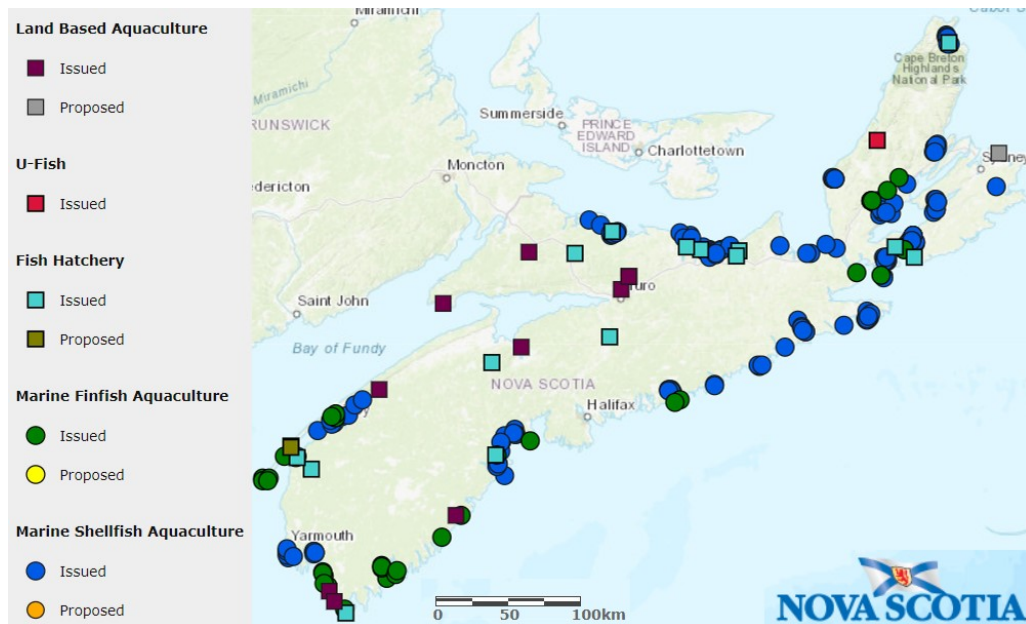
Figure 1.2: Land based and marine aquaculture farms in Nova Scotia (Department of Fisheries & Aquaculture, 2017)

1.2 Lifecycle of Atlantic Salmon

Atlantic salmon (*Salmo salar*) is an anadromous species and native to the Atlantic Ocean (RSPCA, 2017). In Atlantic salmon farming, the lifecycle of the fish begins with the laying of eggs in the hatchery during the early winter months. Eggs are harvested from broodstock (mature salmon), fertilized, and then incubated (RSPCA, 2017; Bergheim & Fivelstad, 2014). Depending on water temperature during incubation, the eggs hatch between 40 and 80 days. The newly hatched salmon, referred to as alevin (2 to 6 months), absorb nutrients from a yolk sac attached to their bodies. It is not until the yolk sac has been absorbed that the fish, now called fry, is ready to eat a formulated diet. At this stage, the fry are transferred to small tanks where they grow into parr (juvenile salmon with characteristic stripes). As the parr continue to grow, they are transferred to larger tanks where they remain for 8 to 12 months in fresh water. When the parr reach a body weight between 80 and 150 g (or when the parr have lost their characteristic stripes), the fish, now called smolts (young adults), are ready to be transferred to seawater (RSPCA, 2017; Bergheim & Fivelstad, 2014). The salmon continue to grow in the saltwater environment where they remain until they are ready for harvest approximately 14 to 18 months from the time they entered the ocean. At this time, the average weight of each fish is around 5 kg. In Atlantic salmon

aquaculture, the fish spend 10 to 16 months in fresh water, plus 14 to 18 months in the open-ocean pens before they are ready for harvest (RSPCA, 2017; Bergheim & Fivelstad, 2014). The life cycle of the Atlantic salmon from eggs to broodstock is illustrated in Figure 1.3.
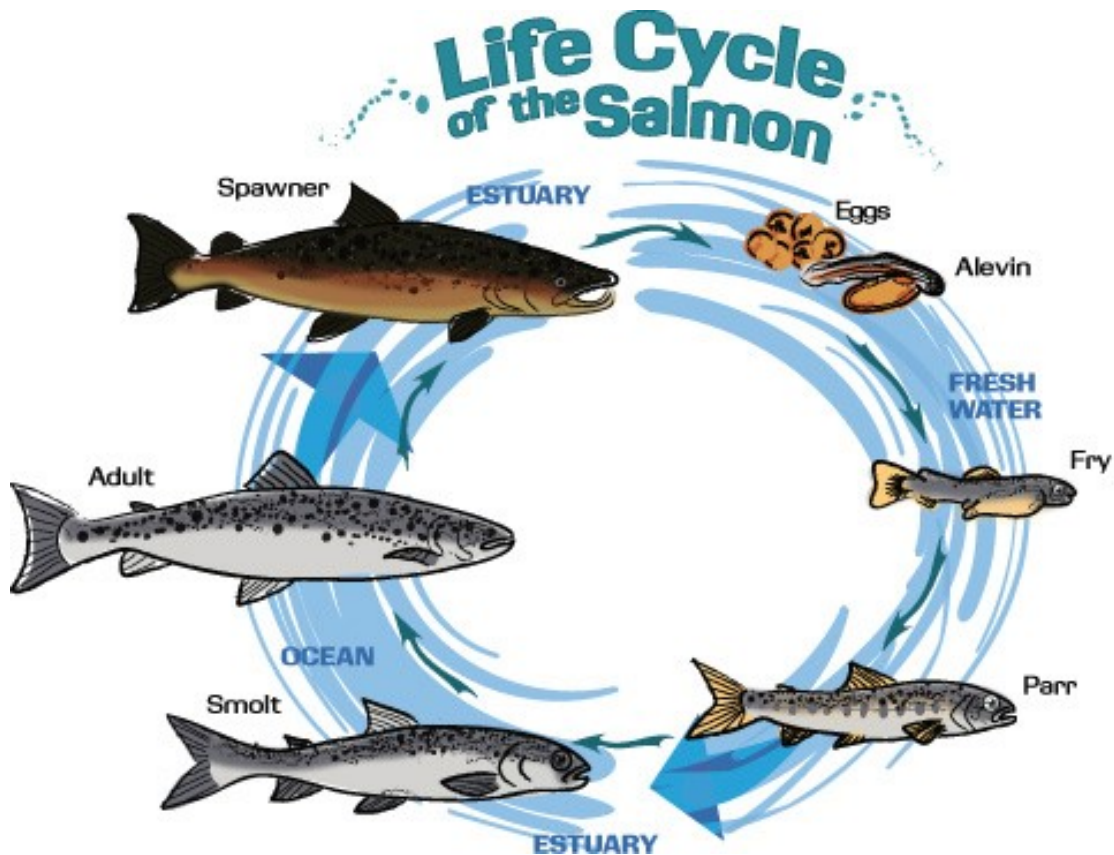
Figure 1.3: The life cycle of the Atlantic salmon from eggs to broodstock (University of California, 2018)

1.3 Atlantic Salmon Aquaculture Methods

Atlantic salmon aquaculture systems are diverse in their design and function. The two most basic categories are closed systems and open-systems. Closed-system aquaculture methods are used to control the exchange between farms and the natural environment and take place in tanks on land (Lawson, 2012). One type of closed aquaculture method for Atlantic salmon is a recirculating system, in which the water is circulated through biofiltration units to remove toxic materials and regulate the water quality for the Atlantic salmon (Lawson, 2012). Land-based salmon farming continues to evolve and is commonly used for

hatcheries but remains an economically unviable method for raising post-smolt Atlantic salmon. Therefore, open-systems are the dominant methods of salmon farming (RSPCA, 2017). Open-systems are found offshore in coastal areas or freshwater lakes and allow for free and unregulated exchange of ocean waters with Atlantic salmon (Lawson, 2012). Open-ocean aquaculture is an approach to Atlantic salmon farming in which the pens are moved some distance offshore and positioned in deeper and less sheltered waters. Open-ocean aquaculture systems have an advantage over closed systems because there is a constant supply of DO from water exchange with the ocean current and air diffusion through the air-water interface at the surface (Oppedal, Dempster, & Stien, 2011). However, during times of warmer ocean temperatures and stagnant water circulation, there is no longer a constant supply of DO (i.e. open-ocean aquaculture systems are no longer an advantage). In 2014 open-ocean pens accounted for over 90% of the salmon farming in Nova Scotia (Department of Fisheries & Aquaculture, 2017). A typical open-ocean aquaculture pen containing Atlantic salmon is illustrated in Figure 1.4.
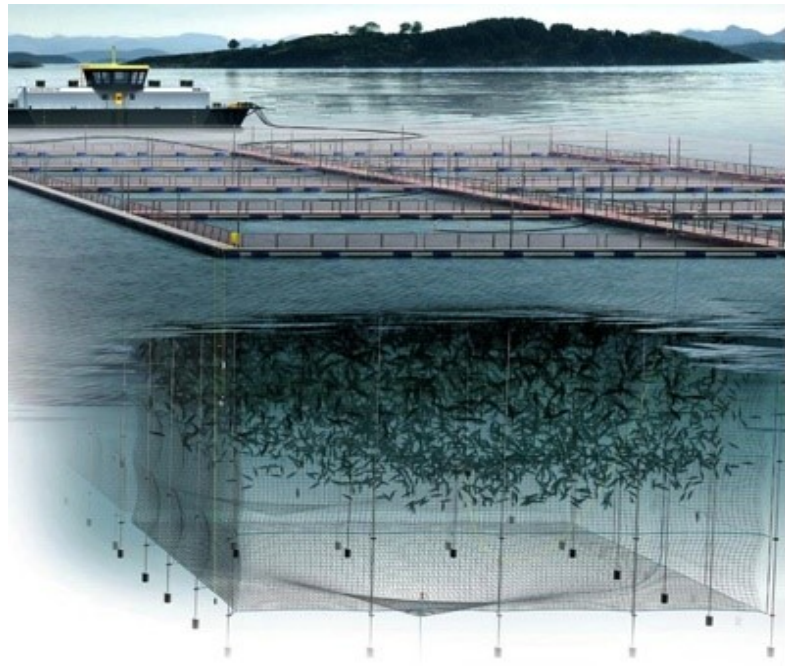
Figure 1.4: Open-ocean aquaculture pen with Atlantic salmon (FAO, 2017)

Open-ocean pens are typically either square pens between 20 and 40 m wide and up to 35 m deep, or circular pens between 90 and 157 m in diameter and up to 48 m deep. Square

pens are arranged in clusters ranging from 4 to 28 pens separated by 2 to 4 m, while circular pens are arranged in rows with spacing up to 20 m between pens (Oppedal et al., 2011).

1.4 Current Issues in Atlantic Salmon Open-Ocean Aquaculture

In Canada, Atlantic salmon can be stocked in open-ocean aquaculture pens up to a recommended stocking density of 25 kg/m^3; however, schooling of Atlantic salmon leads to zones where the density is 1.5 to 5 times the stocking density (Oppedal et al., 2011). As a result, the Atlantic salmon must compete for resources such as DO. Adequate DO concentration is a prerequisite for the welfare, development, and health of Atlantic salmon in open-ocean pens. Low DO levels can lead to increased stress, causing decreased growth rates, reduced feed conversion ratios, increased susceptibility to disease, and in extreme cases, mortality due to suffocation (Berillis et al., 2016). A study produced by Fisheries Research Services (2005) found that between 2000 and 2003, 22% of post-smolt Atlantic salmon died prematurely due to disease and O_2 starvation. Therefore, maintaining optimal DO concentration is essential to the production and efficiency of aquaculture farms.

Recent publications have revealed that the DO concentration of the water in open-ocean Atlantic salmon pens fluctuates substantially, both temporally due to complex tidal, diurnal, and seasonal variations and spatially due to ocean currents and other aquatic species (Berillis et al., 2016). Additionally, the concentration of DO in water, which is required to meet the metabolic demands of Atlantic salmon, depends on a range of factors that affect the total energy expenditure of the fish. The metabolic rate of Atlantic salmon is known to increase with temperature, feeding level, swimming speed, and stress. The suggested minimum DO for the growth of Atlantic salmon is 6 mg/L (Oppedal et al., 2011), implying there are periods of fluctuation in which DO concentration is too low to maintain optimal growth, and that the most severe reductions in O_2 may compromise basic function and survival. Temperature and salinity are closely correlated with DO concentration (Oppedal et al., 2011), and as the temperature and salinity of the ocean water increases, the capacity for oxygenation decreases. The saturated (or maximum achievable) DO concentration (mg/L) for air in water at temperatures ranging from 0 to 25°C and salinities

of 0 and 30 g/kg are illustrated in Figure 1.5 in comparison to the minimum DO for the growth of Atlantic salmon.
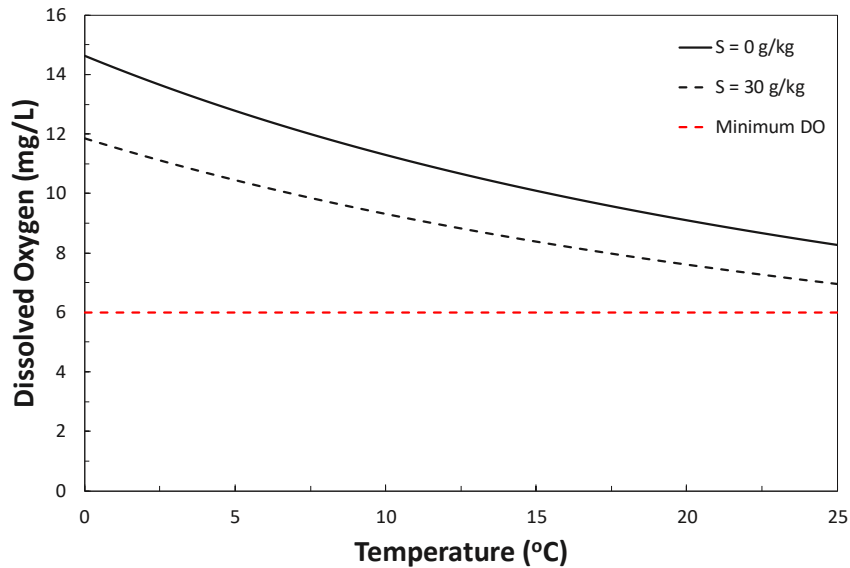
Figure 1.5: DO concentration at saturation for air at temperatures ranging between 0 and 25°C and salinities of 0 and 30 g/kg. Derived from correlations of Benson and Krause (1980) and Benson and Krause (1984).

The coastal regions of Atlantic Canada, and more specifically Nova Scotia, are prone to natural fluctuations in both water temperature and O_2 levels, leading to negative consequences for the health and growth of Atlantic salmon. The reduced DO levels lead to an elevated risk in late summer when temperatures are highest, particularly at night when photosynthetic O_2 production is dormant. Average temperatures off the south shore of Nova Scotia between 2012 and 2017 for July, August, and September were 16.2°C, 17.1°C, and 19°C respectively (NOAA, 2018). Additionally, Atlantic salmon preferentially migrate to warmer water temperatures between 16 and 18°C, even if such zones are deficient in DO. The preference for warmer water and the tendency of Atlantic salmon to form schools, creates a compounding effect that further leads to deficient zones of DO. The rising ocean temperatures and increasing climate change are expected to exacerbate the problem of fluctuating DO levels, creating a need for strategies to mitigate the low DO conditions in highly dense open-ocean salmon farming.

Aeration is a common practice in land-based aquaculture to deliver supplemental O_2 but is less common in open-ocean pens where natural processes regulate DO through exchange with ocean waters. An aeration system that allows for the delivery of supplemental O_2 to open-ocean pens on demand during conditions of low DO has the potential to improve key performance indicators significantly. Improving key performance indicators will reduce episodic stress and mortality caused by low O_2 (Berillis et al., 2016), and increase production efficiency, stability, and environmental sustainability of the aquaculture industry in Nova Scotia. Current literature is lacking heuristics for aerator placement and operation in open-ocean aquaculture systems. Detailed models and heuristics are needed to facilitate the design of aeration systems that include predictions of O_2 uptake from multiple aerators. The detailed models and heuristics are required to estimate the O_2 transfer efficiency from the bubble to the liquid and to characterize the effect of different gas feeds such as air and O_2-enriched air on overall aeration system performance.

1.5 Thesis Objectives

The purpose of this dissertation is to develop heuristics for the aeration in Atlantic salmon open-ocean aquaculture pens during times of low DO (i.e., below 6 mg/L). The purpose of the dissertation will be accomplished through the following objectives.

1. Identify key performance indicators to characterize the beneficial effects of O_2 supplementation for Atlantic salmon and parameters that will affect DO concentration in open-ocean pens.

2. Evaluate technical approaches for efficiently distributing DO to open-ocean aquaculture pens.

3. Develop a detailed model that can predict the hydrodynamics and mass transfer of O_2 from bubble plumes generated by diffusers and validate the hydrodynamics and mass transfer using representative data.

4. Determine best methods to efficiently deliver DO through the timing of aeration, the optimal spacing of diffusers, the number of diffusers required, and the use of air or O_2-enriched air through detailed modeling.

It is proposed that a transient one-dimensional bubble plume model coupled with an ambient environment mixing model will be sufficiently accurate to develop heuristics for the aeration in Atlantic salmon open-ocean aquaculture pens during times of low DO. The model will be able to predict the number of diffusers, the placement of diffusers, and the volume of air or O_2-enriched air required to keep the DO concentration in Atlantic salmon open-ocean pens above the recommended minimum of 6 mg/L. The remaining chapters in this dissertation test this general hypothesis through investigation and detailed modeling of open-ocean pen aeration systems. The following section provides an overview of the organization of this dissertation.

1.6 Thesis Structure

Several case studies were performed in this thesis to investigate and optimize the delivery of DO to open-ocean aquaculture pens. To organize these case studies, this dissertation has been divided into five chapters. The first half of Chapter 2 provides a review of relevant background information related to open-ocean aquaculture and identifies the key performance indicators that characterize the beneficial effects of O_2 supplementation for Atlantic salmon and the parameters that will affect DO concentration in open-ocean pens. The second half of Chapter 2 evaluates the different technological methods available for aeration in open-ocean pens and the current recommended practices for aerating in open-ocean pens. Chapter 3 describes a detailed modeling approach for a transient one-dimensional bubble plume model using the integral method coupled with an ambient environment mixing and transport model. The model is tuned and validated using experimental hydrodynamic and mass transfer plume data from the literature, and solved using a novel method. Chapter 4 provides a detailed case study of an open-ocean aquaculture pen. The number of diffusers required, the spacing required between the diffusers, and the required air and O_2-enriched air flow rate are investigated using the coupled integral model from Chapter 3. Chapter 5 presents a summary of the major conclusions and contributions resulting from these studies, along with some recommendations.

Chapter 2: DO Dynamics in Open-Ocean Aquaculture

2.1 Introduction

The level of DO in seawater depends on (1) the O_2 input from the atmosphere and photosynthesis by aquatic plants, algae, and some bacteria, (2) the biological O_2 consumption (e.g. bacteria, algae, and fish), (3) the vertical and horizontal mixing of water, and (4) the solubility of O_2, which increases with barometric pressure, and decreases with temperature and salinity (Lawson, 2012). The atmosphere is composed of 21.0% O_2, 78.0% nitrogen (N_2), 0.9% argon (Ar), 0.04% carbon dioxide (CO_2), and the remainder is trace amounts of other gases. Atmospheric O_2 enters the water by diffusion associated with physical agitation of the surface water. The diffusion of atmospheric O_2 into surface waters is extremely slow; therefore, O_2 production by photosynthesis in aquatic plants and organisms is the primary source of DO in open-ocean pens (Lawson, 2012). Photosynthesis in an aquaculture pen is fueled by light energy from the sun (Eq. 2.1).

$$6CO_2 + 6H_2O \xrightarrow{Sunlight\ Energy} C_6H_{12}O_6 + 6O_2 \qquad (2.1)$$
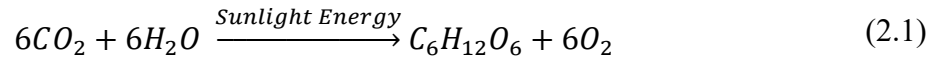
where CO_2 and H_2O react with light energy from the sun to form glucose and O_2. Chlorophyll-bearing aquatic organisms such as submerged plants, phytoplankton, and photosynthetic bacteria transfer O_2 into seawater if sunlight is available (Lawson, 2012). The chlorophyll-bearing aquatic organisms are also responsible for producing a unique 24-hour period of O_2 (Figure 2.1) called the diel cycle. During the 24-hour period the O_2 concentration is lowest at sunrise before photosynthesis begins, the O_2 concentration increases during the daylight hours to a peak concentration in the late afternoon, and finally the O_2 concentration declines at night (Lawson, 2012).
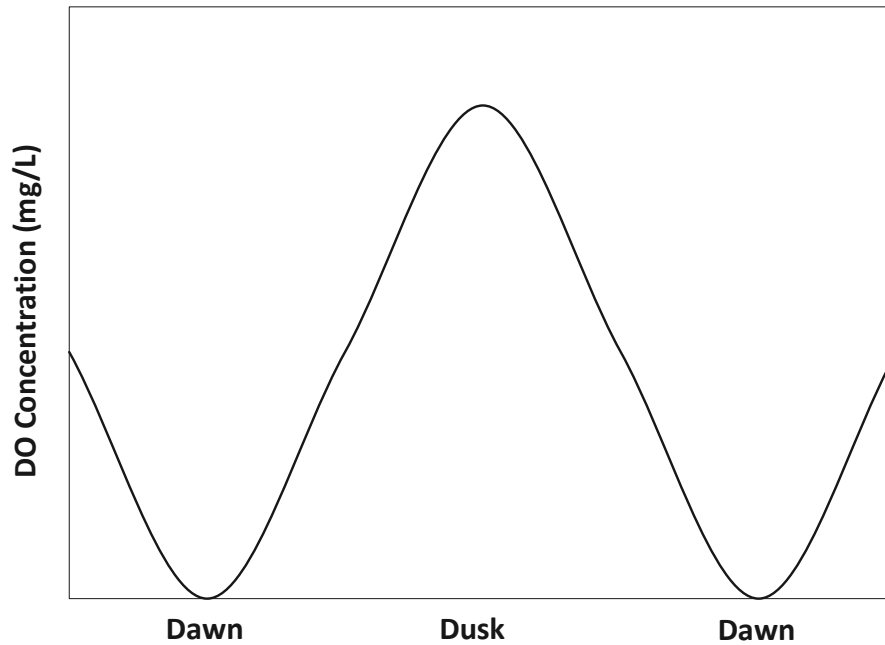
Figure 2.1: Diurnal oxygen cycle in an open-ocean aquaculture pen during a 24-hour period

The concentration of DO along with the seawater temperature and salinity controls the metabolism of Atlantic salmon in open-ocean aquaculture pens. Environmental factors, such as barometric pressure and water depth, can further affect DO balance in seawater, but the temperature is the most influential variable (Lawson, 2012). Warm water holds much less DO than cool water because the solubility of O_2 decreases with increasing temperature. Also, increasing temperature accelerates other factors such as the respiration rates and biological oxygen demand of other species that remove DO from seawater. Together, DO and temperature are two environmental variables that determine the environmental niche of Atlantic salmons (Lawson, 2012). Fish seek an environmental niche and maintain that niche through a complicated series of behavioural enviro-regulation and physiological acclimation processes. Fish can acclimate to low DO and to other physicochemical stimuli but these adjustments are slow, taking anywhere from a few hours to several weeks (Lawson, 2012). Therefore, it is important to maintain the DO level above 6 mg/L in open-ocean pens.

The DO in aquaculture pens can be depleted by (1) diffusion back into the atmosphere, (2) respiration by aquatic organisms and plants, and (3) decomposition of organic material by microbes residing largely in bottom sediments (Lawson, 2012). The DO consumption rates

by Atlantic salmon vary with water temperature, DO concentration, fish size, level of activity, and time after feeding. To combat low DO conditions surface and subsurface mechanical aeration systems can be used. The placement and timing of aeration and the use of air or O_2-enriched air can help optimize the delivery of DO and improve the economics of mechanical aeration.

This chapter discusses the dynamics of DO in open-ocean aquaculture including the diffusion mechanisms of O_2 into seawater, the solubility of O_2 in seawater, factors that affect DO concentration in open-ocean pens, and the effects that low DO has on the health of Atlantic salmon. Aeration technologies for open-ocean aquaculture will be introduced and strategies for placement and timing will be discussed.

2.2 Dissolved Oxygen Dynamics in Open-Ocean Aquaculture

2.2.1 Diffusion of Oxygen from the Gas Phase to the Liquid Phase

The rate of diffusion of O_2 to seawater depends on the difference in O_2 partial pressure between the gas phase and the concentration in the liquid phase. The greater the difference in partial pressures, the greater the driving force moving O_2 from one phase to the other. The maximum rate of O_2 transfer into seawater occurs when the DO concentration in seawater is 0 mg/L. As DO concentrations increase from 0 mg/L, the O_2 partial pressure difference between air and seawater steadily decreases up to the point where the DO concentration equals the saturation concentration. Lewis and Whitman (1923), developed the two-film model to explain mass transfer from gas to liquid and from liquid to gas. In the two-film model, O_2 first transfers from the bulk gaseous phase into the thin films surrounding the gas-liquid interface. Next, the O_2 must diffuse through laminar gas and laminar liquid films, respectively. Finally, the O_2 enters the bulk liquid phase (Seader, Henley & Roper, 2010). The total resistance to transfer from the gas to the liquid is made up of three resistances: the gas film, the interface, and the liquid film. An instantaneous equilibrium is assumed so there is no mass transfer limitation at the interface. It is also common for one of the films to exhibit high resistance to mass transfer compared to the other. Therefore, a single film control assumption can be applied. Oxygen is only slightly

soluble in water; therefore, the resistance to diffusion is controlled by the liquid film (k_l), and that provided by the gas film (k_g) is negligible in comparison (Seader et al., 2010). The two-film model is illustrated in Figure 2.2.
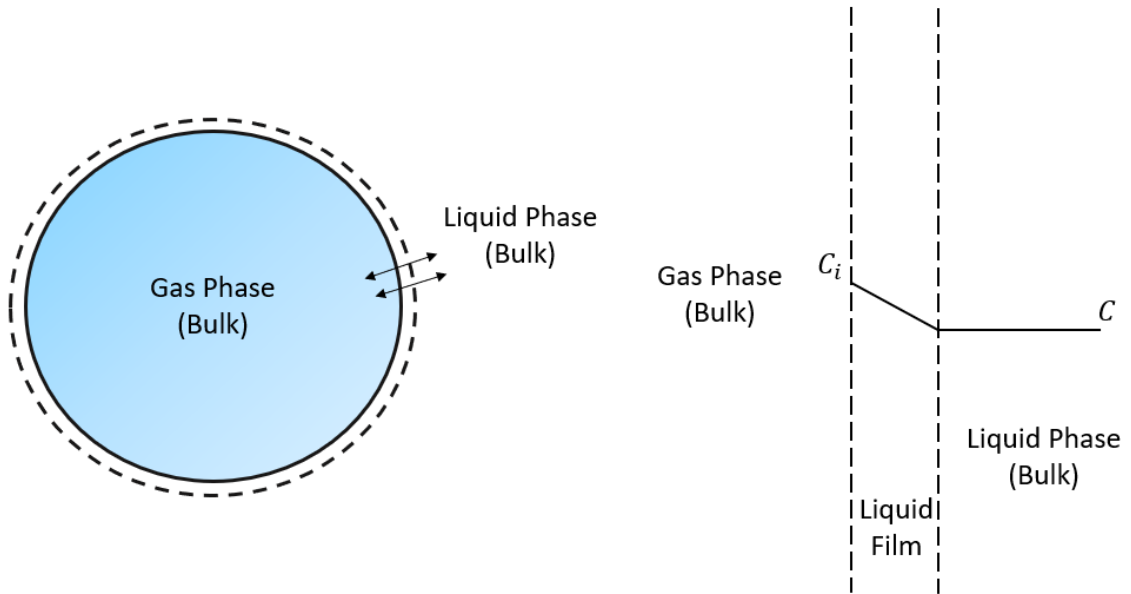
Figure 2.2: A two-film model for oxygen transfer from air into water showing a negligible film resistance to mass transfer on the gas side

The rate of O$_2$ movement between air and water can be described by the Lewis-Whitman gas transfer equation according to

$$\frac{dC}{dt} = k_l \frac{A}{V}(C^* - C) \qquad (2.2)$$

where dC/dt is the rate of O$_2$ transfer between the liquid and the gas (mol m^{-3} s^{-1}), k_l is the convective liquid-film coefficient (m/s), A/V, also referred to as a, is the ratio of the air-water interfacial area to water volume (m^{-1}), C^* is the DO concentration when water is saturated with O$_2$ under the prevailing conditions of water temperature, salinity, and atmospheric pressure (mg/L), and C is the measured DO concentration in the liquid (mg/L). Oxygen moves to and from water across the air-water interface; therefore, a greater amount of O$_2$ can enter or leave a given amount of water when the air-water interfacial area is increased. If the water is initially low in O$_2$, the thin film of water at the interface of a calm water surface quickly becomes saturated with O$_2$ which slows the rate of O$_2$ diffusion into the water. Turbulent mixing restores the saturation deficit in the surface film by moving

oxygenated water away from the surface, increasing the overall rate of O_2 transfer (Lawson, 2012).

2.2.2 Solubility of Oxygen in Seawater

Benson and Krause derived equations from thermodynamic principles that compute the solubility of O_2 in seawater for atmospheric air. Benson and Krause (1980) specify O_2 solubility as a function of temperature in freshwater, whereas Benson and Krause (1984) includes adjustments based on barometric pressure and salinity using

$$[DO] = DO_o F_S F_P \tag{2.3}$$

where the dissolved oxygen $[DO]$ concentration (mg/L) is represented as a baseline concentration in freshwater (DO_o) multiplied by a salinity correction factor (F_S) and a pressure correction factor (F_P). While all three terms are functions of water temperature, the salinity correction factor is a function of salinity, and the pressure correction factor is a function of barometric pressure. For freshwater (salinity = 0 g/kg) and standard pressure (101 325 Pa), the salinity and pressure factors are equal to one. To compute the O_2 solubility (mg/L), the baseline DO concentration at 0 salinity and at 101 325 Pa is

$$DO_o = e^{\left[-139.34411 + \frac{1.575701 \times 10^5}{T} - \frac{6.642308 \times 10^7}{T^2} + \frac{1.243800 \times 10^{10}}{T^3} - \frac{8.621949 \times 10^{11}}{T^4}\right]} \tag{2.4}$$

where T is temperature (K). The Benson and Krause salinity factor is

$$F_S = e^{\left[-S\left(0.017674 - \frac{10.754}{T} + \frac{2140.7}{T^2}\right)\right]} \tag{2.5}$$

where S is salinity (g/kg). The Benson and Krause pressure factor includes a correction for non-ideal gases and is calculated by

$$F_P = \frac{(P - P_w)(1 - \theta_o P)}{(1 - P_w)(1 - \theta_o)} \tag{2.6}$$

14

where P is the barometric pressure (Pa), P_w is the vapour pressure of water (Pa), and θ_o is the second virial coefficient of O_2 (Dymond & Smith, 1980) calculated using

$$\theta_o = 0.009672 - 4.94 \times 10^{-5}T + 6.436 \times 10^{-8}T^2 \tag{2.7}$$

The vapour pressure of water can be calculated using the Antoine equation (Yaws, 2009) according to

$$P_w = e^{\left[11.8571 - \frac{3840.70}{T} - \frac{216961}{T^2}\right]} \tag{2.8}$$

The Benson and Krause equations apply to a temperature range of 273.15 to 313.15 K, a salinity range of 0 to 40 g/kg and a pressure range of 50 662 to 111 458 Pa for atmospheric air. The maximum error in the Benson and Krause equation is on the order of 0.001 mg/L (Benson and Krause, 1984). The the effect of different salinities on the saturated DO concentration as a function of temperatures between 0 and 25°C is illustrated in Figure 2.3 at salinities of 0, 10, 20, and 30 g/kg for air at atmospheric pressure.
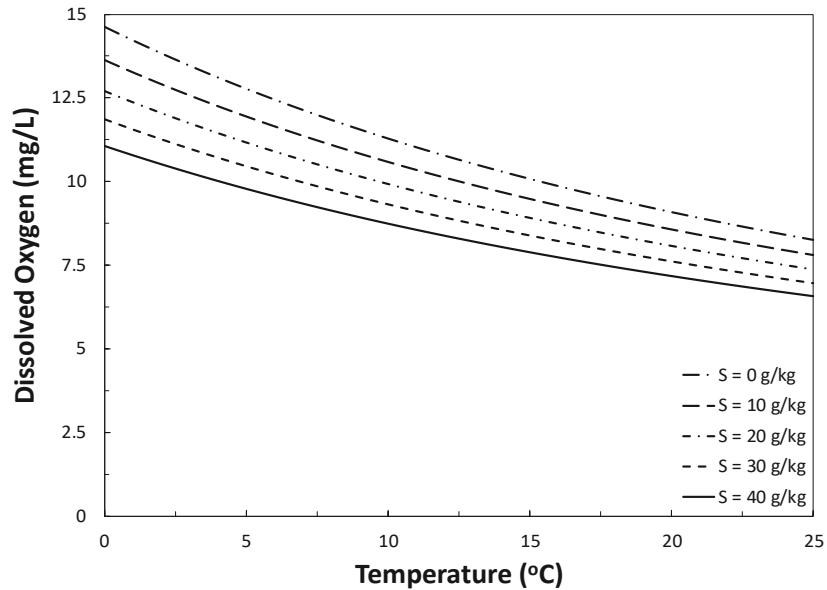
Figure 2.3: Saturated DO concentration as a function of temperatures between 0 and 25°C at salinities of 0, 10, 20, and 30 g/kg for air at atmospheric pressure

The saturated DO concentration decreases with increasing salinity. Dissolved O_2 supersaturation also occurs when the partial pressure of O_2 in solution exceeds the partial

pressure in the atmosphere (i.e., O_2 greater than 21 mol %). To illustrate the effect of water depth and gas phase composition, Henry's law is used, which states that the amount of dissolved gas is proportional to its partial pressure in the gas phase according to

$$C_{O_2} = K_{O_2} P y_{O_2} \tag{2.9}$$

where C_{O_2} is the liquid phase O_2 concentration (mg/L), K_{O_2} is the Henry's law constant of O_2 (mg L^{-1} Pa^{-1}) which is a function of temperature (K), P is pressure in the gas phase (Pa), and y_{O_2} is the gas phase O_2 composition. The Henry's law constant (Wüest et al., 1992) for O_2 as a function of temperature can be estimated using

$$K_{O_2} = 0.00068 - 1.6 \times 10^{-5} T + 1.85 \times 10^{-7} T^2 \tag{2.10}$$

The Henry's law constant as a function of temperature in Eq. 2.10 was developed by Wüest et al. (1992) using data from Marshall (1976) and is valid for a temperature range between 0 and 25°C. The Henry's law constant in Eq. 2.10 is limited for water; therefore, the salinity factor in Eq. 2.5 is required to adapt its use for seawater. Alternatively, a constant Henry's law constant of 1.2×10^{-5} mol m^{-3} Pa^{-1} for a temperature of 20°C can be used (Sander, 2015). Validation of the Henry's law constant in Eq. 2.10 can be found in Appendix A. The saturated DO profiles as a function of temperature at depths of 0, 10, 20, 30, and 40 m and salinity of 34 g/kg are illustrated in Figure 2.4.
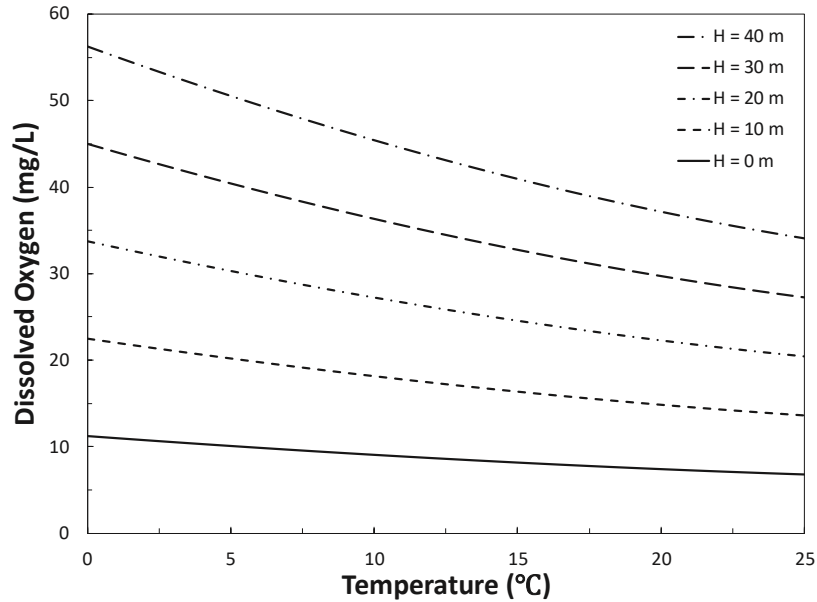
Figure 2.4: Saturated DO as a function of temperature at a salinity of 34 g/kg for air at the depths of 0, 10, 20, 30, and 40 m

The saturated DO concentration decreases with increasing temperature. Additionally, the saturated DO concentration increases with increasing hydrostatic pressure. The saturated DO profiles as a function of pressure at a temperature of 20°C and salinity of 34 g/kg for various gas phase O_2 compositions are illustrated in Figure 2.5.
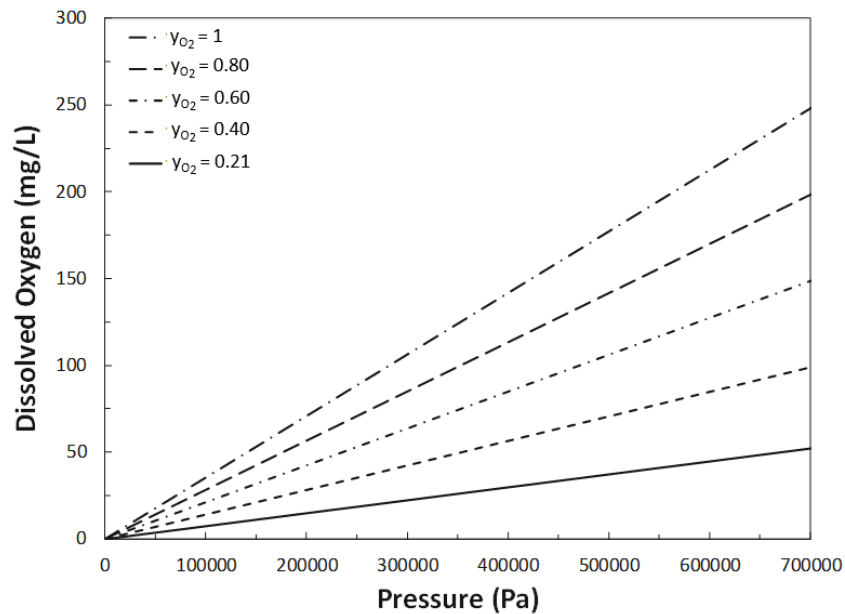
Figure 2.5: Saturated DO as a function of O_2 partial pressure at a temperature of 20°C and salinity of 34 g/kg at the indicated gas phase oxygen compositions

The DO saturation increases with increasing O_2 partial pressure in the gas phase. Additionally, the DO concentration increases with increased gas phase O_2 compositions. Appendix A contains the saturated dissolved nitrogen (DN) equations as a function of temperature, salinity, and pressure (Weiss, 1970).

2.2.3 Dissolved Oxygen Consumption Rates by Atlantic Salmon

Oxygen consumption in Atlantic salmon varies depending on numerous factors where the primary factors are body weight, temperature, growth rate, feeding rate, swimming velocity and stress levels. The expected normal O_2 consumption rate in post-smolt Atlantic salmon (body weight of 0.1 to 5 kg) ranges between 2 and 4 mgO$_2$ kgFish^{-1} min^{-1} at a water temperature of 15°C (Oppedal et al., 2011). The body weight of fish is known to affect O_2 consumption rates because smaller fish will consume more O_2 than larger fish. Oxygen consumption in Atlantic salmon increases exponentially with increasing water temperature. Oxygen consumption increases by a factor of 1.6 to 3.0 for every 10°C rise in water temperature. Salmon exposed to flowing water attempt to hold position against the flowing water. Fish swimming for prolonged periods can maintain O_2 consumption rates that are four to seven times greater than those at resting metabolic levels (Oppedal et al., 2011). Several models for estimating the O_2 consumption of post-smolt Atlantic salmon in seawater under routine aquaculture conditions have been developed (Bergheim et al., 1993; Grottum and Sigholt, 1998). The models calculate O_2 consumption based on fish size (body weight), temperature, and swimming speed (fish body lengths/s) using

$$DO_{fish} = aW^b(T - 273.15)^{c_1}10^{du_c} \tag{2.11}$$

where DO_{fish} is the O_2 consumption rate (mgO$_2$ kgFish^{-1} min^{-1}), W is the fish body weight (g), T is the water temperature (K), u_c is the mean current speed (cm/s), and a, b, c_1, and d are empirical constants fitted to the model. Bergheim (1993) developed a model for O_2 consumption in post-smolt Atlantic salmon according to

$$DO_{fish} = 1.92W^{-0.27}(T - 273.15)^{0.63}10^{0.010u_c} \tag{2.12}$$

18

Using the Bergheim (1993) model, the O_2 consumption rate (mgO$_2$ kgFish^{-1} min^{-1}) of post-smolt Atlantic salmon is illustrated in Figure 2.6 for temperatures of 10 and 20°C, body weights of 500 and 2500 g, and a water velocity between 0 and 50 cm/s.
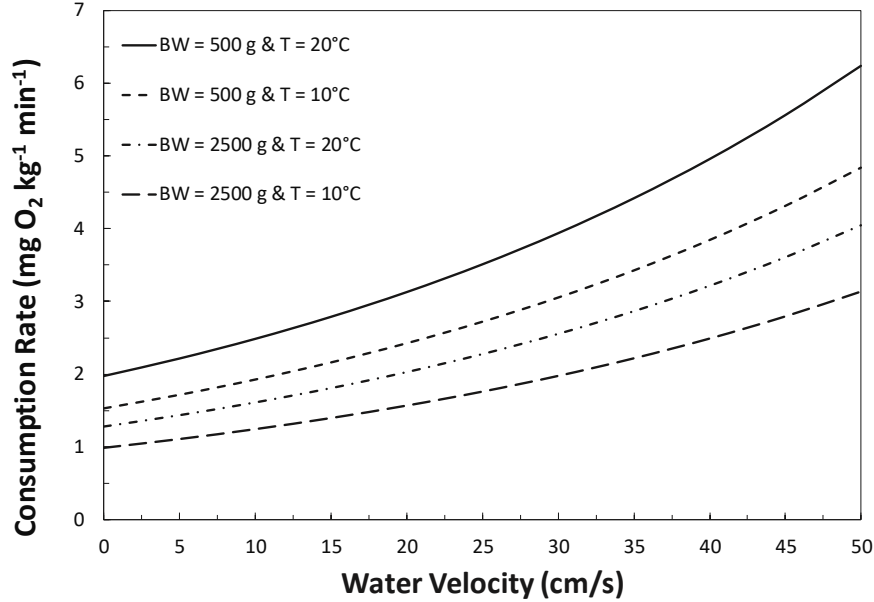
Figure 2.6: Oxygen consumption rate of post-smolt Atlantic salmon for temperatures of 10 and 20°C, body weights of 500 and 2500g, and a water velocity between 0 and 50 cm/s

The O_2 consumption rate of post-smolt Atlantic salmon decreases with increasing body weight and increases with increasing water temperatures and current velocity. In addition to the O_2 consumption rate of the Atlantic salmon, there is also O_2 consumption from other species in the open-ocean pen. The DO dynamics of the entire open-ocean pen (Lawson, 2012) can be modeled using

$$DO_t = \pm DO_{diffusion} + DO_{photosynthesis} - DO_{fish} - DO_{species} \qquad (2.13)$$

where DO_t is the total DO demand of the open-ocean pen (mg/L), $DO_{diffusion}$ is the DO added or removed from the pen by diffusion (mg/L), $DO_{photosynthesis}$ is the DO added to the pen by photosynthesis (mg/L), and $DO_{species}$ is the O_2 consumption rate of all other species in the open-ocean pen (mg/L). Equation 2.13 can be used to calculate the DO concentration when all the components of the equation are known. It is difficult to estimate the consumption rate of the entire niche because the species will have different densities in

each pen. However, the DO consumption rate of the other species in the open-ocean pen is expected to be insignificant compared to the stocking density of Atlantic salmon

2.2.4 Effects of Low Dissolved Oxygen on Atlantic Salmon Health

If DO concentrations are adequate, fish meet the increased demand for O_2 during active periods or just after feeding by increasing the volume of water passing over their gills. Atlantic salmon do this by using two physiological responses to acquire O_2: (1) By increasing the ventilation (breathing) rate, and (2) by taking in larger gulps with each breath, resulting in increased DO intake. When DO declines in the open-ocean pen, the behavioural and physiological responses of the fish begin to change (Lawson, 2012). First, Atlantic salmon will seek zones of higher DO concentrations in the open-ocean pen. When the salmon can no longer find zones of high DO the fish will become less active to conserve energy and metabolic O_2 and will even stop feeding in response to reduce their metabolism. As DO concentrations continue to decline, a compensatory point is reached where the O_2 demand of the fish tissue is greater than that which can be supplied by the behavioural and physiological responses of the fish (Lawson, 2012). At this point the Atlantic salmon will gape at the surface to remove DO from the thin surface film. Small salmon are more efficient at doing this than large salmon. Therefore, during O_2 depletions, larger salmon will die first, soon followed by the smaller salmon (Lawson, 2012). When the salmon gulp at the surface, the DO concentration is near the lethal level, and fish can only survive short periods under these conditions. DO saturation levels of 5.44 to 6.22 mg/L lead to reduced appetite, 4.66 to 5.44 mg/L lead to acute anaerobic metabolism and increased skin lesions, and 3.89 to 4.66 mg/L lead to acute stress responses, reduced feed conversion, and growth (Oppedal et al., 2011).

Dissolved gas supersaturation also has adverse effects on Atlantic salmon. Gas bubble disease occurs when the fish is exposed to excess gas such as CO_2, O_2, or N_2 in the water (Espmark, Hjelde & Baevefjord, 2010). The gas will begin to develop bubbles under the skin and in the vascular system, resulting in gas embolisms, and eventually death. The gas bubbles can also cause subdermal emphysema, including the lining of the mouth, which results in blistering of the skin around the mouth (Espmark, Hjelde & Baevefjord, 2010). The blistering contributes to the blockage of respiratory water flow over the gills, resulting

in suffocation and death. Atlantic salmon are especially sensitive to gas bubble disease and can tolerate partial pressures no greater than 17% of the atmospheric partial pressures at saturation (Espmark, Hjelde & Baevefjord, 2010).

2.3 Selection of Aeration Systems for Open-Ocean Aquaculture

In open-ocean aquaculture, the full demand for the O_2 supply of Atlantic salmon cannot be met through natural processes during times of warmer ocean temperatures and stagnant water circulation; therefore, mechanical aeration is required. Aeration is the process of adding O_2 to water to ensure salmon are receiving adequate DO. However, the cost of aeration is the third largest cost in intensive aquaculture, representing 15% of total production cost (Kumar, Moulick, & Chandra Mal, 2013). Several types of aerator configurations can be used to increase DO concentrations in open-ocean aquaculture. Therefore, the selection of aerators plays a major role in maximizing the profit. Proper aeration system selection is based on several factors including the size and depth of the pen, the shape of the pen (i.e., square, rectangular, or circle), seasonal changes such as temperature, and aerator type and efficiency.

2.3.1 Evaluating Performance of Aeration Systems

The O_2 transfer rate (OTR) is commonly used to evaluate the efficacy of aeration devices (Kumar et al., 2013). The OTR of an aerating device is defined as the mass of O_2 that the device can introduce into a body of water per unit time according to

$$OTR = k_l a (C^* - C_0) V \tag{2.14}$$

where OTR is the standard O_2 transfer rate (kgO_2/h), $k_l a$ is the overall volumetric O_2 transfer coefficient (s^{-1}), C_0 is the initial DO concentration (mg/L), and V is the aeration volume (m^3) of the aquaculture pen (Kumar et al., 2013). A more meaningful and comparative parameter for evaluating aeration systems is the SAE. The SAE is defined as the mass of O_2 transferred per unit power (kgO_2/kWh) according to

$$SAE = \frac{SOTR}{\dot{W}} \tag{2.15}$$

where $\dot{W}$ is the power input to the aeration system (kW). If DO_t (Eq. 2.13) in the aquaculture pen is known, the total power requirement (kW) for aeration can be estimated using

$$\dot{W} = \frac{DO_t}{\text{SAE}} \tag{2.16}$$

If the individual power requirement of an aerator ($\dot{W}_I$) is known, the total number of aerators (N) required for aeration can be estimated using

$$N = \frac{\dot{W}}{\dot{W}_I} \tag{2.17}$$

The cost of aeration can be evaluated by determining the fixed and variable costs associated with different modes of aeration (Kumar et al., 2013). The hourly energy cost (E_C) can be obtained from

$$E_c = E_r \dot{W}_i N \tag{2.18}$$

where E_c is the energy cost ($/h) and E_r is the electricity rate ($/kWh).

2.3.2 Types of Aeration Systems

Two types of aeration systems can be used: surface aeration and subsurface aeration. In surface aeration, the water surface is agitated to mix O_2 into the top layer of the water. Surface aeration devices include paddle-wheel aerators and propeller-aspirator pumps. Paddle-wheel aerators consist of a rotating hub with adjustable paddles that splash water into the air (Kumar et al., 2013). The paddle-wheels also cause horizontal movement of the water, increasing the mixing at the surface. Paddles that are set deeper in water will increase mixing but reduce aeration, and raising the paddles will have the opposite effect. Paddle-wheels have a standard aeration efficiency (SAE) of 1.1 to 3.0 kgO$_2$/kWh (Kumar et al., 2013).

Propeller-aspirator pumps consist of a rotating hollow shaft attached to an electric motor. A diffuser and an impeller are located at one end of the shaft and are submerged. The unit

is supported at the water surface with a float assembly so that a hole in the opposite end of the shaft near the motor remains above the water surface. The motor usually operates at 3 450 rpm, and the impeller accelerates the water sufficiently to cause a pressure drop within the hollow tube that forces atmospheric air into the tube (Kumar et al., 2013). The air passes through the diffuser and enters the water as fine bubbles that are mixed by the impeller. These aerators provide excellent water circulation in addition to aeration. Propeller-aspirator pumps have an SAE of 1.3 to 1.8 kgO_2/kWh (Kumar et al., 2013).

Surface aeration is effective for shallow aquaculture ponds; however, surface aeration methods do not aerate to a sufficient depth in open-ocean pens. When aquaculture pens are in deeper waters, such as those used for open-ocean aquaculture, subsurface aeration systems can be 5 to 10 times more effective than surface aerators at mixing and delivering O_2 (Kumar et al., 2013). Effective subsurface aeration systems include aeration cones (Speece cone), porous disc diffusers, and porous hose diffusers. An aeration cone, or a downward flow bubble contactor, consists of an inverted cone that is partially submerged in the receiving seawater. Seawater low in DO enters the top of the aeration cone with a stream of air or O_2 (McGinnis & Little, 1998). The seawater and air stream proceed toward the bottom of the cone with a reduced velocity. As the air or O_2 bubbles are carried downward toward the discharge, the water velocity is reduced until it equals the upward terminal velocity of the bubbles (McGinnis & Little, 1998). Therefore, the bubbles are held inside the cone for a period to enhance O_2 transfer. A portion of the air or O_2 is vented to strip away any N_2. The saturation of DO is determined by the operating pressure and depth of the aeration cone. (McGinnis & Little, 1998). The performance of aerator cones is determined by the seawater and air or O_2 flow rates, influent seawater DO concentration, off-gas vent rate, cone geometry and operating pressure. Aeration cones have an SAE of 2.0 to 2.5 kgO_2/kWh (Lawson, 2012).

Diffuser aeration systems use compressors to supply pressurized air or oxygen-enriched air to diffusers and porous pipes. In diffused systems, air is introduced either at the bottom of the pen or a specific location in the water, and O_2 is transferred as the bubbles ascend. The amount of O_2 transferred depends on the number, size and relative velocity of the ascending bubbles, the DO deficit, and the water depth at which the bubbles are released. Air bubble

size varies from extremely fine (0 to 3 mm) to coarse (3 to 10 mm), depending on the diffusion device used. Some common diffusers are fine bubble diffusers, coarse bubble diffusers, and porous hose diffusers.

Fine bubble diffusers produce 0 to 3 mm bubbles, have high aeration efficiency and have high oxygen transfer efficiency (OTR) due to the increased contact time because of slower bubble rise velocity (EPA, 1999). However, one disadvantage is that they are susceptible to fouling over time and require frequent maintenance. Fine bubble diffusers have a SAE of 1.8 to 3.9 kgO_2/kWh (EPA, 1999). In practice, more air can be released through coarse bubble diffusers, but the O_2 transfer is highest for the smallest bubble diameters. Also, the greater the water depth at the point of bubble release, the higher the O_2 transfer will be because the bubble-to-water contact time is larger (EPA, 1999). Most diffused-air systems release large volumes of air at low pressure. The minimum operating pressure increases with increasing water depth above the diffuser since enough pressure must be provided to force air from the diffuser against the total pressure (atmospheric plus hydrostatic) at the discharge point (Lawson, 2012). Porous diffuser hoses consist of a hose with fine perforations that release small bubbles evenly across the hose. Another type of aeration device is a packed bed that transfers O_2 to water and membrane contactors. Packed bed and membrane contactors are efficient on small scales but are not recommended for large-scale operations such as open-ocean aquaculture (Lawson, 2012). The different types of aeration devices are illustrated in Figure 2.7.
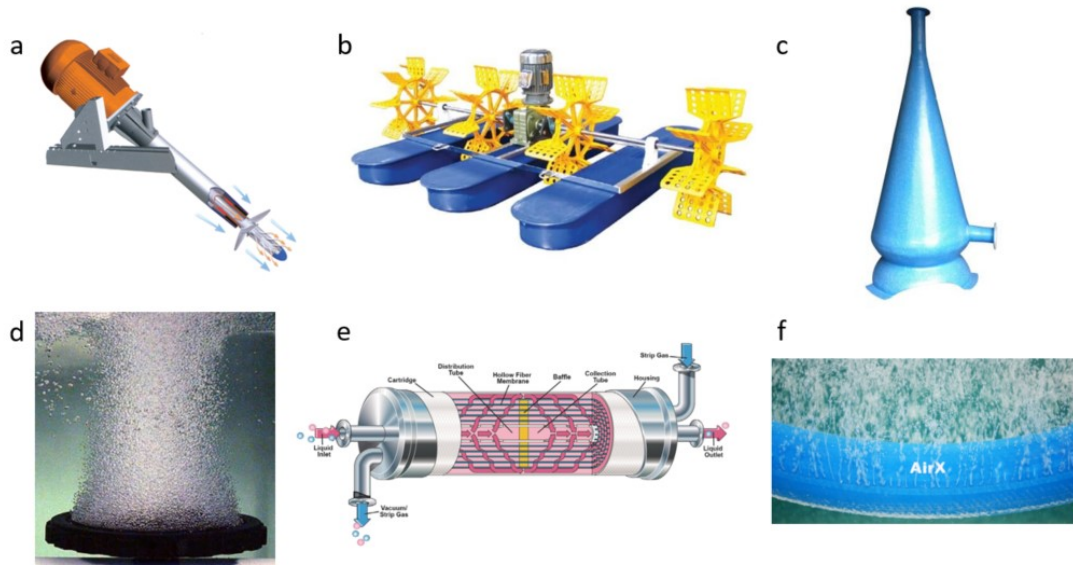
Figure 2.7: Types of aeration devices: (a) propeller-aspirator pump, (b) paddle-wheel aerator (Pentair, 2018), (c) aeration cone (Fresh by Design, 2018), (d) disc diffuser (Pentair, 2018), (e) membrane contactor (Applied Membrane, 2018), and (f) porous hose diffuser (OxyVision, 2018)

2.3.3 Production of Oxygen-Enriched Air for Aeration

The use of O_2 in aquaculture has increased in recent years in both the commercial and research sectors. Pure O_2 is available from three sources: (1) high-pressure O_2 gas in compressed cylinders, (2) liquid O_2 produced from cryogenic distillation, and (3) on-site generation using pressure swing adsorption (Smith & Klosek, 2001). High pressure O_2 cylinders and liquid O_2 (LOX) are produced offsite and delivered when required. Liquid O_2 is typically around 95 to 98% O_2 and produced by distilling liquefied air (cryogenic distillation). The LOX is stored in tanks designed to maintain a temperature of -182.9°C and pressure between 1000 to 4000 kPa (Smith & Klosek, 2001). When O_2 is needed, the LOX from the tank is vaporized by directing it through a heat exchanger.

In remote areas or when large volumes of O_2 are required, it may be more economical to generate O_2 on-site using pressure swing adsorption rather than pay transportation fees for the compressed or liquefied O_2. Pressure swing adsorption or membrane separation are used to produce O_2 on site to a purity of 85 to 95% (Smith & Klosek, 2001). A feed stream of dry atmospheric air is compressed to the O_2 generator requirement. The compressed air then flows through a vessel that is packed full of adsorbents that selectively adsorb N_2 from

the air to produce an O_2 enriched stream. When the bed reaches the N_2 adsorption capacity, the column is depressurized, removing N_2 so the bed can be reused. The O_2 is stored in a collection tank that is in a well ventilated and fire hazard free area (Smith & Klosek, 2001).

2.3.4 Placement of Aeration Systems in Open-Ocean Pens

The placement of the aeration system influences the effectiveness of O_2 transfer. Locating aerators to take advantage of ocean current (i.e., wind-driven currents) will help distribute oxygenated water and improve circulation and transfer efficiency (Lawson, 2012). When several aerators are used in aquaculture pens, it is recommended that the aerators be located where the current enhances the flow produced by the other aerators. Literature currently lacks aerator placement heuristics such as spacing between aerators and aeration configurations. Pentair, a manufacturer of open-ocean disc diffusers recommends using five evenly placed diffusers for a round pen 30 m in diameter with a depth of 15 m and using four diffusers near the corners of a rectangular pen 30 m in length and width, with a maximum operational depth of 15 m (Pentair, 2018). The Pentair disc diffuser configurations for circular and square aquaculture pens are illustrated in Figure 2.8.
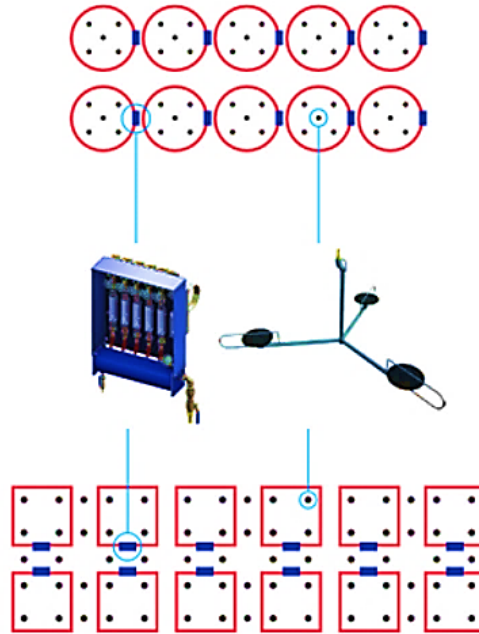
Figure 2.8: Pentair disc diffuser configurations for circular and square aquaculture pens (Pentair, 2018)

2.3.5 Timing of Aeration in Open-Ocean Pens

There are three strategies used to manage DO levels in open-ocean aquaculture (1) emergency aeration, (2) supplemental aeration, and (3) continuous aeration (Lawson, 2012). In emergency aeration, aerators are turned on only when the DO has dropped to levels that threaten the survival of the salmon. The usual strategy involves using the minimum number of aerators to create a zone of oxygenated water immediately around the aerator where the fish can gather. In the immediate area around the aerator, enough O_2 is added to the water to sustain life, but the overall DO concentration in the open-ocean pen is not increased significantly. Emergency aeration is detrimental to the salmon because, while it saves the salmon's life, the salmon are continually exposed to suboptimal O_2 concentrations. Repeated exposure to emergency aeration can result in added stress, poor feed conversion, reduced growth, increased susceptibility to disease, and mortality. Emergency aeration is the most cost-effective method of aeration. Supplemental aeration or nightly aeration is the practice of aerating at some fixed time every night well before DO concentrations fall to stressful levels and continuing to aerate until photosynthesis begins to add O_2 to the pen the next day. Depending on the stocking density and environmental niche of the open-ocean pen, aeration may only be required for three to four

27

hours. Continuous aeration is the practice of aerating 24 hours per day during the summer months when water temperature is highest. Supplemental and continuous aeration can be costly methods but have been shown to prevent DO concentrations from dropping to critical levels, which improves feed conversion ratios and increases salmon growth. Therefore, it is necessary to have a good understanding of the environmental trends near or at the aquaculture pens such as weather patterns, DO and temperature monitoring to improve prediction of high need aeration periods (Lawson, 2012).

2.4 Modeling of Open-Ocean Aeration Systems

There is no literature on the modeling of open-ocean aeration systems. However, previous modeling of bubble plumes released in the ocean can be applied to predict aeration in open-ocean aquaculture pens. There are three modeling techniques that can be used to predict the hydrodynamics and mass transfer rate from bubbles plumes produced by a diffuser: (1) empirical models or cone modeling, (2) integral modeling, and (3) computational fluid dynamic (CFD) modeling (Fraga & Stoesser, 2016). Cone modeling is the simplest approach to implement which assumes either that the bubble plume has a cone angles (θ) or that the radius at the surface is proportional to the release depth. The cone angle for flow rates that are used for aeration are between 10 and 12° (Fraga & Stoesser, 2016). Limitations with cone modeling include: (1) not directly solving hydrodynamics of the plume and (2) coupling of mass transfer from the bubble to the liquid without hydrodynamic information affects the scalability. When a higher degree of accuracy and information on plume hydrodynamics is required, then integral modeling is implemented.

In Integral models, the radial profiles of velocity and density are assumed to have a similar form at different heights within the plume. Integral models have an advantage over cone modeling because the coupling of mass transfer is easier with plume hydrodynamics (Fraga & Stoesser, 2016). The simplicity of integral models allows for quick predictions of real-scale bubble plumes. However, like cone modeling, integral models have disadvantages and limitations: (1) integral models are more difficult to implement and are more computationally intensive than cone modeling, (2) integral models are unable to predict the individual behaviour of bubbles such as bubble breakup or bubble coalescence because the

models cannot be connected to a three-dimensional flow field, (3) integral models also do not explicitly solve for fluxes occurring in radial or lateral planes; therefore, understanding plume-to-plume interactions and mixing from plume detrainment and entrainment can only be approximated, (4) integral models do not explicitly provide information regarding turbulence but rely on the entrainment assumption and momentum amplification factor as an approximation (Fraga & Stoesser, 2016). When information on individual bubble behaviour, turbulence, and plume-to-plume interactions is required, then CFD modeling is implemented.

Computational fluid dynamics is a multi-dimensional method that requires the solution for the equations of motion for a liquid carrier and a dispersed gas phase as well as coupling and interaction between the two phases (Olsen, Skjetne & Johansen, 2017). There are generally two accepted approaches for large scale CFD bubble plume modeling: Euler-Euler and Euler-Lagrange. In Euler-Euler, both the liquid phase and the gas phase are computed in an Eulerian framework. On the other hand, in Euler-Lagrange, flow of the carrier liquid is calculated the same as in Euler-Euler and the gas phase is treated as Lagrangian markers where the movement of each individual bubble or cloud of bubbles is tracked (Olsen, Skjetne & Johansen, 2017). Limitations with CFD include: (1) Euler-Euler and Euler-Lagrangian approaches require additional closure relationships and (2) CFD is computationally intensive and difficult to implement compared to cone modeling and integral modeling. A comparison of modeling approaches for bubble plumes generated by diffusers is summarized in Table 2.1.

Table 2.1: Comparison of Approaches to Plume Modeling

Modeling Approach	Scalability	Computational Cost	Difficulty of Implementation
Empirical or Cone	Low	Low	Low
Integral	Medium	Medium	Medium
CFD	High	High	High

There is no modeling information on open-ocean aeration systems; therefore, integral modeling is the preferred method because it is robust model that provide quick and accurate predictions of real-scale plumes.

2.5 Conclusions

Dissolved O_2 and temperature are two of the most important environmental variables that determine every Atlantic salmon's environmental niche. The level of DO in seawater is dependent on several biological and chemical processes; however, photosynthesis is the primary source of DO in open-ocean pens. The main resistance for DO transfer from the gas to the liquid phase is through the liquid-film mass transfer coefficient which can be described by the two-film theory model of Lewis and Whitman. A minimum DO concentration of 6 mg/L for cold-water species such as Atlantic salmon is recommended to protect the Atlantic salmon from adverse health effects such as acute stress responses, and reduced feed conversion and growth

Parameters that affect DO concentration in open-ocean pens include the saturated concentration level of DO and the DO consumption rate by Atlantic salmon. The saturation of DO in the liquid phase decreases with increased salinity and temperature and increases with increased pressure and gas phase O_2 concentration. The DO consumption rates of Atlantic salmon vary with water temperature, DO concentration, fish size, level of activity, and time after feeding and are between 2 and 4 mgO_2 $kgFish^{-1}$ min^{-1}.

Technical approaches for efficiently distributing DO to open-ocean aquaculture pens include surface and subsurface aeration systems. The placement and timing of aeration and the use of air versus O_2 can help optimize the delivery of DO and help reduce cost. Fine bubble diffusers are the recommended method for aerating in open-ocean aquaculture as these diffusers have a high SAE (1.8 to 3.9 kgO_2/kWh), can produce high flow rates, and are versatile in the use of air and O_2. The timing and placement of aeration and the use of air or oxygen-enriched air were evaluated based on need and on the cost of compression and the volume of gas necessary to reach the desired DO levels.

The next steps are to predict the timing, placement, and volume of gas required to maintain a minimum DO concentration of 6 mg/L. To meet this objective, a detailed model using the integral approach is required. The model should predict both the rate of mass transfer from the gas bubble to the liquid and hydrodynamics of the plume comprised of the gas released from the diffuser and the entrained liquid which rises to the free surface.

Chapter 3: Development and Validation of a Plume Model

3.1 Introduction

Bubble plumes are produced when gases are injected into liquids. A bubble plume consists of a rising bubble core and the surrounding water entrained in the flow. Due to water entrainment from the ambient environment, the bubble plume expands while it is rising. The bubble plume can be divided into three different zones: the zone of flow establishment or jet region, the zone of established flow or plume region characterized by self-similarity, and the surface zone characterized by an outward radial flow of entrained fluid (Figure 3.1). Bubble plumes occur in several engineering applications including underwater gas blowouts (Johansen, 2000; Yapa & Chen, 2004), reservoir destratification (Singleton & Little, 2006), CO_2 sequestration, and artificial aeration and oxygenation (Wüest, Brooks & Imboden, 1992; Lima Neto & Parente, 2016). Due to the complexity and the wide-reaching applications of bubble plumes, there is an interest in better understanding their hydrodynamic, mass transfer, and heat transfer properties. The integral approach is one method used to predict these phenomena.

Integral models are semi-empirical models that have been successfully used to provide accurate predictions of plume properties, including the centerline velocity and plume radius. Integral models are based on the assumption of self-similarity and the entrainment hypothesis (Morton, Taylor & Turner, 1956). The entrainment hypothesis introduced by Morton et al. (1956) states that the rate of entrainment at the edge of the plume is proportional to the characteristic velocity at that height. The proportionality constant is the entrainment coefficient (α), and the characteristic velocity is the plume centerline velocity (u). Integral models are based on the integration of the laws of conservation of mass and momentum combined with assumptions mainly regarding the entrainment and recirculation processes. In addition to the entrainment coefficient, integral models also rely on empirical parameters such as the spread ratio (λ), the momentum amplification factor (γ), and closure relationships for the mass and momentum conservation equations. The spread ratio can be expressed as the spreading ratio of the bubble core radius (λr_p) relative to the entrained liquid radius (r_p) and must take a value between 0 and 1. Literature has reported a variety of values for the spread ratio ranging from 0.2 (Ditmars & Cederwall,

1974), to 0.8 (Wüest et al., 1992; Milgram, 1983), to 1 (Crounse, Wannamaker & Adams, 2007). The momentum amplification factor can be expressed as the ratio of total momentum flux to the momentum flux carried by the mean flow. For bubble plumes with low gas flows rates and deep waters, Lima Neto (2012) showed that a relationship for the momentum amplification factor is required because the turbulent momentum becomes increasingly significant with decreasing flow rates (γ can be neglected for high flow rates). A diagram of a rising bubble plume separated into the zone of flow establishment, the zone of established flow, and the surface zone in an unstratified environment is illustrated in Figure 3.1.
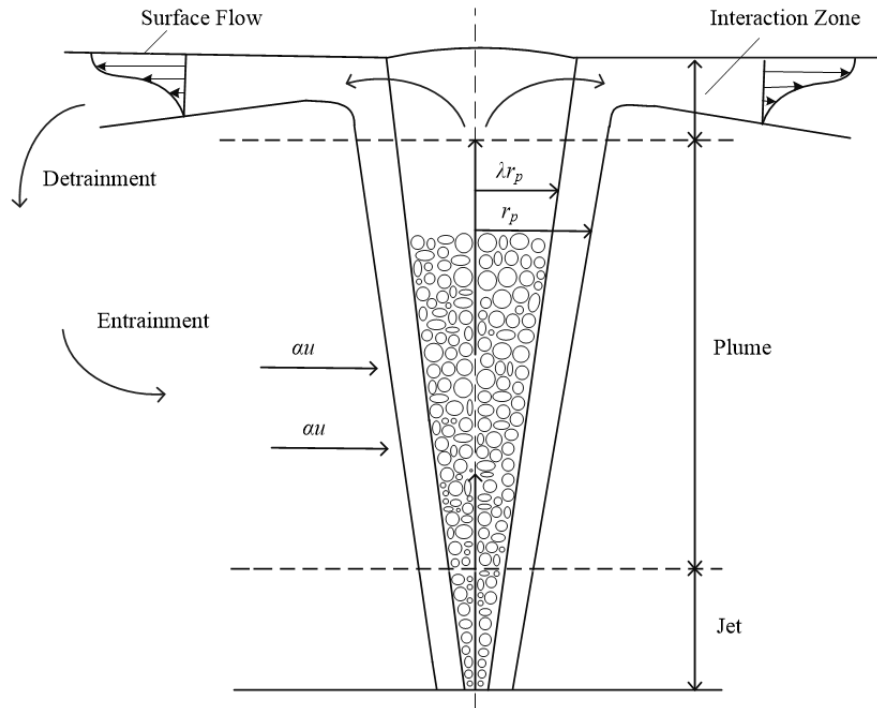
Figure 3.1: Bubble plume diagram separated into the zone of flow establishment, the zone of established flow, and the surface zone.

Integral models can differ in the assumption made for the self-similar profile. Models have been developed using either a Gaussian or Tophat self-similarity profile (Figure 3.1) to model the hydrodynamics of bubble plumes. A Tophat profile is a uniform distribution profile that has been shown to be sufficiently accurate given the approximations already contained in the integral approach. Gaussian profiles provide a more realistic approach representation of bubble plumes that are based on experimental data but which require more complex equations. Davidson (1986) showed that each of the profiles selected

(Tophat or Gaussian) led to different equations that govern the plume variables; however, the effects of these differences on actual plume predictions is insignificant with respect to predicting plume radius and plume centerline velocity.
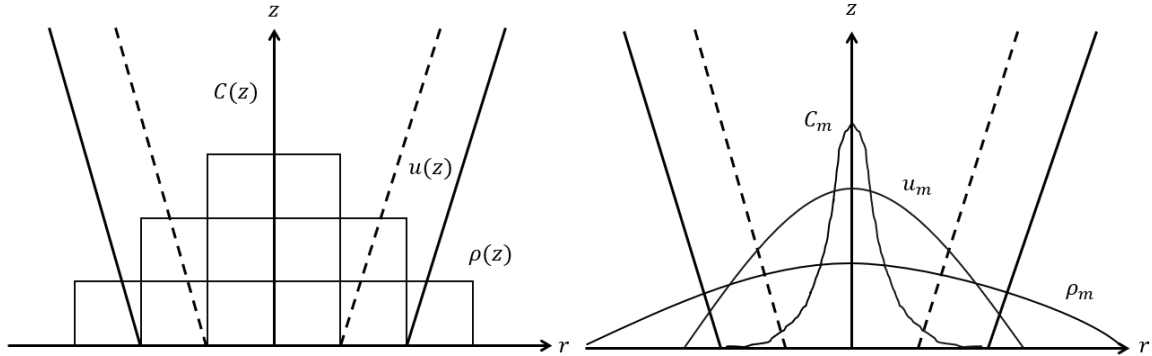
Figure 3.1: Tophat distribution (left) and Gaussian distribution (right)

Many integral models describing the behaviour of bubble plumes have been presented in the literature. Ditmars and Cederwall (1974) developed the first generation of integral models by adapting existing models for single-phase plumes from Morton et al. (1956) to multiphase plumes by incorporating the slip velocity. Milgram (1983) provided valuable experimental data to verify the integral models and investigated the model's main parameters: α, λ, and γ. Using experimental data from previous studies, Milgram developed empirical relationships for the entrainment coefficient and the momentum amplification factor. Wüest et al. (1992) developed a discrete bubble model for reservoirs in which the properties were evaluated in one bubble and extended to the rest at the same height. This model was used successfully in unstratified and stratified conditions by McGinnis and Little (2002) and McGinnis et al. (2004). More complex integral models have been developed by considering the effect of crossflow and the formation of a double plume (Socolofsky, Bhaumik & Seol, 2008); however, these approaches are outside the scope of the thesis. Common ranges and recommended values for the empirical parameters α, λ, and γ are provided in Table 3.1.

Table 3.1: Common Ranges and Recommended Values for the Empirical Parameters α, λ, and γ

Parameter	Range	Recommended Value
α	0.06 - 0.15	0.11
λ	0.6 – 1.0	0.8
γ	1 - 2	1

In this chapter, the integral approach is used to model gas transfer from bubble plumes. The model is based on Tophat profiles of plume properties, conservation equations for volume, momentum, species, and energy, and functional relationships modified from Lima Neto (2012, 2016) and Wüest et al. (1992) to describe the hydrodynamics and mass transfer of bubble plumes. The proposed integral model differs from previous approaches by incorporating a relationship for bubble terminal velocity with a swarm correction factor that accounts for various slip velocities as the bubble radius changes. The bubble plume is then coupled with an ambient environment model to account for the exchange of DO and solved using a novel approach in MATLAB® and Simulink® (The MathWorks Inc., 2018). Finally, the coupled model is validated using hydrodynamic studies from Fanneløp and Sjøen (1980) and Milgram (1983), and mass transfer studies from DeMoyer, Schierholz, Gulliver, and Wilhelms (2003), and Buscaglia, Bombardelli, and Garcia (2002).

3.2 Model Formulation

This section describes the derivation and justification of the conservation equations and closure relationships used for the bubble plume and the ambient environment.

3.2.1 Bubble Plume Model

Depending on the assumptions used to describe the liquid-gas mixture, a variety of mathematical models can be developed. The following relationships need to be considered when developing a complete bubble plume model using the integral approach: (1) a conservation of volume (or mass) equation that describes the rate of volume change in the bubble plume caused by the entrainment of water, (2) a conservation of momentum equation that describes the movement of gas bubbles and entrained water in the bubble

plume, (3) a conservation of energy equation that describes the rate of heat transfer from the gaseous phase to the plume and an energy conservation equation that describes the change in plume temperature, (4) a conservation equation describing the change in the bubble plume salinity, (5) a conservation of species equation for each species that describes the amount of dissolved species in the liquid phase within the bubble plume, (6) a conservation of species equation that describes the amount of gaseous species in the bubble plume, (7) closure relationships that calculate physical properties of the liquid and the gaseous phase.

Assumptions are required for the development of the mathematical model. The assumptions used in the model include: (1) the bubble source is assumed to produce bubbles at a constant rate and with a uniform distribution, (2) bubbles produced are spherical and of uniform size, and bubble coalescence and breakup are negligible, (3) the gas exchange between the water and gases other than O_2 and N_2 (CO_2 and Ar) is negligible, (4) there are no effects caused by interactions with other plumes, and (5) the gas exiting the diffuser transitions into the plume region instantaneously regardless of the gas velocity (jetting regime is neglected).

An Eulerian reference frame is used to derive the conservation equations in which the flow rates are considered entering and leaving a cylindrical control volume of a radius equal to the plume radius and height (Δz) fixed in time and space. The density of the fluid inside the control volume remains locally invariant (Boussinesq assumption). This assumption leads to cancellation of the density term from both sides of the mass conservation equation so that the mass terms for the continuous phase reduces to the corresponding volume terms. The reference frame is chosen such that the vertical coordinate (z) is positive upwards with the origin at the diffuser source. The conservation equations are derived using the assumptions listed for the plume model formulation. Figure 3.3 shows a sample control volume for the conservation equations.
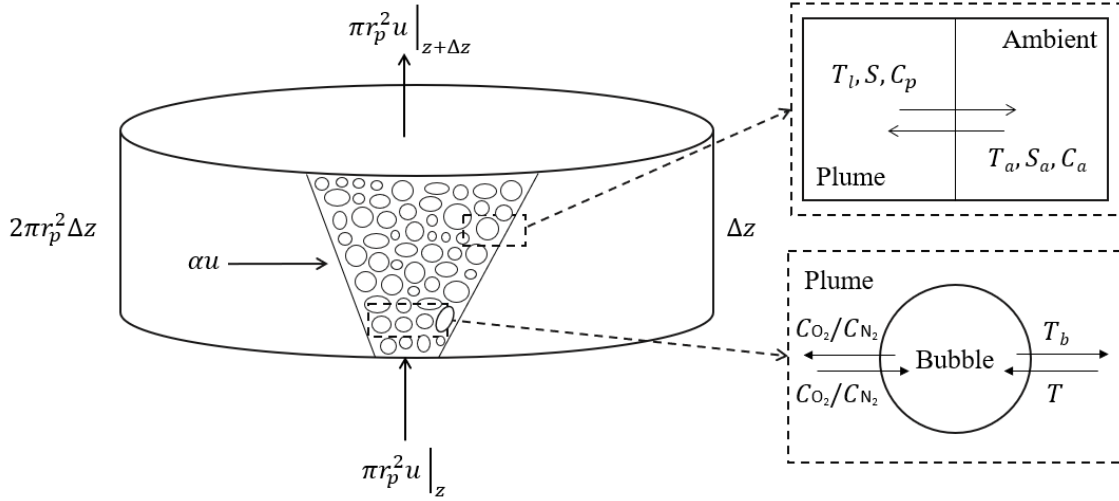
Figure 3.3: Control volume for the conservation equations

3.2.1.1 Conservation of Volume

The general expression for the water volumetric flow rate across a cross-section of a cylindrical control volume (Figure 3.3), is given by

$$Q = \int_0^{r_p} u(z,r)\big(1 - \varepsilon(z,r)\big)2\pi r dr + \int_0^{r_p} u_b(z,r)\varepsilon(z,r)2\pi r dr \qquad (3.1)$$

where u_b is the bubble velocity of the dispersed phase (j), u is the liquid centerline velocity of the continuous phase (i), and ε is the gas volume per total volume of the bubble-water mixture in the plume (gas holdup or phase fraction). For Tophat profiles, u_b can be defined as

$$u_b(z) = u + u_t \qquad (3.2)$$

where u_t is the slip velocity of the dispersed phase, relative to the continuous phase. A dilute plume assumption states that the gas phase fraction $\varepsilon(z,r)$ is small so that $\big(1 - \varepsilon(z,r)\big)$ is approximately equal to one and $\varepsilon(z,r)$ is approximately equal to zero. Therefore, the integration is simplifies to

$$Q(z) = \pi r_p^2 u \qquad (3.3)$$

37

The dilute plume assumption is only valid if the gas phase fraction is small ($\varepsilon < 10^{-2}$). If the phase fraction exceeds 1%, then the integration results in

$$Q(z) = \pi r_p^2 u(1 - \lambda^2 \varepsilon) \tag{3.4}$$

Finally, incorporating the entrainment hypothesis by Morton et al. (1956), the entrainment velocity (u_e) can be expressed as αu. The change in volumetric flow rate dQ inside the control volume for a steady flow is equal to the entrained volume flux, which is given by the product of the entrainment velocity and the circumferential area, $2\pi r_p dz$, of the control volume (3.3). The conservation of volume flux equation can be written as

$$\frac{d[\pi r_p^2 u(1 - \lambda^2 \varepsilon)]}{dz} = 2\pi r_p \alpha u \tag{3.5}$$

where z is the vertical coordinate (positive upwards), r_p is the radius of the plume (m), λ is the spreading ratio of the bubble core radius relative to the entrained liquid radius, and α is the entrainment coefficient.

3.2.1.2 Conservation of Momentum

The conservation of momentum equation can be derived from Newton's second law of motion, which states that a direct proportionality exists between the rate of change of momentum and the driving force. In a multiphase plume, this driving force can be attributed to buoyancy by

$$\frac{d\left(\frac{\dot{m}u}{\rho}\right)}{dz} = B_{dispersed} + B_{continuous} \tag{3.6}$$

where $B_{dispersed}$ is the buoyant force acting due to the dispersed phase (λr_p) and $B_{continuous}$ is the buoyant force acting due to the continuous phase ($r_p - \lambda r_p$), and dM/dz is the rate of change of specific momentum (m³/s²). The general expression for specific momentum flow across a cross-section of the cylindrical control volume is expressed as

38

$$M(z) = \gamma \left[\int_0^{r_p} u^2(z,r)(1 - \varepsilon(z,r))2\pi r dr + \int_0^{r_p} u_b^2(z,r)\varepsilon(z,r)2\pi r dr \right] \tag{3.7}$$

where $M(z)$ is the specific momentum (m^4/s^2). Using the dilute plume assumption, Eq. 3.7 can be integrated and reduced to give

$$M(z) = \pi \gamma r_p^2 u^2 \tag{3.8}$$

where γ is the momentum amplification factor that accounts for the added momentum due to turbulence (dimensionless). The general expressions for the buoyant forces on the dispersed and continuous phases across a cross-section of the cylindrical control volume can be substituted on the right side of Eq. 3.7 to give

$$\frac{d(\pi r_p^2 u^2)}{dz} = \frac{1}{\gamma} \left[\int_0^{(1-\lambda)r_P} \frac{\rho_a - \rho_w}{\rho_p} gu(z,r)(1 - \varepsilon(z,r))2\pi r dr \right.$$
$$\left. + \int_0^{\lambda r_p} \frac{\rho_a - \rho_p}{\rho_p} gu_b(z,r)\varepsilon(z,r)2\pi r dr \right] \tag{3.9}$$

where ρ_a is the density of the ambient fluid outside the plume (kg/m^3), ρ_w is the density of water inside the plume (kg/m^3), ρ_p is the mixture density of the bubbles and water (kg/m^3), and g is the acceleration due to gravity (m/s^2). The mixture density can be estimated using the expression $\rho_p = (1 - \varepsilon)\rho_w + \varepsilon \rho_g$. Integrating Eq. 3.9 reduces the equation to

$$\frac{d(\pi r_p^2 u^2)}{dz} = \frac{\pi r_p^2}{\gamma} \left[(1 - \lambda)^2 g \frac{\rho_a - \rho_w}{\rho_p} + \lambda^2 g \frac{\rho_a - \rho_p}{\rho_p} \right] \tag{3.10}$$

When there is no ambient fluid stratification, $\rho_a = \rho_w$ (Boussinesq approximation), the continuous buoyant force is negligible and Eq. 3.10 reduces to

$$\frac{d(\pi r_p^2 u^2)}{dz} = \frac{\pi r_p^2 \lambda^2 g}{\gamma} \frac{\rho_a - \rho_p}{\rho_p} \tag{3.11}$$

To consider gas expansion due to decompression as a bubble rises towards the surface the polytropic relation is used according to

$$\frac{\rho_{g,z}}{\rho_{g,0}} = \left[\frac{P_z}{P_0}\right]^{\frac{1}{n}} \tag{3.12}$$

where $\rho_{g,z}$ is the gas density at depth z (kg/m^3), $\rho_{g,0}$ is the gas density at the diffuser (kg/m^3), P_z is the pressure at depth z (Pa), P_0 is the pressure at the diffuser (Pa), and n is the polytropic index representing the isothermal ($n = 1$), isentropic ($n = Cp/Cv$), or incompressible flow ($n = \infty$). In the case of bubble plume modeling, a polytropic index representing isothermal flow ($n = 1$) is the most appropriate (Fanneløp & Bettelini, 2007). The pressure can be expressed in terms of hydraulic head (m), H_d, or pressure due to the liquid by

$$H_d = H_0 + \frac{P_{std}}{\rho_w g} \tag{3.13}$$

where H_0 is the hydraulic head at the diffuser (m) and P_{std} is the atmospheric pressure at the surface (Pa). Combining Eq. 3.12 and Eq. 3.13 gives

$$\frac{\rho_{g,z}}{\rho_{g,0}} = \left[\frac{H_d - z}{H_d}\right]^{\frac{1}{n}} \tag{3.14}$$

The gas density at depth z can be rearranged for the total mass of gaseous species according to

$$\rho_{g,z} = \frac{\dot{m}_{g,z}}{\dot{V}_z} \tag{3.15}$$

where $m_{g,z}$ is the total mass of gaseous species (kg), $\dot{V}_z$ is the gas volumetric flow rate at depth z (m^3/s). The resulting expression from the substitution of Eq. 3.14 into Eq. 3.15 and rearranging for $m_{g,z}$ is

$$\dot{m}_{g,z} = \rho_{g,0} \dot{V}_z \left[\frac{H_d - z}{H_d}\right]^{\frac{1}{n}} \tag{3.16}$$

The general expression for the mass conservation equation for the gas phase $\dot{m}_{g,z}$, can be expressed as

$$\dot{m}_{g,z} = \lambda^2 \pi r_p^2 \rho_{g,0} \left(\frac{\rho_a - \rho_p}{\rho_p} \right)(u + u_t) \tag{3.17}$$

The mass conservation for the gas phase in Eq. 3.17 can be rearranged to give

$$\frac{\rho_a - \rho_p}{\rho_p} = \frac{\dot{m}_{g,z}}{\lambda^2 \pi r_p^2 \rho_{g,0}(u + u_t)} \tag{3.18}$$

Substituting Eq. 3.16 into Eq. 3.18 gives

$$\frac{\rho_a - \rho_p}{\rho_p} = \frac{\dot{V}_z}{\lambda^2 \pi r_p^2 (u + u_t)} \left[\frac{H_d}{H_d - z} \right]^{\frac{1}{n}} \tag{3.19}$$

Finally, substituting Eq. 3.19 into Eq. 3.11 results in the final form of the momentum conservation equation. Additionally, $\dot{V}_z$ can be expressed as $V_{b,z} N_b$ resulting in

$$\frac{d(\pi r_p^2 u^2)}{dz} = \frac{g V_{b,z} N_b}{\gamma(u + u_t)} \left[\frac{H_d}{H_d - z} \right]^{\frac{1}{n}} \tag{3.20}$$

3.2.1.3 Conservation of Energy

The conservation of energy is used to derive the equation for the change of temperature of the bubbles in the plume. The change in temperature of the gas bubbles inside the control volume is due to heat transfer from the entrained liquid and heat released due to the dissolution of the dispersed phase (which is assumed negligible). The energy released from the bubble can appear as a loss or a gain; therefore, heat transfer from the bubble can occur in both directions. The general expression for the conservation of energy of a bubble can be expressed as

$$\frac{d(\varepsilon \pi r_p^2 \rho_g u_b e)}{dz} = -ha(T_b - T_l)\pi r_p^2 \tag{3.21}$$

41

where $e = C_{v,g}(T_b - T_{ref})$ is the specific internal energy for the bubble (J/kg), h is the convective heat transfer coefficient (W m^{-2} K^{-1}), $a = 3\varepsilon/r_b$ is the interfacial bubble area to volume (m^{-1}), T_b is the bubble temperature (K), and T_l is the plume temperature (K). Rearranging Eq. 3.21 for bubble temperature results in

$$\frac{dT_b}{dz} = -\frac{3h(T_b - T_l)}{r_b \rho_g C_{v,g}(u + u_t)} \tag{3.22}$$

where $C_{v,g}$ is the specific heat capacity of the gas (J kg^{-1} K^{-1}). The general expression for the conservation of energy in the liquid phase in the cylindrical control volume assuming a dilute plume assumption can be expressed as

$$\frac{d(\pi r_p^2 u T_l \rho_l C_{p,l})}{dz} = 2\pi r_p \alpha u T_a \rho_a C_{p,a} + \frac{3h(T_b - T_l)\pi r_p^2}{r_b \rho_g C_{v,g}(u + u_t)} \tag{3.23}$$

where T_a and T_l are the ambient and plume temperatures (K), and $C_{p,a}$ and $C_{p,l}$ are the ambient and plume specific heat capacities (J kg^{-1} K^{-1}). The ambient density and specific heat capacity can usually be considered constant and equal to the plume density and specific heat capacity, simplifying the energy balance. However, because the volume of gas at the source is expected to be large, the density and specific heat capacities can not be considered constant in this model. All the ambient, plume, and gas properties are a function of temperature. The energy balance in Eq. 3.23 is rearranged for temperature to give

$$\frac{dT_l}{dz} = \frac{2\pi r_p \alpha u T_a \rho_a C_{p,a} - T_l \rho_l C_{p,l}(2\pi r_p \alpha u)}{\rho_l C_{p,l} \pi r_p^2 u} + \frac{3h(T_b - T_l)}{r_b \rho_g C_{v,g}(u + u_t)} \tag{3.24}$$

The temperature balance in Eq. 3.24 can further be rearranged to give

$$\frac{dT_l}{dz} = \frac{2\alpha(T_a \rho_a C_{p,a} - T_l \rho_l C_{p,l})}{\rho_l C_{p,l} r_p} + \frac{3h(T_b - T_l)}{r_b \rho_g C_{v,g}(u + u_t)} \tag{3.25}$$

3.2.1.4 Conservation of Salinity

The conservation of salinity is derived on the basis that the change in salinity of the plume inside the control volume is due to the salinity of the entrained liquid. The general

expression for the conservation of salinity for the cylindrical control volume is expressed by

$$\frac{d\left(\pi r_p^2 u \rho_l S\right)}{dz} = 2\pi r_p \alpha u \rho_a S_a \tag{3.26}$$

where S_a and S are the ambient and plume salinities (g/kg). All the ambient, plume, and gas properties are a function of salinity; therefore, the salinity balance in Eq. 3.26 is rearranged to give

$$\frac{dS}{dz} = \frac{2\pi r_p \alpha u \rho_a S_a - \rho_l S\left(2\pi r_p \alpha u\right)}{\rho_l \pi r_p^2 u} \tag{3.27}$$

The salinity balance in Eq. 3.27 can further be rearranged to give

$$\frac{dS}{dz} = \frac{2\alpha(\rho_a S_a - \rho_l S)}{\rho_l r_p} \tag{3.28}$$

3.2.1.5 Conservation of Dissolved and Gaseous Species

A conservation equation is needed for each gaseous species being exchanged between the bubbles and the ambient fluid. Mass transfer from the gas fluxes can occur in both directions and appears as a gain in the dissolved species equation and a loss in the gaseous species equation. The general expression for the gaseous species molar flow rate through a cross-section of a cylindrical control volume (Figure 3.3), is given by

$$\dot{N}_g(z) = \left[\int_0^{r_p} u(z,r)\left(1 - \varepsilon(z,r)\right) C_i(z,r) 2\pi r dr \right. $$
$$\left. + \int_0^{r_p} u_b(z,r)\varepsilon(z,r) C_i(z,r) 2\pi r dr \right] \tag{3.29}$$

where $\dot{N}_g$ is the gaseous species molar flow rate (mol/s) and C_i is the gas phase concentration (mol/m³). The first term on the right-hand side of Eq. 3.29 is negligible as only the bubble is considered. Integrating Eq. 3.29 results in

43

$$\dot{N}_g(z) = \pi r_p^2 \lambda^2 u_b C_i \qquad (3.30)$$

The gas flux leaving the bubble to the liquid can be described by the Lewis-Whitman two-film expression according to

$$k_{l,i}(K_i P_i - C_i) \qquad (3.31)$$

where $k_{l,i}$ is the liquid-film mass transfer coefficient (m/s), K_i is the Henry's law constant (mol m^{-3} Pa^{-1}), P_i is the partial pressure of the species (Pa), and C_i is the dissolved gas concentration in the liquid (mol/m^3). To estimate the total gas transfer along the height of the plume, the total number of bubbles per unit time released from the diffuser into the plume (N_b) is assumed constant with no breakup or coalescence and determined using

$$N_b = \frac{\dot{V}_0}{V_{b,0}} \qquad (3.32)$$

where N_b is the total number of bubbles per unit time (s^{-1}), $\dot{V}_0$ is the gas volumetric flow rate at the diffuser (m^3/s), $V_{b,0}$ is the initial bubble volume at the diffuser (m^3). The number of bubbles at each height in the plume is

$$N_{b,z} = \frac{N_b}{u + u_t} \qquad (3.33)$$

where $N_{b,z}$ is the number of bubbles at each height in the plume (m^{-1}) and $u + u_t$ is the total bubble velocity (m/s). To account for the surface area of bubbles available to transfer mass, the total surface area of bubbles ($A_b = 4\pi r_b^2$) per unit plume height is found by multiplying the surface area of each bubble by the number of bubbles per unit height resulting in

$$\frac{4\pi r_b^2 N_{b,z}}{u + u_t} \qquad (3.34)$$

Combining Eq. 3.34 with Eq. 3.31, the conservation equation for the gaseous species molar flow is given by

$$\frac{d\left(\pi r_p^2 \lambda^2 (u + u_t) C_i\right)}{dz} = -\frac{4\pi r_b^2 N_{b,z}}{u + u_t} k_{l,i}(K_i P_i - C_i) \tag{3.35}$$

The general expression for the dissolved species molar flow rate across a cross-section of a cylindrical control volume (Figure 3.3), is given by

$$\dot{N}_l(z) = \left[\int_0^{r_p} u(z,r)\big(1 - \varepsilon(z,r)\big) C_i(z,r) 2\pi r dr \right. $$
$$\left. + \int_0^{r_p} u_b(z,r)\varepsilon(z,r) C_i(z,r) 2\pi r dr \right] \tag{3.36}$$

where $\dot{N}_l$ is the dissolved species molar flow rate (mol/s) and C_i is the dissolved gas concentration (mol/m^3). The second term on the right-hand side of Eq. 3.36 is negligible if the dilute plume assumption applies. Integrating Eq. 3.36 results in

$$\dot{N}_l(z) = \pi r_p^2 u C_i (1 - \lambda^2 \varepsilon) \tag{3.37}$$

The dissolved species molar flow rate changes with height as a result of the entrainment term at ambient concentration and the gas transfer term appears as a gain resulting in

$$\frac{d\left(\pi r_p^2 u C_i\right)}{dz} = 2\pi r_p \alpha u C_{a_i} + \frac{4\pi r_b^2 N_{b,z}}{u + u_t} k_{l,i}(K_i P_i - C_i) \tag{3.38}$$

A summary of the conservation equations and the variables used in the conservation equations is provided in Table 3..

Table 3.2: Conservation Equations for Plume Model and Definition of Variables

Conservation Equations	Variable	Term
	Entrainment (q_e)	$2\pi r_p \alpha u$
$\dfrac{dQ}{dz} = 2\pi r_p \alpha u$	Liquid volumetric flow (Q)	$\pi r_p^2 u$
$\dfrac{dM}{dz} = \dfrac{g V_{b,z} N_b}{\gamma(u + u_t)} \left[\dfrac{H_d}{H_d - z}\right]^{\frac{1}{n}}$	Momentum (M)	$\pi r_p^2 u^2$
$\dfrac{dT_l}{dz} = \dfrac{2\alpha(T_a \rho_a C_{p,a} - T_l \rho_l C_{p,l})}{\rho_l C_{p,l} r_p}$ $+ \dfrac{3h(T_b - T_l)}{r_b \rho_g C_{v,g}(u + u_t)}$	Temperature (T_l)	T
$\dfrac{dS}{dz} = \dfrac{2\alpha(\rho_a S_a - \rho_l S)}{\rho_l r_p}$	Salinity (S)	S
$\dfrac{d\dot{N}_l}{dz} = 2\pi r_p \alpha u C_{a_i} + \dfrac{4\pi r_b^2 N_b}{u + u_t} k_{l,i}(K_i P_i - C_i)$	Dissolved species molar flow ($\dot{N}_l$)	$Q C_i$
$\dfrac{d\dot{N}_g}{dz} = -\dfrac{4\pi r_b^2 N_b}{u + u_t} k_{l,i}(K_i P_i - C_i)$	Gaseous species molar flow ($\dot{N}_g$)	$\pi r_p^2 \lambda^2 u_b C_i$

3.2.2 Ambient Environment Mixing Model

To describe the mixing of O_2 from the bubble plume with the ambient environment a conservation equation can be derived by drawing a control volume (Figure 3.2). The following assumptions are required to derive the conservation equations: (1) the ambient environment is horizontally well mixed, (2) mixing in the vertical direction can be described by plug flow, (3) there is no back mixing in the vertical direction, and (4) the plume can only be entraining or detraining at any height along the plume.
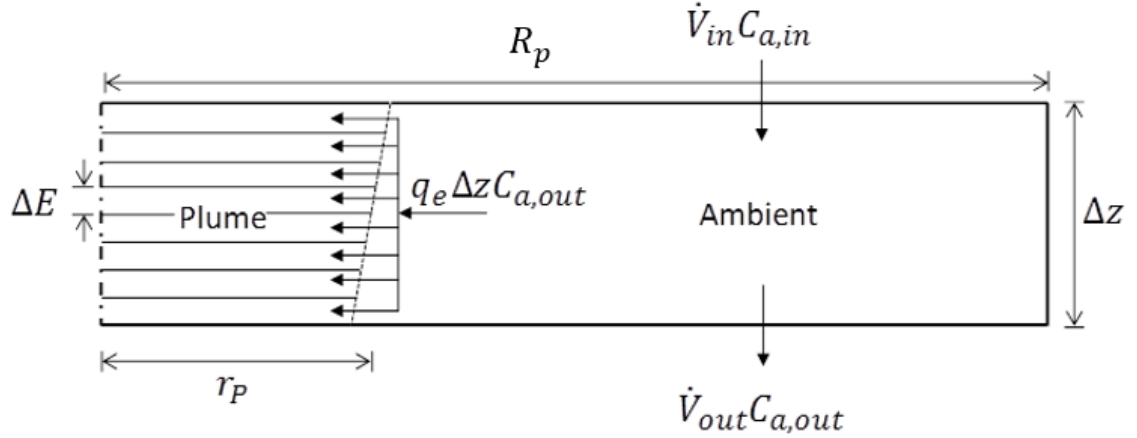
Figure 3.2: Control volume for the ambient environment

At the top of the plume, the entrained liquid and dissolved O_2 gets detrained and mixed into an ambient environment. As the detrained liquid is mixing in the ambient environment, the liquid is also entraining back into the plume. The rate of change of the vertical downward flow from the plume through a cross-sectional area can be described as

$$\frac{dV}{dt} = 0 = \dot{V}_{in} + q_d\Delta z - \dot{V}_{out} - q_e\Delta z \qquad (3.39)$$

where $\dot{V}_{in}$ is the volumetric flow rate entering the control volume (m^3/s), $\dot{V}_{out}$ is the volumetric flow rate leaving the control volume (m^3/s), q_d is the detrainment from the plume (m^2/s) and q_e is the entrainment into the plume (m^2/s). The entrainment is always equal to zero at the top of the plume and positive everywhere else along the plume. The conservation equation for the ambient O_2 concentration is given as

$$\left(\pi\left(R_p^2 - r_p^2\right)\Delta z\right)\frac{dC_a}{dt} = \dot{V}_{in}C_{a,in} - \dot{V}_{out}C_{a,out} + q_dC_p\Delta z - q_eC_a\Delta z \qquad (3.40)$$

where C_a is the O_2 concentration of the ambient environment in the control volume (mol/m^3), C_p is the O_2 concentration detraining from the plume (mol/m^3), R_p is the aeration radius of the entire control volume (m), and $C_{a,in}$ and $C_{a,out}$ are the O_2 concentrations entering and leaving the control volume respectively (mol/m^3).

3.2.3 Closure Relationships

The conservation equations require additional closure relationships for a solution to be possible. Previous models by Fanneløp & Sjøen (1980), Milgram (1983), Wüest et al., (1992), and Lima Neto et al. (2016) used a constant slip velocity between 0.23 and 0.30 m/s regardless of the gas phase fraction. However, the bubble terminal velocity changes significantly with bubble diameter and phase fraction. The terminal velocity of air bubbles in seawater is illustrated in Figure 3.3 for phase fractions of 0.01 to 0.40 at 20°C using Eq. 3.41 to 3.46.
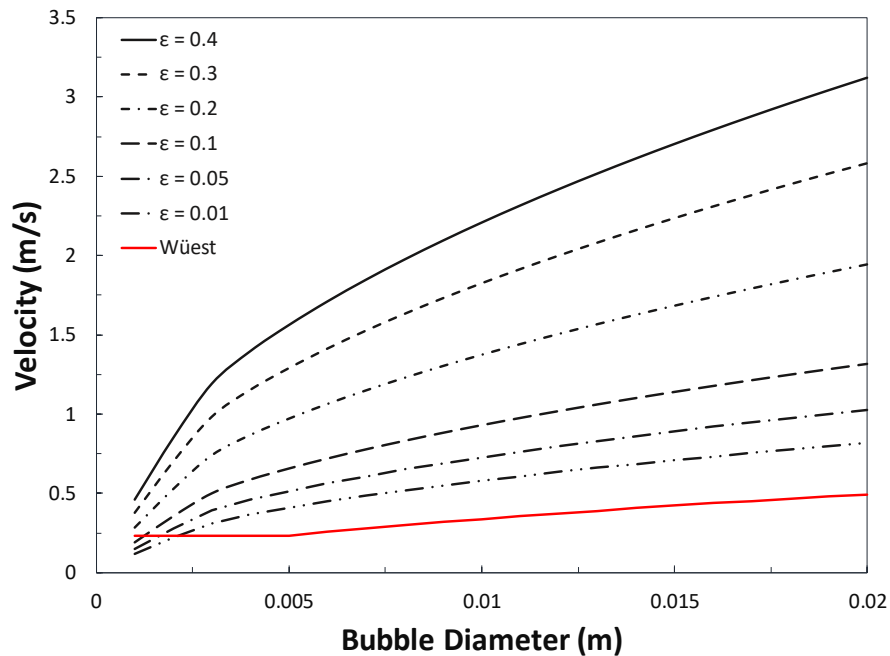
Figure 3.3: Terminal velocity of air bubbles (21 mol % O_2 and 79 mol % N_2) in seawater (34 g/kg) for gas phase fractions of 0.01 to 0.4 at 20°C using Eq. 3.41 to 3.46

To produce the results in Figure 3.3, a drag coefficient is required to quantify the resistance of a gas bubble moving through the liquid phase. The Schiller-Naumann model was originally derived for glass beads and is meant for solid spherical particles but has been successfully used in gas-liquid multiphase systems with a ± 5% deviation (Clift, Grace & Weber, 1978) from experimental data (Schiller & Naumann, 1933). The Schiller-Naumann drag coefficient can be expressed by

$$C_d = \begin{cases} \dfrac{24}{Re}(1 + 0.15Re^{0.687}), & Re \leq 800 \\ 0.44, & Re > 800 \end{cases} \tag{3.41}$$

where C_d is the drag coefficient (dimensionless) and $Re = \dfrac{|u_l - u_g|d_b\rho_l}{\mu_l}$ is the Reynolds number (dimensionless). The drag coefficient can then be used to estimate the terminal velocity (u_t) by

$$u_t = \left[\left(\frac{4d_b g}{3C_d}\right)\left(\frac{-\sum \rho_{g,i} y_i - \rho_l}{\rho_l}\right)\right]^{\frac{1}{2}} \tag{3.42}$$

where $\sum \rho_{g,i} y_i$ is the average of the gas phase densities (kg/m³). The gas bubble will decompress as it rises from the diffuser to the free surface, increasing the bubble volume. The ideal gas law combined with isothermal expansion is used to evaluate the impact of decompression on the bubble by

$$V_{b,z} = \frac{m_{b,z}}{\rho_{g,d}}\left(\frac{H_d}{H_d - z}\right)^{1/n} \tag{3.43}$$

where $V_{b,z}$ is the bubble volume (m³), $m_{b,z}$ is the total mass of gaseous species of a bubble (kg) at depth z, and $\rho_{g,d}$ is the density of the gas at the diffuser (kg/m³). The diameter of the bubble can be estimated assuming the bubble is spherical using

$$d_b = \sqrt[3]{\frac{6V_{b,z}}{\pi}} \tag{3.44}$$

where d_b is the bubble diameter (m). The effect of the gas phase fraction on the drag coefficient is included by using a correction of the bubble terminal velocity. Lockett & Kirkpatrick (1974) experimentally derived a bubble swarm correction for gas-phase fractions up to 50% using

$$u_t^* = u_t(1 - \varepsilon)^{1.39}(1 + 2.55\varepsilon)^3 \tag{3.45}$$

where ε is the gas phase fraction (dimensionless) and u_t^* is the swarm corrected terminal bubble velocity (m/s). The gas phase fraction can be estimated using the ideal gas law (Wüest et al., 1992) according to

$$\varepsilon = \left[\frac{\dot{n}_{O_2} + \dot{n}_{N_2}}{r_p^2 \lambda^2 (u + u_t)}\right]\frac{RT}{P} \tag{3.46}$$

where $\dot{n}_{O_2}$ and $\dot{n}_{N_2}$ are the molar flow rates (mol/s) of O$_2$ and N$_2$, respectively. To account for the transfer from the gas to the liquid, a mass transfer coefficient is required. The liquid-film mass transfer coefficient (k_l) is estimated by

$$k_l = \frac{\mathrm{Sh} D_{i,j}}{d_b} \tag{3.47}$$

where Sh is the Sherwood number (dimensionless), $D_{i,j}$ is the diffusion coefficient (m^2/s) of dissolved species (i) in the liquid phase (j), and d_b is the characteristic length or bubble diameter (m). The Sherwood number can be estimated using the Hughmark correlation (Hughmark, 1967) for air bubbles in water according to

$$\mathrm{Sh} = 2 + 0.463 \mathrm{Re}^{0.484} \mathrm{Sc}^{0.339} \left(\frac{d_b g^{\frac{1}{3}}}{D_{i,j}^{\frac{2}{3}}}\right)^{0.072} \tag{3.48}$$

where $\mathrm{Sc} = \frac{\mu_l}{\rho_l D_{i,j}}$ is the Schmidt number (dimensionless) and g is the gravitational constant (m/s^2). To account for the heat leaving the bubble, a convective heat transfer coefficient is estimated by

$$h = \frac{\mathrm{Nu} \kappa_l}{d_b} \tag{3.49}$$

where h is the convective heat transfer coefficient (W m^{-2} K^{-1}), Nu is the Nusselt number (dimensionless), and κ_l is the thermal conductivity of the liquid phase (W m^{-1} K^{-1}). The Nusselt number can be estimated using the Ranz-Marshall correlation (Ranz & Marshall, 1956) according to

$$\mathrm{Nu} = 2 + 0.6\mathrm{Re}^{0.5}\mathrm{Pr}^{0.33} \tag{3.50}$$

where $\mathrm{Pr} = \frac{C_{p,l}\mu_l}{k_l}$ is the Prandtl number (dimensionless). The properties used to estimate the Reynolds and Prandtl number for the heat transfer coefficient including the liquid phase specific heat capacity ($C_{p,l}$), viscosity (μ_l) density (ρ_l), and thermal conductivity (κ_l) are calculated using the film temperature equation according to

$$T_f = \frac{T_l + T_b}{2} \tag{3.51}$$

where T_f is the film temperature (K), T_l is the temperature of the liquid (K), and T_b is the bubble temperature (K). The property correlations can be found in Appendix A. Additional relationships for the entrainment coefficient and momentum amplification factor developed by Milgram (1983) can be found in Table 3..

Table 3.3: Empirical Correlations for Entrainment Coefficient and Momentum Amplification Factor Developed by Milgram (1983)

Entrainment coefficient:	$\alpha = 0.01481\ \ln\beta + 0.0824$ $\delta = \dfrac{g'\dot{V}_z}{H_0 u_t^3};\ g' = \dfrac{g(\rho_l - \rho_g)}{\rho_l}$
Momentum amplification factor:	$\gamma = 1.405\beta^{-0.18}$

3.3 Numerical Methodology

To simplify the system of nonlinear ordinary differential equations (ODEs), the dependent variables of each conservation equation (Table 3.) were transformed. The new conservation equations (Table 3.) can then be written in terms of new variables (Wüest et al., 1992; Singleton & Little, 2006).

Table 3.4: Transformation of Variables in the Plume Conservation Equations

Variable	Conservation Equation
Plume water volumetric flow (Q)	$\dfrac{dQ}{dz} = 2\alpha(\pi M)^{\frac{1}{2}}$
Momentum (M)	$\dfrac{dM}{dz} = \dfrac{gV_{b,z}N_b}{\gamma\left(\dfrac{M}{Q}+u_t\right)}\left[\dfrac{H_d}{H_d - z}\right]^{\frac{1}{n}}$
Salinity (S)	$\dfrac{dS}{dz} = \dfrac{2\alpha(\rho_a S_a - \rho_l S)}{\rho_l \dfrac{Q}{(\pi M)^{\frac{1}{2}}}}$
Dissolved species molar flow ($\dot{N}_l$)	$\dfrac{d\dot{N}_l}{dz} = 2\alpha(\pi M)^{\frac{1}{2}}C_{a,i} + \dfrac{4\pi r_b^2 N_b}{\dfrac{M}{Q}+u_t}k_{l,i}\left(K_i P_i - \dfrac{\dot{N}_l}{Q}\right)$
Gaseous species molar flow ($\dot{N}_g$)	$\dfrac{d\dot{N}_g}{dz} = -\dfrac{4\pi r_b^2 N_b}{\dfrac{M}{Q}+u_t}k_{l,i}\left(K_i P_i - \dfrac{\dot{N}_l}{Q}\right)$

The coupled plume model depends on initial conditions for the conservation equations. The initial conditions are controlled by liquid and gas properties at the diffuser depth and by the diffuser design. The initial bubble radius is determined by the diffuser nozzle or pore size, and the initial plume radius is determined by the effective diameter of the diffuser. The initial water velocity of the plume is an additional variable that needs to be determined when insufficient information is known about the diffuser. A densimetric Froude number was used to estimate the initial plume velocity (Wüest et al., 1992) by

$$\text{Fr} = \dfrac{u_0}{\left[\dfrac{2\lambda r_{p,0}\left(\rho_a - \rho_p\right)}{\rho_p}\right]^{\frac{1}{2}}} \tag{3.52}$$

where Fr is the Froude number (dimensionless) and u_0 is the entrance velocity at the source (m/s). The Froude number approaches a constant value of 1.7 as the plume travels farther from the diffuser. If the initial Froude number is less than 1.5, the initial plume water velocity increases immediately above the diffuser, and if the initial Froude number is

greater than 1.7, the initial plume velocity will decrease immediately above the diffuser. An increasing velocity above the diffuser is the expected behaviour because of entrainment (Wüest et al., 1992), so a value of 1.6 is used at the diffuser. A summary of the initial conditions required for the conservation equations is provided in Table 3..

Table 3.5: Initial Conditions for the Plume Conservation Equations

Variable	Term	Definition
Plume radius (m)	$r_{p,0}$	Effective radius of the diffuser
Centerline plume velocity (m/s)	u_0	Using Froude number of 1.6
Water temperature (K)	$T_{l,0}$	Ambient temperature at diffuser
Bubble temperature (K)	$T_{b,0}$	Temperature of compressed air
Salinity (g/kg)	S_0	Ambient salinity at diffuser
Pressure (Pa)	P_0	Depth and density at diffuser
Dissolved species conc. (mol/m^3)	$C_{i,0}$	Ambient concentration at diffuser
Bubble radius (m)	$r_{b,0}$	Diffuser design
Water volumetric flow (m^3/s)	Q_0	$\pi r_{p,0}^2 u_0$
Momentum (m^4/s^2)	M_0	$\pi r_{p,0}^2 u_0^2$
Dissolved species molar flow (mol/s)	$\dot{N}_{l,0}$	$Q_0 C_{i,0}$
Gaseous species molar flow (mol/s)	$\dot{N}_{g,0}$	$\dfrac{y_i P_{std} \dot{V}_{std}}{R T_{std}}$

Additional input variables are required to solve the conservation equations including the molar composition of gaseous species (y_i) and the flow rate from the diffuser ($\dot{V}_{std}$). The system of nonlinear ordinary differential equations (ODEs) in Table 3.4 are integrated numerically using the initial conditions in Table 3. and solved with an in-house code developed in MATLAB® and Simulink®. The system of nonlinear ODEs is solved using the *ode15s* algorithm built into MATLAB®. The *ode15s* algorithm is a variable step, variable-order, implicit solver that is based on the backward numerical differentiation formulas of orders one to five (Shampine, Reichelt & Kierzenka, 1999). The MATLAB® and Simulink® algorithm used to solve the system of ODEs is illustrated in Figure 3.4.

53
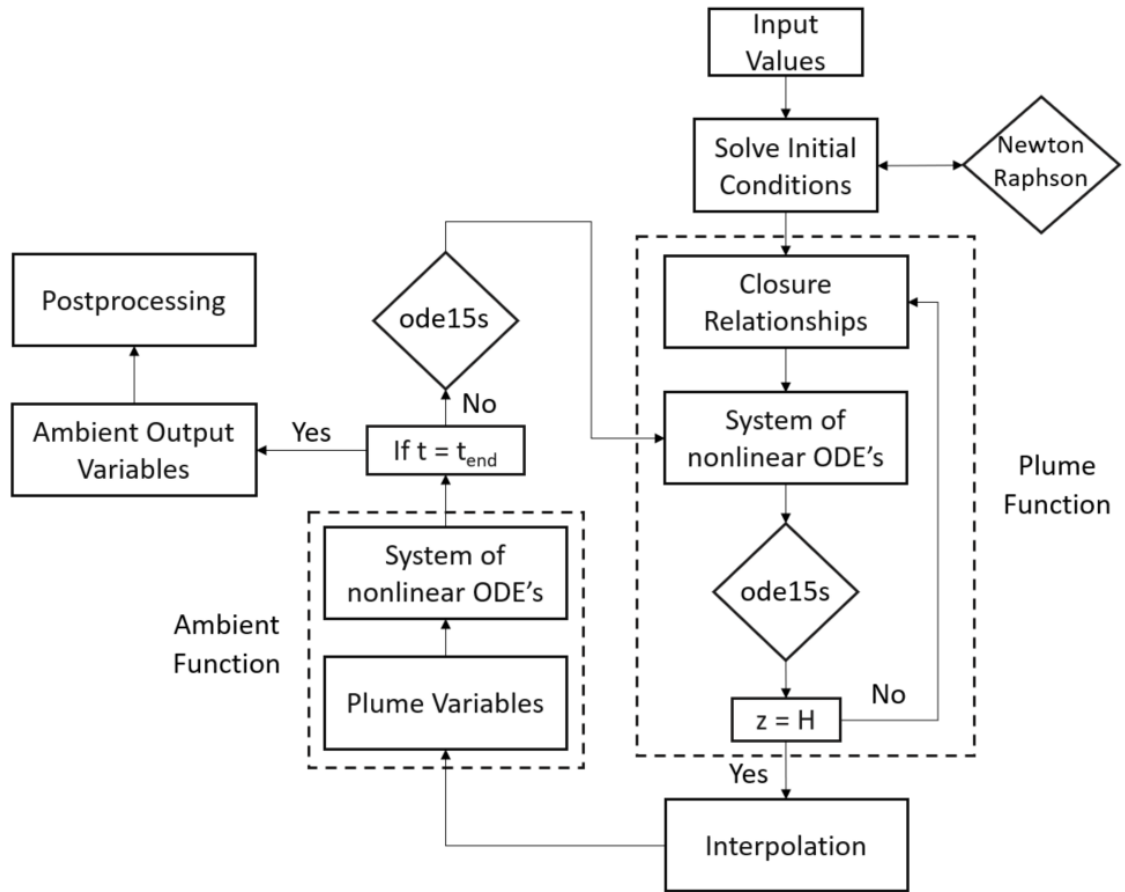
Figure 3.4: MATLAB® and Simulink® algorithm used to solve the system of ODEs

The algorithm consists of the *Plume Function* which solves for the bubble plume and the *Ambient Function* which solves for mixing and detrainment from the plume. The *Plume Function* and *Ambient Function* are divided into horizontal slices, n_E and n_Z respectively. The *Plume Function* consists of 10 times the number of segments as the *Ambient Function* (i.e. if the *Plume Function* has 100 segments, the *Ambient Function* has 10 segments). The limits of integration also need to be specified for both functions. The *Plume Function* requires the limits $[0 \; H_0]$ and the *Ambient Function* requires the limits $[t_{start} \; t_{end}]$. The algorithm begins with the *Plume Function*, where initial values are specified, initial conditions are solved using a Newton-Raphson solver, closure relationships are solved, and systems of nonlinear ODEs are solved. When the *ode15s* solver completes the specified number of iterations, n_E, the plume variables are passed to the *Ambient Function*. The *Ambient Function* solves the mixing of gaseous species detrained from the plume with the ambient water. The mixing is modeled using a tanks-in-series approach in the vertical

direction, and as perfectly mixed in the horizontal direction. The *Ambient Function* then steps forward in time and passes the output variables back to the *Plume Function* once it has completed the number of specified iterations, n_z. The algorithm continues to loop until the specified time, t_{end}, is reached. The gas properties in the mathematical model for O_2 and N_2, including density, viscosity, and specific heat capacity are temperature dependent. Correlations were used to estimate the viscosity (Yaws, 2014) and specific heat capacity (Yaws, 2015), and the ideal gas law was used to estimate the density of O_2 and N_2. The seawater properties in the model including density, viscosity, specific heat capacity, and thermal conductivity are temperature, salinity, and pressure dependent. Correlations were used to estimate the density, viscosity, specific heat capacity, and thermal conductivity. Descriptions of the correlations used for seawater, O_2, and N_2 are provided in Appendix A.

3.4 Validation Case Studies and Discussion

Four case studies were used to validate the hydrodynamics and mass transfer predictions for the integral model approach. The Fanneløp & Sjøen (1980) and Milgram (1983) experiments were used to validate the plume centerline velocity and plume radius, and the DeMoyer et al. (2003) and Buscaglia et al. (2002) experiments were used to validate the mass transfer from gaseous species to the liquid ambient environment.

3.4.1 Hydrodynamic Validation Case Studies

3.4.1.1 Fanneløp & Sjøen (1980) Case Study

To validate the plume hydrodynamics including the plume radius and plume centerline velocity of the model, the experimental data of Fanneløp and Sjøen (1980) were compared to the present model. The Fanneløp and Sjøen (1980) case study was selected because the low velocities released from the diffuser and the depth of the experiment is similar to the velocities and operational depths of diffusers used for aquaculture. Fanneløp & Sjøen (1980) were studying the hydrodynamic structure of deep-set underwater bubble plumes and were interested in the gas expansion with decreasing hydrostatic pressure and the influence of variable buoyancy on relevant plume parameters. The Fanneløp & Sjøen (1980) experiment was conducted in a towing basin with a height of 10 m, a width of 10.5

m, and a length of 150 m. Air (21 mol % and 79 mol %) was injected into the bottom of the towing basin using a diffuser with a diameter of 100 mm. The diffuser had 150 1-mm holes, generating bubble sizes up to 10 mm. An annotated diagram of the Fanneløp & Sjøen (1980) experiments is illustrated in Figure 3.5.
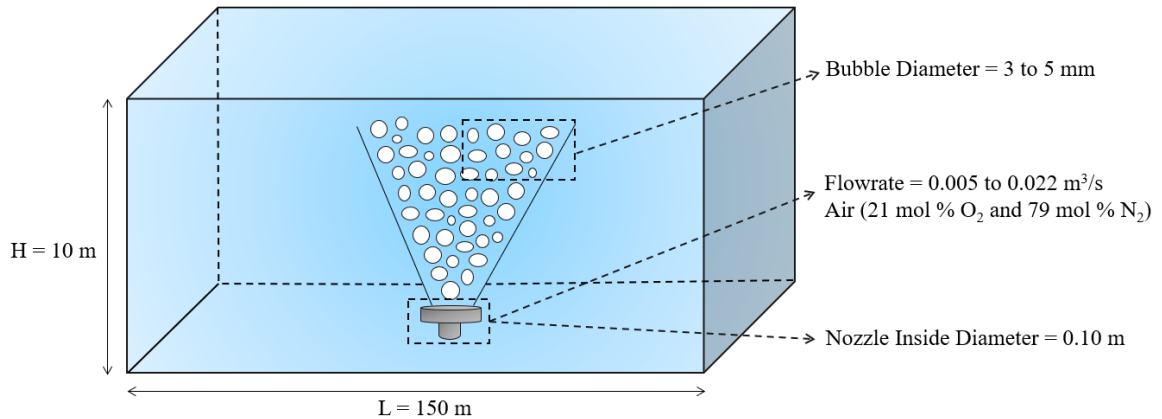
Figure 3.5: Annotated diagram of the Fanneløp & Sjøen (1980) experiments

To solve the Fanneløp & Sjøen case study for flow rates of 0.0100 and 0.0221 m^3/s at standard conditions, the initial conditions in Table 3. were used.

Table 3.6: Initial Conditions Used for the Fanneløp & Sjøen (1980) Case Study for Flow Rates of 0.01 and 0.0221 m³/s

Initial Condition	Variable	Case Study	
		0.0100 m³/s	0.0221 m³/s
Plume radius (m)	$r_{p,0}$	0.0500	0.0500
Centerline plume velocity (m/s)	u_0	1.64	2.76
Water temperature (K)	T_0	293	293
Bubble temperature (K)	$T_{b,0}$	293	293
Salinity (g/kg)	S_0	0	0
Dissolved O_2 concentration (mol/m³)	$C_{O_2,0}$	0	0
Bubble diameter (m)	$d_{b,0}$	0.003 to 0.005	0.003 to 0.005
Water volumetric flow (m³/s)	Q_0	0.0129	0.0217
Momentum (m⁴/s²)	M_0	0.0212	0.0598
Dissolved O_2 molar flow (mol/s)	$\dot{N}_{l,0}$	0	0
Gaseous O_2 molar flow (mol/s)	$\dot{N}_{g,0}$	0.0937	0.207

Three conditions were studied to validate the Fanneløp & Sjøen (1980) case study: (1) no dissolution with a constant slip velocity of 0.23 m/s and bubble diameters of 3 to 5 mm, (2) dissolution of air bubbles at a constant slip velocity of 0.23 m/s and bubble diameters of 3 to 5 mm, and (3) dissolution of air bubbles with a slip velocity that changes with gas phase fraction, and bubble diameters of 3 to 5 mm. The constant bubble velocity case studies and the slip velocity that changes with gas phase fraction case study were performed using $\lambda = 0.8$, $\alpha = 0.11$, and $\gamma = 1.35$. The plume radius and plume centerline velocity of Fanneløp & Sjøen (1980) for flow rates of 0.01 and 0.0221 m³/s are illustrated in Figure 3.6.
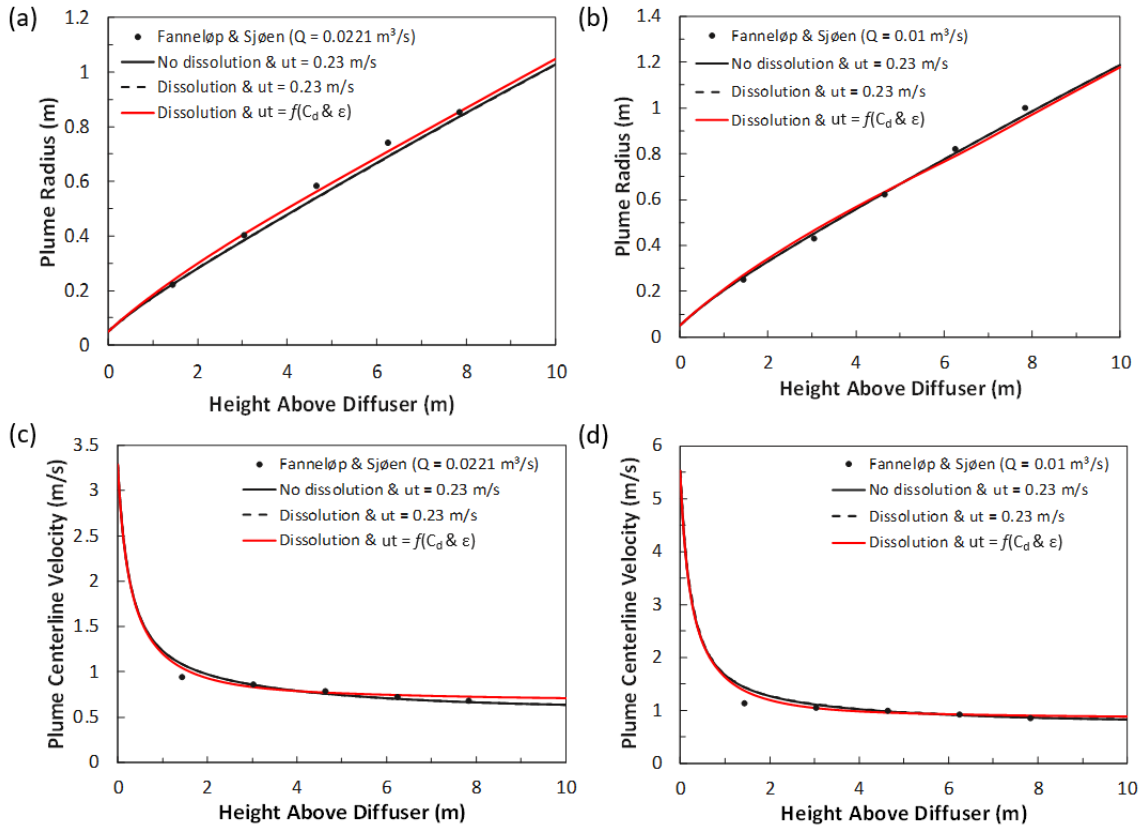
Figure 3.6: Comparison between the present model and the experimental data of Fanneløp & Sjøen (1980) for (a) plume radius for a flow rate of 0.01 m³/s (b) plume radius for a flow rate of 0.0221 m³/s (c) plume centerline velocity for a flow rate of 0.01 m³/s, and (d) plume centerline velocity for a flow rate of 0.0221 m³/s

There was no significant difference for the plume radius and plume centerline velocity for bubble size between 3 and 5 mm; therefore, only the results for the 3 mm bubble are shown. There is a small difference between the dissolution and no dissolution case studies; however, the difference is overall insignificant. The addition of a slip velocity as a function of the drag coefficient and swarm correction provided a comparable fit to the Fanneløp & Sjøen (1980) experimental data.

3.4.1.2 Milgram (1983) Case Study

To further validate the plume hydrodynamics including the plume radius and plume centerline velocity of the model, the experimental data of Milgram (1983) were compared to the present model. The Milgram (1983) case study was selected to determine the limitations of the present model because the Milgram (1983) experiments were conducted at higher velocities and released from a pipe. Milgram (1983) was interested in looking at

58

previous bubble plume studies to compile a dataset ranging from depths of 3.66 to 50 m and gas flow rates between 0.0002 and 0.590 m^3/s at standard conditions. A large dataset with a broad range allowed Milgram to developed functional relationships for parameters such as the entrainment coefficient and the momentum amplification factor. The Milgram (1983) experiments were conducted in Bugg Spring, which is a natural sinkhole located in Okahumpkar, Florida. The depth of Bugg Spring was 50 m; however, the width and length of the spring varied with height. Milgram injected air (21 mol % O_2 and 79 mol % N_2) through a 5 cm circular pipe at flow rates of 0.0240 to 0.289 m^3/s at standard conditions. An annotated diagram of the Bugg Spring Milgram experiments is illustrated in Figure 3.7.
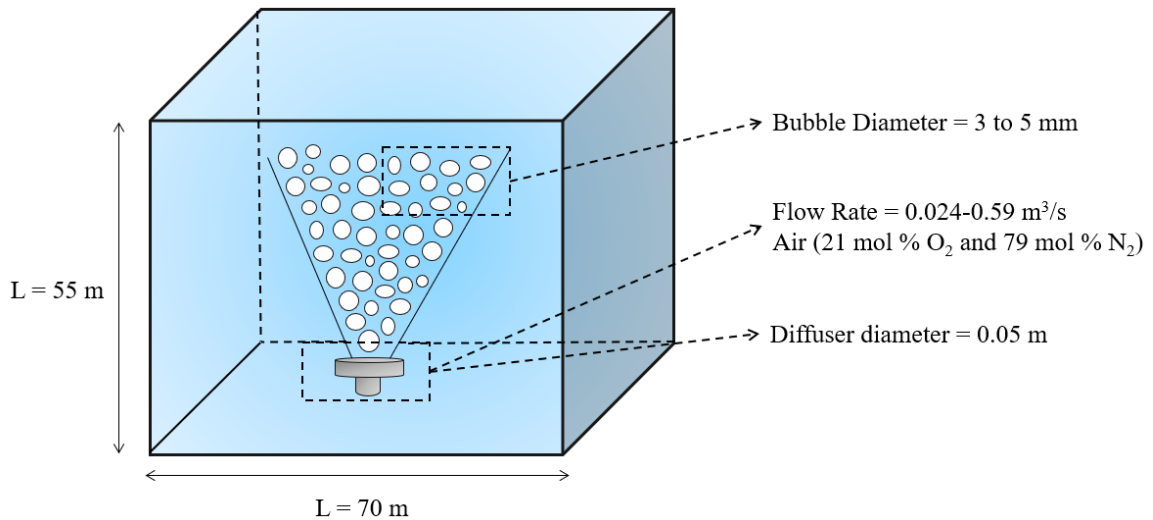
Figure 3.7: Annotated diagram of the Milgram (1983) experiments

The gas exiting the circular pipe will initially form a jet at high velocity. The jetting regime is ignored for the Milgram cases, and the bubble diameters are assumed to be between 3 and 5 mm at the pipe exit. To solve the Milgram case studies for air flow rates of 0.0240 to 0.289 m^3/s, the initial conditions in Table 3. were used.

Table 3.7: Initial Conditions Used for the Milgram (1983) Case Study for Flow Rates of 0.0240 and 0.289 m³/s

Initial Condition	Variable	Case Study 0.0240 m³/s	Case Study 0.289 m³/s
Plume radius (m)	$r_{p,0}$	0.0250	0.0250
Centerline plume velocity (m/s)	u_0	3.00	40.0
Water temperature (K)	T_0	293	293
Bubble temperature (K)	$T_{b,0}$	293	293
Salinity (g/kg)	S_0	0	0
Dissolved O_2 concentration (mol/m³)	$C_{O_2,0}$	0	0
Bubble diameter (m)	$d_{b,0}$	0.003 to 0.005	0.003 to 0.005
Water volumetric flow (m³/s)	Q_0	0.0129	0.0217
Momentum (m⁴/s²)	M_0	0.0212	0.0598
Dissolved O_2 molar flow (mol/s)	$\dot{N}_{l,0}$	0	0
Gaseous O_2 molar flow (mol/s)	$\dot{N}_{g,0}$	0.0937	0.207

Three conditions were studied to validate the Milgram (1983) case study: (1) no dissolution with a constant slip velocity of 0.23 m/s and bubble diameters of 3 to 5 mm, (2) dissolution of air bubbles at a constant slip velocity of 0.23 m/s and bubble diameters of 3 to 5 mm, and (3) dissolution of air bubbles with a slip velocity that changes with phase fraction and bubble diameters of 3 to 5 mm. The constant bubble velocity case studies and the slip velocity that changes with gas phase fraction case study was performed using $\lambda = 0.8$, $\alpha = 0.11$, and $\gamma = 1.35$. The plume radius and centerline plume velocity of Milgram (1983) for flow rates of 0.024 and 0.289 m³/s are illustrated in Figure 3.8.
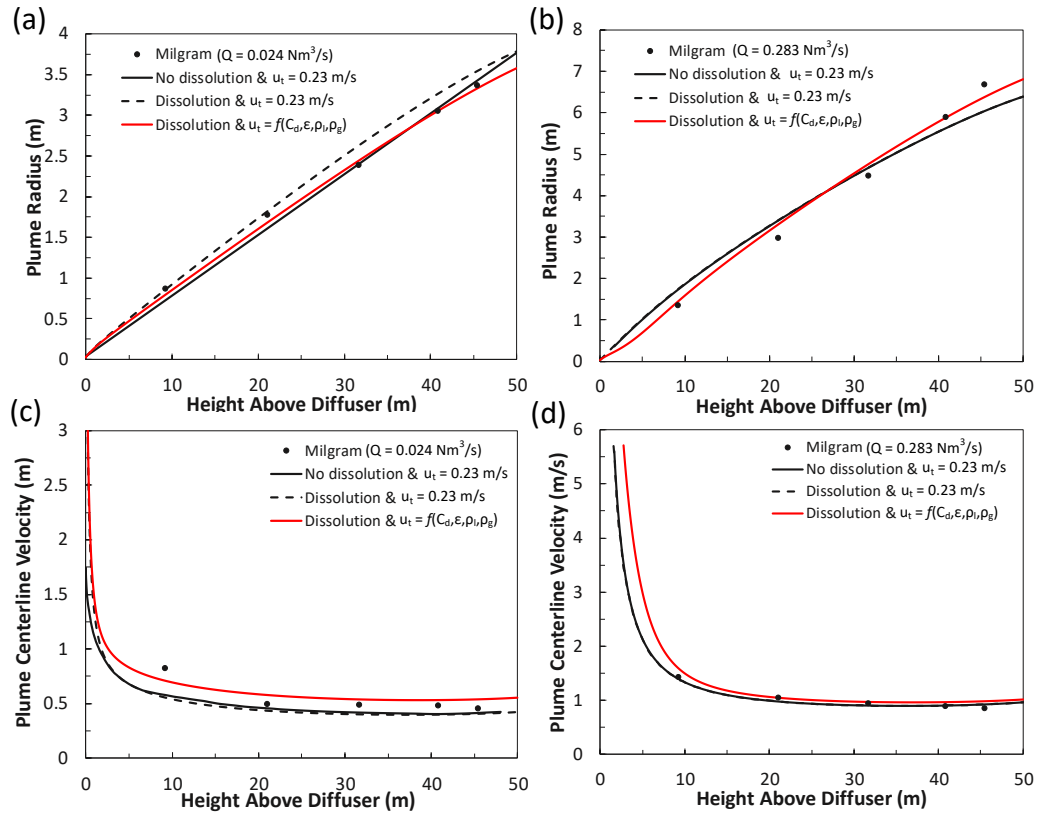
Figure 3.8: Comparison between the present model and the experimental data of Milgram (1983) for (a) plume radius for a flow rate of 0.024 m³/s (b) plume radius for a flow rate of 0.289 m³/s (c) plume centerline velocity for a flow rate of 0.024 m³/s, and (d) plume centerline velocity for a flow rate of 0.289 m³/s

There was no significant difference for the plume radius and plume centerline velocity for bubble size between 3 and 5 mm; therefore, like the Fanneløp & Sjøen case studies, only the results for the 3 mm bubble are shown. Additionally, there is a small difference between the dissolution and no dissolution case studies. The addition of a slip velocity as a function of the drag coefficient and swarm correction provided a comparable fit to the Milgram (1983) experimental data. The Froude number procedure to estimate the initial centerline plume velocity provided a reasonable prediction of the jetting velocity even though the intention was to ignore it.

3.4.2 Mass Transfer Validation Case Studies

3.4.2.1 DeMoyer et al. (2003) Case Study

To validate the mass transfer rate from the bubbles to the liquid, the experimental data of DeMoyer et al. (2003) were compared to the present model. The DeMoyer et al. (2003) case study was selected because the experiment is similar to the operational specifications of diffusers used in aquaculture. DeMoyer et al. (2003) were interested in determining the primary location of O_2 transfer in a diffused aeration system by examining the free surface-water interactions, and the bubble-water interactions. The aeration tests were conducted at the US Army Corps of Engineers Research and Development Center in Vicksburg, MS using a cylindrical tank with a depth of 9.25 m and a diameter of 7.60 m. Oxygen-enriched air (26.6 mol % O_2 and 73.4 mol % N_2) was injected at flow rates between 0.024 and 0.037 m^3/s through a stainless steel 0.305 m coarse bubble diffuser mounted 0.9 m from the tank bottom. The coarse bubble diffuser used in DeMoyer et al. (2003) is designed to produce bubbles with diameters between 3 and 5 mm; however, no direct measurements of the bubble size was conducted during the experiment. The air used for the experiments was delivered to a compressor at a temperature of 20°C and a pressure of 101 325 Pa and compressed to the hydrostatic pressure at the bottom of the tank. The water in the tank was at a temperature of 31°C and was chemically deoxygenated using sodium sulfite to reduce the DO concentration to approximately 2.39 mg/L before each experiment. The DO concentrations and temperatures were measured with four air-calibrated Hydrolab MiniSonde 4a multiprobes (Hydrolab, 2018) at various locations in the tank (DeMoyer et al., 2003); however, the exact locations in the tank were not disclosed. An Annotated diagram of the DeMoyer et al. (2003) experiments is illustrated in Figure 3.11.
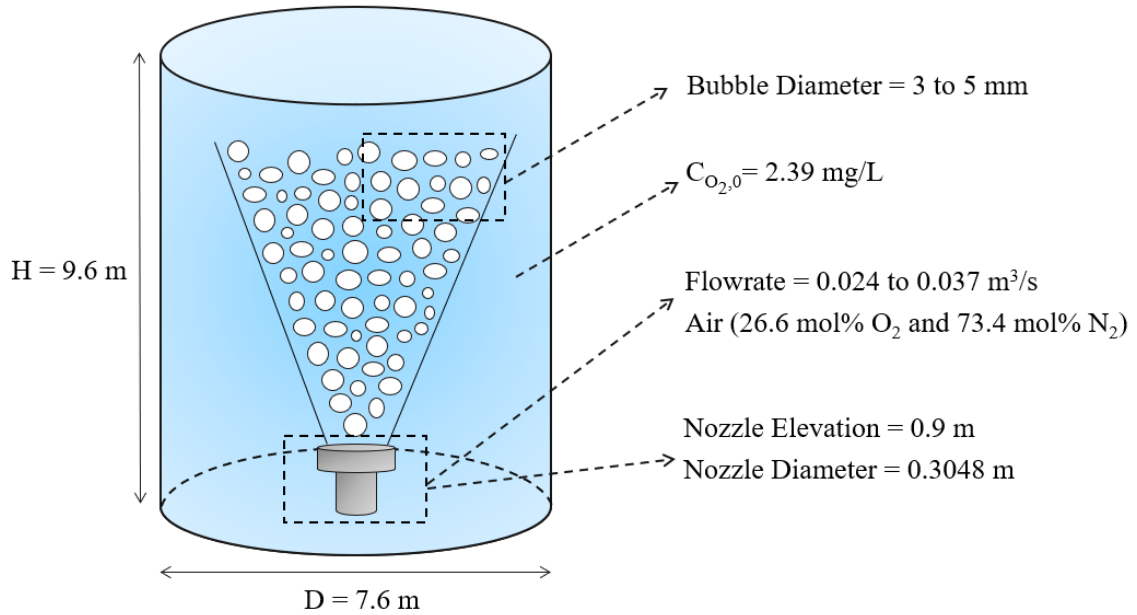
Figure 3.9: Annotated diagram of the DeMoyer et al. (2003) experiments

DeMoyer et al. (2003) performed two different experiments, one with a free surface where the surface water was exposed directly to the atmosphere, and a second test with the surface covered with 30 cm thick Styrofoam blocks everywhere except a 1.8 m diameter hole directly above the plume. The water surface mass transfer coefficient for the first experiment was 3.5 m/s and 0.51 m/s outside the plume. In the second experiment the water surface mass transfer coefficient was 3.87 m/s above the plume. For both experiments, there was significant mass transfer from the atmosphere to the surface of the water. In the present model the water surface mass transfer coefficient was neglected because the bubble transfer mass coefficient was on average 70% larger in the DeMoyer et al. (2003) experiments. To solve the case studies for an air flow rate of 0.024 m^3/s, the initial conditions in Table 3. were used.

Table 3.8: Initial Conditions Used for DeMoyer et al. (2003) Case Study for a Flow Rate of 0.024 m³/s

Initial Condition	Variable	Case Study 0.024 m³/s
Plume radius (m)	$r_{p,0}$	0.152
Centerline plume velocity (m/s)	u_0	1.29
Water temperature (K)	T_0	304
Bubble temperature (K)	$T_{b,0}$	293
Salinity (g/kg)	S_0	0
Dissolved O_2 concentration (mol/m³)	$C_{O_2,0}$	0.0747
Bubble diameter (m)	$d_{b,0}$	0.003 to 0.005
Water volumetric flow (m³/s)	Q_0	0.094
Momentum (m⁴/s²)	M_0	0.121
Dissolved O_2 molar flow (mol/s)	$\dot{N}_{l,0}$	0.00703
Gaseous O_2 molar flow (mol/s)	$\dot{N}_{g,0}$	0.163

The DeMoyer et al. (2003) case study was completed for bubble diameters of 3 to 5 mm and compared to the experimental data because the exact bubble diameter produced during the experiments was not measured. Additionally, values of $\lambda = 0.8$, $\alpha = 0.11$, and $\gamma = 1.35$ were used for the case studies. The DO concentrations in the case study were volume averaged because the exact location of the DO probes was not reported. The volume averaged DO concentration is calculated using

$$DO_{V_{avg}} = \frac{\sum \pi r_p^2 \Delta z C_{O_2}}{\pi r_p^2 H} \tag{3.53}$$

where $DO_{V_{avg}}$ is the volume-averaged DO concentration (mol/m³). A comparison between the measured DO concentrations in DeMoyer et al. (2003) and the predicted volume averaged DO concentration in the downflow region using the integral model for bubble sizes of 3 to 5 mm is illustrated in Figure 3.10.
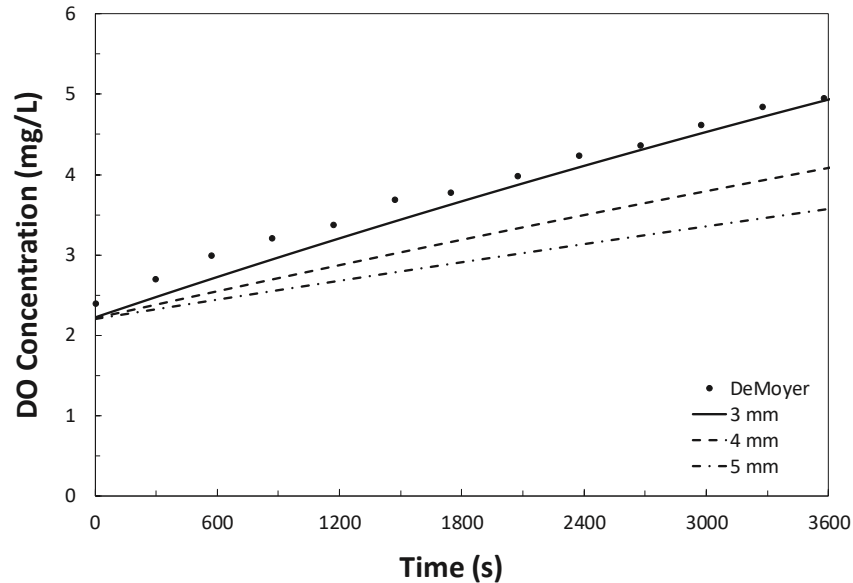
Figure 3.10: Comparison between DeMoyer et al. (2003) experimental free surface DO concentrations and the predicted volume averaged DO concentration in the downflow region using the integral model for bubble sizes of 3 to 5 mm with a flow rate of 0.024 m³/s

The volume-averaged DO concentration predicted using a 3 mm bubble in the present model provided the best fit to the data of the DeMoyer et al. (2003) free surface experiment, except for an underprediction during the first 1500 seconds of the experiment. A bubble size of 3 mm appears to provide a reasonable prediction of the mass transfer and agrees with DeMoyer's suggested bubble sizes in the range of 3 to 5 mm. It is clear from Figure 3.10 that the present model using a 4 and 5 mm bubble underpredicted the DO concentration profile for the free surface experiment of DeMoyer et al. (2003). No comparison was made to the DeMoyer et al. (2003) covered surface experiment because the data was not available. The locations of the DO probes in the tank were not reported, and it was not clear if the DO concentrations reported in DeMoyer et al. (2003) were volume-averaged or point measurements from one probe in the tank. Therefore, the DO concentrations at specific heights in the tank were investigated using the present model for a 3 mm bubble. Ten equal cross-sections or 0.925 m intervals of the tank were used for the *Ambient Function* of the present model. A comparison between the DeMoyer et al. (2003) experimental free surface DO concentration data and the predicted DO concentration

profiles from the present model using a 3 mm bubble size at a flow rate of 0.024 m³/s are illustrated in Figure 3.11 for heights of 0.925, 4.625, and 9.25 m above the diffuser.
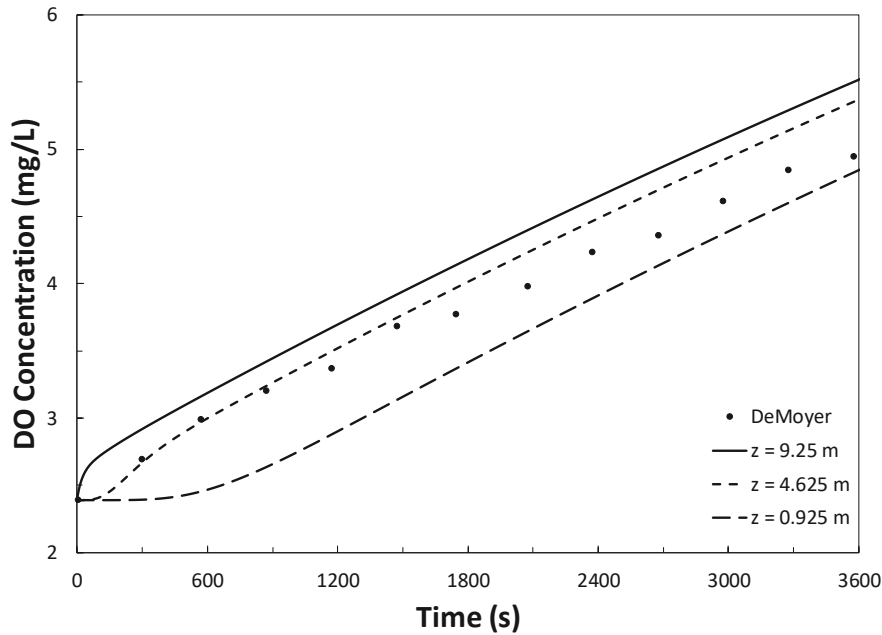

Figure 3.11: Comparison between the DeMoyer et al. (2003) experimental free surface DO concentration data and the predicted DO concentration profiles from the present model using a 3 mm bubble at a flow rate of 0.024 m³/s for heights of 0.925, 4.625, and 9.25 m above the diffuser

The predicted DO concentration for heights of 0.925, 4.625, and 9.25 m above the diffuser indicates the DeMoyer et al. (2003) experimental free surface data falls within the DO concentration upper (9.25 m) and lower (0.925 m) bounds using the present model with a 3 mm bubble size. The DO concentration profiles do not provide all the information in regard to the mass transfer rate. Therefore, the results for the total OTR (bubble OTR plus the free surface OTR) and the bubble OTR from the DeMoyer et al. (2003) free surface experiment were compared to the present model using a 3 mm bubble. In the DeMoyer et al. (2003) experiments the total OTR was a measured value, the bubble OTR was calculated, and the surface OTR was estimated by subtracting the bubble OTR from the total OTR. A comparison of the DeMoyer et al. (2003) free surface experimental total and bubble OTR (gO_2 m^{-3} h^{-1}) to the predicted OTR using the present model for bubble sizes of 3 to 5 mm at a flow rate of 0.024 m³/s is illustrated in Figure 3.12.
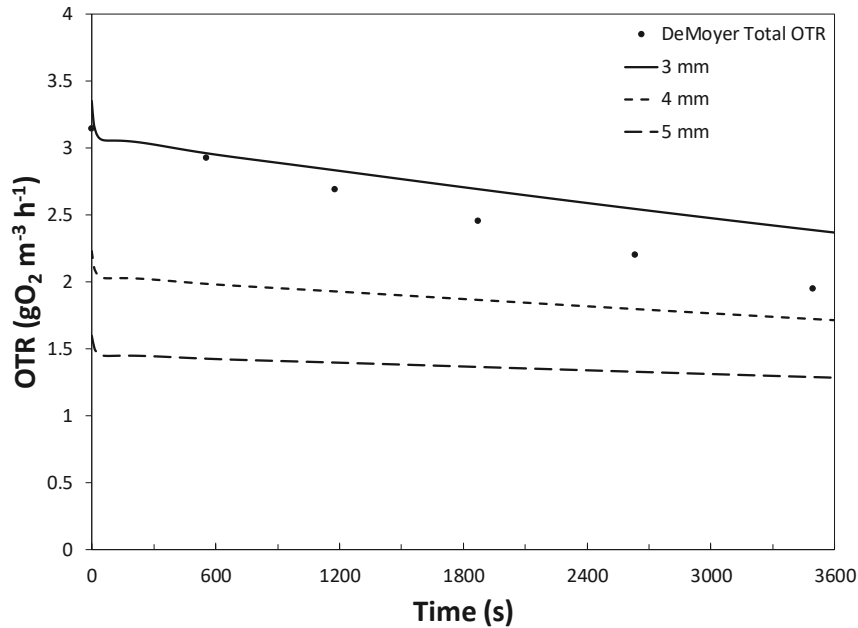
Figure 3.12: Comparison between the DeMoyer et al. (2003) free surface experimental total and bubble OTR to the predicted OTR using the present model for bubble sizes of 3 to 5 mm at a flow rate of 0.024 m³/s

The present model using a 3 mm bubble predicts the total OTR well but overestimates the mass transfer given that the actual bubble distribution would not be mono-dispersed. A match was unachievable without accounting for the surface effects because the concentration driving force over time will be affected. To account for the differences seen in Figure 3.12, the liquid-film mass transfer coefficient could be varied to tune the model and match the experimental data. Additionally, a source term could be added to the top of the computational boundary to account for surface mass transfer. It should be noted that the model DeMoyer et al. (2003) used to back-calculate the bubble OTR was not a standard bubble plume model. Therefore, tuning the present model to the DeMoyer et al. (2003) total OTR results could introduce error when the methods used for the mass transfer coefficient calculation cannot be directly compared to the present approach. It should be noted that the DeMoyer et al. (2003) free surface experimental results indicate that surface OTR is between 40 and 52% of the total OTR, which is extremely large for the system. In the present model, the total bubble surface area at steady state for a 3 mm bubble would be 381.7 m² (assuming the effects of decompression on the bubble and volume loss from the bubble as a result of mass transfer to the liquid are equal). The total surface of the bubbles in the system is significantly larger compared to the area of the free-surface which is 46

m^2. It is unlikely that 40 to 52% of the total OTR would be due to mass transfer from the surface assuming a similar concentration driving force and surface renewal rate. Even with a mean bubble size approaching 3 to 4 mm, the calculated area ratios from the present model suggest that the surface OTR accounts for approximately 10% to 15% of the total OTR.

3.4.2.2 Buscaglia et al. (2002) Case Study

To further validate the mass transfer rate from the bubbles to the liquid and the effect of decompression on the bubble as it rises towards the surface, the integral model results of Buscaglia et al. (2002) were compared to results of the present model. Buscaglia et al. (2002) were interested in the comparison between integral models and computational fluid dynamic simulations for bubble plume modeling. Using both methods, Buscaglia et al. (2002) simulated the McCook Reservoir in Chicago, Illinois. Atmospheric air (21 mol% O_2 and 79 mol% N_2) was injected at a depth of 77 m through a diffuser 0.65 m in diameter. The diffuser produced bubbles with a diameter of 5 mm, and the ambient concentrations were 1 mg/L and 0.28 mg/L of DO and DN, respectively. An annotated diagram of the McCook Reservoir simulations is illustrated in Figure 3.13.
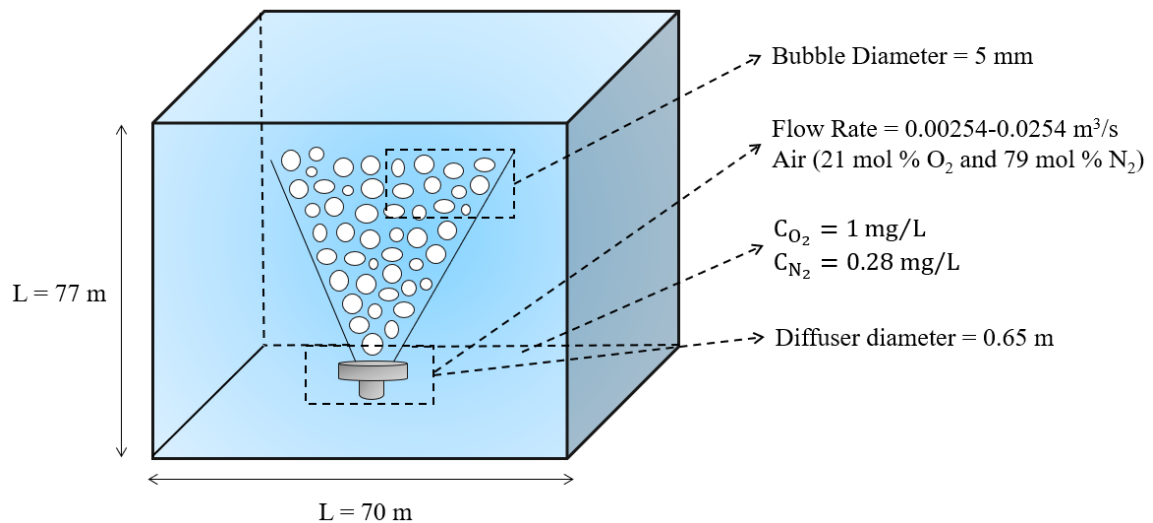
Figure 3.13: Annotated diagram of the Buscaglia et al. (2002) simulations

To solve the Buscaglia case studies for flow rates of 0.00254 and 0.0254 m^3/s, the initial conditions in Table 3. were used.

Table 3.9: Initial Conditions Used for Buscaglia et al. (2003) Case Study for Flow Rates of 0.00254 and 0.0254 m³/s

Initial Condition	Variable	Case Study	
		0.00254 m³/s	**0.0254 m³/s**
Plume radius (m)	$r_{p,0}$	0.325	0.325
Centerline plume velocity (m/s)	u_0	0.293	0.717
Water temperature (K)	T_0	293	293
Bubble temperature (K)	$T_{b,0}$	293	293
Salinity (g/kg)	S_0	0	0
Dissolved O_2 concentration (mol/m³)	$C_{O_2,0}$	0.0313	0.0313
Bubble diameter (m)	$d_{b,0}$	0.005	0.005
Water volumetric flow (m³/s)	Q_0	0.000972	0.00238
Momentum (m⁴/s²)	M_0	0.000285	0.00170
Dissolved O_2 molar flow (mol/s)	$\dot{N}_{l,0}$	3.04×10^{-5}	7.43×10^{-5}
Gaseous O_2 molar flow (mol/s)	$\dot{N}_{g,0}$	0.0246	0.246

Additionally, values of $\lambda = 0.8$, $\alpha = 0.11$, and $\gamma = 1.35$ were used for the present model. A comparison between the present integral model and that of Buscaglia et al. (2002) for a flow rate of 0.00254 m³/s is illustrated in Figure 3.14.
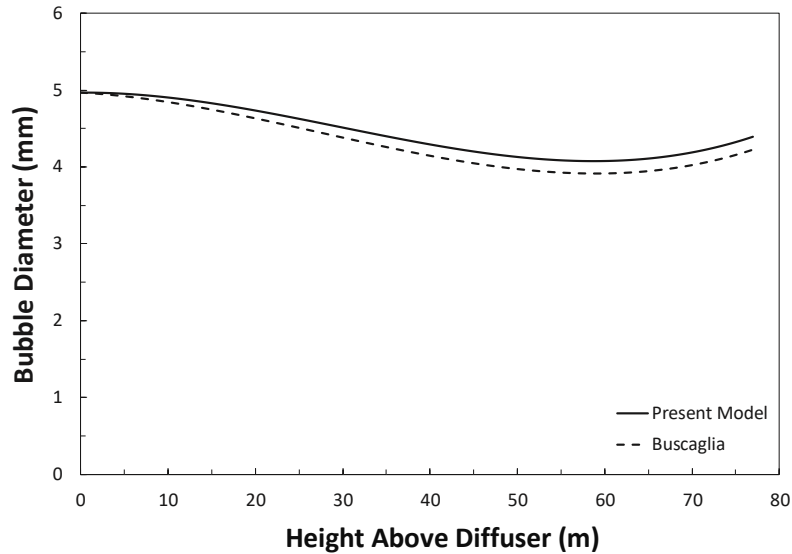
Figure 3.14: Bubble diameter comparison between the present model and the integral model of Buscaglia et al. (2002) for a flow rate of 0.00254 m³/s

For the low flow rate case, the present integral model predicts results similar to those obtained by Buscaglia et al. (2002). There is a zone dominated by bubble dissolution for the first 50 m followed by a zone of bubble expansion where the bubble diameter increases. The present model slightly underpredicts the mass transfer but overpredicts the bubble expansion compared to Buscaglia et al. (2002). There is no experimental data available to distinguish between the two models because Buscaglia et al. (2002) only performed simulations. However, the difference between the two models can be explained by the bubble slip velocity and the liquid-film mass transfer coefficient. Buscaglia et al. (2002) used a constant slip velocity of 0.23 m/s whereas the present model used a variable bubble radius as a function of the drag coefficient and the gas phase fraction. The bubble terminal velocity is used in the estimation of the bubble radius and can explain some of the variances in the zone of bubble expansion predicted by the two models. Buscaglia et al. (2002) also used a constant k_l from Wüest et al. (1992) and assumed the same k_l for both O_2 and N_2. The Hughmark (1967) and Wüest et al. (1992) k_l as a function of bubble diameter (mm) are illustrated in Figure 3.15.
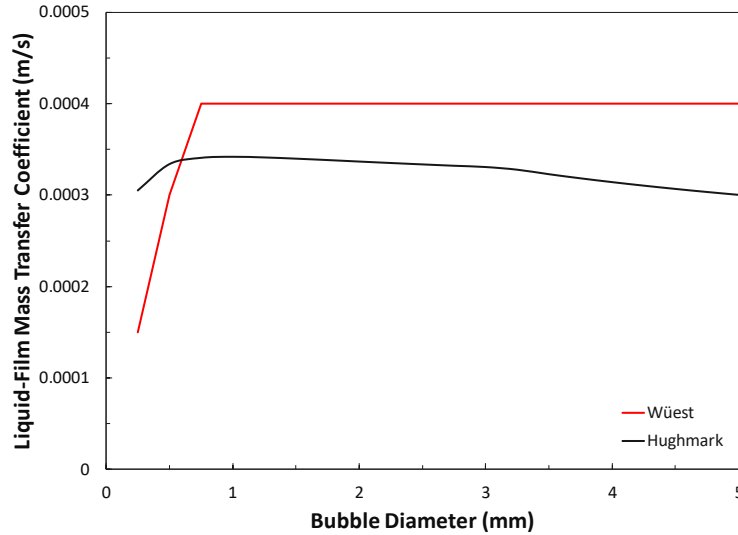
Figure 3.15: Hughmark (1967) k_l used in the present study and Wüest et al. (1992) k_l used in Buscaglia et al. (2002)

The Wüest et al. (1992) k_l is larger than the Hughmark (1967) k_l, which can explain the difference in the mass transfer zone between the two models. Additionally, Buscaglia et al. (2002) use the Gaussian self-similarity profile for the integral model and the present model uses the Tophat self-similarity profile. A comparison between the bubble diameter profile predicted by the present integral model and that of Buscaglia et al. (2002) for a flow rate of 0.0254 m^3/s is illustrated in Figure 3.16.
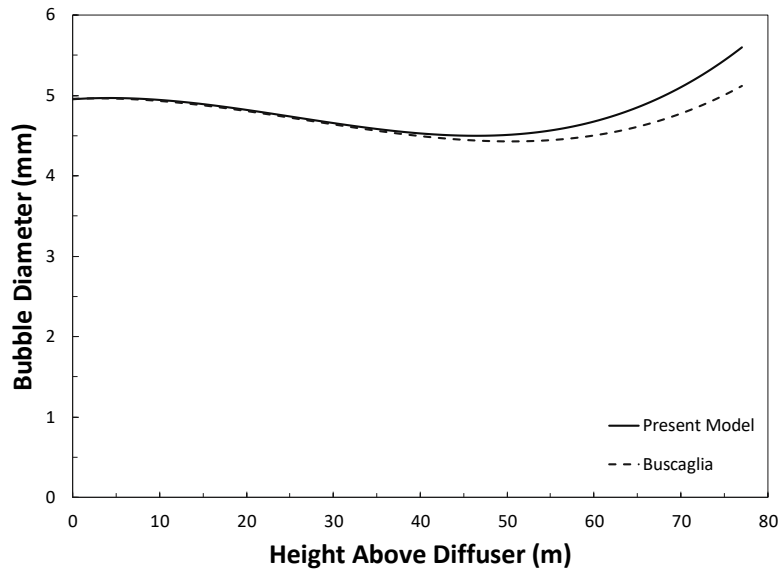

Figure 3.16: Bubble diameter comparison between the present integral model and that of Buscaglia et al. (2002) for a flow rate of 0.0254 m^3/s

71

For the high flow rate case, the present integral model predicts similar behaviour to that predicted by Buscaglia et al. (2002). There is a zone dominated by slight bubble dissolution for the first 50 m followed by a zone of bubble expansion. The present model overpredicts the bubble expansion but appears to predict a mass transfer rate similar to that found by Buscaglia et al. (2002). It appears that for low flow rates, the mass transfer coefficient is the dominating variable indicated by the similar profiles in Figure 3.14. For the higher flow rates, the bubble slip velocity is the dominant variable.

3.5 Conclusions

A bubble plume model using an integral approach was coupled with an ambient environment model and solved using a novel method in MATLAB® and Simulink®. The integral model differed from previous approaches by incorporating a relationship for the bubble terminal velocity with a swarm correction. The model was validated using hydrodynamic studies from Fanneløp & Sjøen (1980) and Milgram (1983), and mass transfer studies from DeMoyer et al. (2003) and Buscaglia et al. (2002).

With validation of the hydrodynamics, mass transfer correlations and transient bubble size behaviour complete, the next step is to apply the validated plume model for large-scale case studies of open-ocean aeration systems with DO consumption rate by Atlantic salmon. The objectives are to accurately predict the number of diffusers, the optimal spacing between the diffusers, and the flow of gas required for both air and enriched air streams to maintain the DO concentration above 6 mg/L in an open-ocean pen.

# Chapter 4: Modeling of Open-Ocean Aeration Systems

4.1 Introduction

The coastal regions of Nova Scotia are prone to natural fluctuations in both water temperature and DO levels, leading to consequences that have a negative impact on the health and growth of Atlantic salmon in open-ocean pens. The fluctuating temperature and DO levels have created a need for mitigation strategies in the Nova Scotian aquaculture industry. An aeration system that allows for the delivery of supplemental O_2 to aquaculture pens on demand during conditions of low DO will improve key performance indicators significantly, reduce episodic stress and mortality due to low O_2, and increase production efficiency, stability, and environmental sustainability of the aquaculture industry in Nova Scotia.

To summarize Chapter 2, the minimum DO concentration to protect the Atlantic salmon from adverse health effects, such as acute stress responses and reduced growth, is 6 mg/L. The normal O_2 consumption rate of Atlantic salmon ranges between 2 and 4 mgO$_2$ kgFish^{-1} min^{-1}. Therefore, an aeration system must meet or exceed the O_2 consumption rate of the salmon. Fine bubble diffusers are the recommended method for aerating in open-ocean aquaculture because the diffusers have a high SAE (between 1.8 and 3.9 kgO$_2$/kWh) and can deliver high flow rates of air or O_2-enriched air.

In this chapter, a large-scale case study investigating the aeration of an open-ocean salmon pen that has a constant O_2 consumption rate of 2 mg O_2 kg Fish^{-1} min^{-1} was performed. The bubble plume integral model coupled with the ambient environment model from Chapter 3 will be used to evaluate the number of diffusers, placement of diffusers, and volume of air or enriched air required to keep the DO concentration in the open-ocean pens above the recommended minimum of 6 mg/L. An economic analysis will be performed based on the required flow rate, the use of air or O_2-enriched air, the compression requirements, and the O_2 generation requirements.

4.2 Model Formulation

The bubble plume and ambient environment conservation equations derived in Chapter 3 are used to model the large-scale case; however, now a DO consumption term for the Atlantic salmon (DO_{fish}), as described in Chapter 2, is applied to the ambient environment conservation equation (Figure 4.1). The ambient environment control volume with the DO consumption term is illustrated in Figure 4.1.
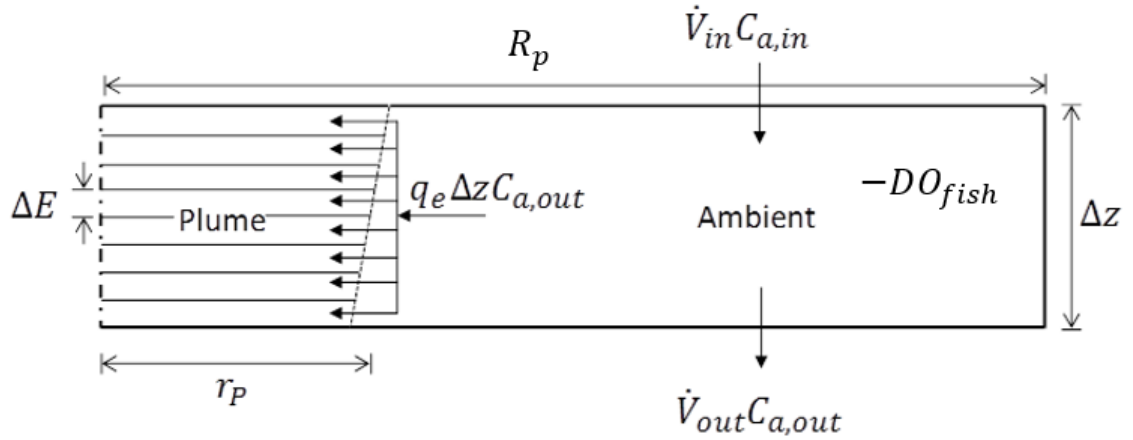
Figure 4.1: Ambient environment conservation equation with DO consumption term

The assumptions used in the model include: (1) interactions between the Atlantic salmon and the plume are neglected (salmon do not alter the flow of the plume), (2) mixing due to the salmon swimming is neglected, and (3) the Atlantic salmon consume DO equally inside and outside the plume. The resulting ambient environment conservation equation is

$$\left(\pi\left(R_p^2 - r_p^2\right)\Delta z\right)\frac{dC_a}{dt} = \dot{V}_{in}C_{a,in} - \dot{V}_{out}C_{a,out} + q_d C_p \Delta z - q_e C_a \Delta z \tag{4.1}$$

where DO_{fish} is the consumption rate of the Atlantic salmon (mol m^{-3} s^{-1}). The OTR (mol m^{-3} s^{-1}) summarized in Chapter 2 can be locally calculated in the plume using

$$\text{OTR} = \frac{dC}{dt} = k_l a\left(H_{O_2}P_{O_2} - C_{O_2}\right) \tag{4.2}$$

where k_l is the convective liquid-film mass transfer coefficient (m/s), a is the ratio of the air-water interfacial area to volume (m^{-1}), H_{O_2} is the Henry's law constant for O$_2$ (mol m^{-3}

Pa^{-1}), P_{O_2} is the partial pressure of O$_2$ (Pa), and C_{O_2} is the concentration of O$_2$ inside the plume (mol/m^3). As summarized in Chapter 2, a more useful way to show the OTR is the SAE according to

$$SAE = \frac{OTR}{\dot{W}} \tag{4.3}$$

where $\dot{W}$ is the power of the aeration system (kW). The power requirements of the aeration system should consider the compression of air or O$_2$-enriched air to the hydrostatic pressure at the depth of the diffuser, and the pressure drop through the length of piping from the compressor to the diffuser, and the pressure drop through the diffuser.

4.2.1 Pressure Drop through Piping and Diffuser

The optimal pipe diameter (based on economics) for turbulent flow in steel pipes with an inside diameter ≥ 0.0254 m can be estimated using (Peters, Timmerhaus & West, 2003)

$$d_{opt} = 0.363\dot{V}_{std}^{0.45}\rho_g^{0.13} \tag{4.4}$$

where d_{opt} is the optimal inside pipe diameter (m), $\dot{V}_{std}$ is the gas volumetric flow rate at standard conditions (m^3/s) and ρ_g is the gas density (kg/m^3). The pressure drop over the length of pipe can be estimated using the Darcy-Weisbach equation for turbulent flow (McCabe, Smith & Harriott, 2004)

$$\Delta P_p = \frac{fL\rho_g u^2}{2d_{opt}} \tag{4.5}$$

where ΔP_p is the pressure drop through the length of pipe (Pa), L is the length of pipe (m), f is the Darcy friction factor (dimensionless), and u is the gas velocity in the pipe (m/s), To estimate the Darcy friction factor, the Colebrook-White equation is used (McCabe, Smith & Harriott, 2004)

$$\frac{1}{\sqrt{f}} = -2\log\left(\frac{\varepsilon}{3.7d_h} + \frac{2.51}{Re\sqrt{f}}\right) \tag{4.6}$$

where ε is the pipe roughness (m), d_h is the hydraulic diameter (m), and Re is the Reynolds number of the fluid (dimensionless). The total pressure drop (P_t) can be estimated using

$$P_t = \Delta P_d + \Delta P_p + P_0 \tag{4.7}$$

where ΔP_d is the pressure drop across the diffuser (Pa), ΔP_p is the pressure drop through the length of pipe (Pa), and P_0 is the hydrostatic pressure at the diffuser depth (Pa).

4.2.2 Compression of Air and Oxygen-Enriched Air

To estimate the power required to compress the air and O_2-enriched air, the integral between the suction pressure and discharge pressure (McCabe, Smith & Harriott, 2004) is evaluated using

$$W_s = \int_{P_1}^{P_2} \frac{dP}{\rho} \tag{4.8}$$

For an ideal gas undergoing reversible adiabatic compression the gas will follow an isentropic path where the relation between P and ρ is

$$\frac{P}{\rho^\gamma} = \frac{P_1}{\rho_1^n} \tag{4.9}$$

where $n = \frac{c_p}{c_v}$ (dimensionless). Eq. 4.9 can be rearranged for density to produce

$$\rho = \frac{\rho_1}{P_1^{1\backslash n}} P^{1\backslash n} \tag{4.10}$$

Substituting ρ from Eq. 4.10 into the integral for the work of compression on an ideal gas (Eq. 4.8) and then integrating results in

76

$$W_s = \frac{P_1^{1\backslash\gamma}}{\rho_1} \int_{P_1}^{P_2} \frac{dP}{P^{1\backslash\gamma}} = \frac{P^{1\backslash\gamma}}{(1 - 1\backslash\gamma)\rho_1} \left(P_2^{(1-1\backslash\gamma)} - P_1^{(1-1\backslash\gamma)} \right) \tag{4.11}$$

Multiplying W_s by $P_1^{(1-1\backslash\gamma)}$ and dividing the terms in the parentheses by the same quantity results in

$$-W_s = \frac{\gamma}{\gamma - 1} \left(\frac{RT_1}{MW} \right) \left[\left(\frac{P_2}{P_1} \right)^{\frac{n-1}{n}} - 1 \right] \tag{4.12}$$

where $\frac{P}{\rho} = \frac{RT}{MW}$. When the efficiency is not 100%, the power can be evaluated using

$$\dot{W} = \frac{-W_s \dot{m}}{\eta} \tag{4.13}$$

where η is the efficiency (dimensionless) and $\dot{m}$ is the mass flow rate of the fluid (kg/s). For the purposes of calculations in this chapter, the efficiency of the compressor is assumed to be 75%. With adiabatic compression, the temperature increase of the fluid is proportional to the pressure increase by

$$\frac{T_2}{T_1} = \left(\frac{P_2}{P_1} \right)^{\frac{n-1}{n}} \tag{4.14}$$

4.3 Large-Scale Case Setup

A large-scale case study was set up in MATLAB® and Simulink® to evaluate the number of diffusers required, the placement of diffusers required, and volume of air or O_2-enriched air needed to keep the DO concentration in the open-ocean pen above the recommended minimum of 6 mg/L. Atmospheric air (21 mol% O_2) and O_2-enriched air (21-95 mol% O_2) were injected into a round pen 30 m in diameter and 15 m deep through five-trilobed diffusers. Each trilobed diffuser contains three 0.3048 m diameter discs operating at gas flow rates between 0 and 0.0085 m^3/s per disc at standard conditions or between 0 and 0.0255 m^3/s per trilobed diffuser at standard conditions, producing bubble diameters of approximately 1 mm (Pentair, 2018). The DO concentration in the open-ocean pen was initially 6 mg/L, the DN concentration in the pen was saturated, and the water salinity was

34 g/kg. A water temperature of 20°C was chosen to represent a worst-case scenario for open-ocean pens in Nova Scotia during the summer months of July, August, and September. An Atlantic salmon stocking density of 22 kg/m³ was chosen because this value is the recommended maximum stocking density of Atlantic salmon before adverse health effects become apparent. Open-ocean pens are generally deeper than 15 m; however, this value was chosen because it is the maximum operating depth of the trilobed diffuser (Pentair, 2018). An annotated diagram of the open-ocean aquaculture pen is illustrated in Figure 4.2.
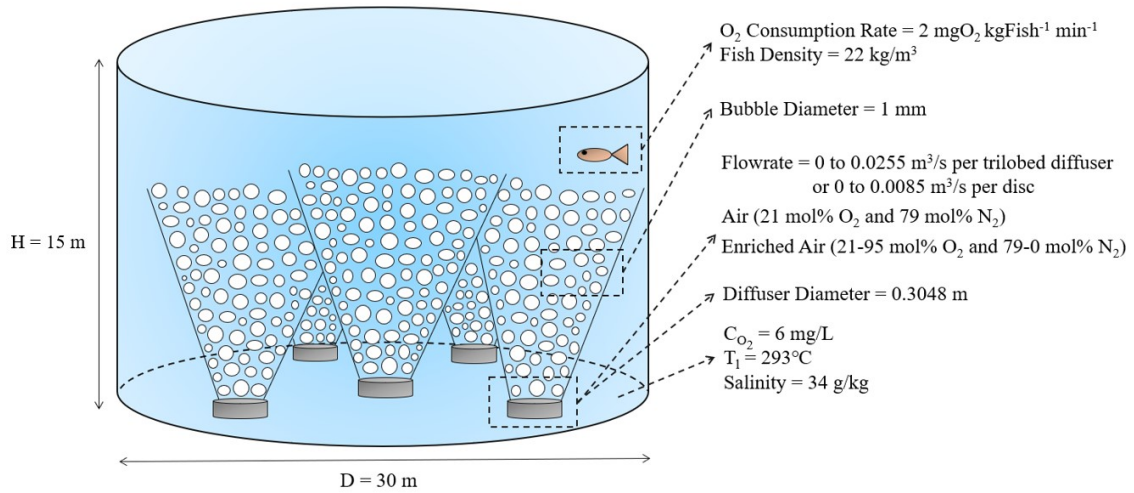
Figure 4.2: Annotated diagram of an open-ocean aquaculture pen

The required spacing of five-trilobed diffusers that will aerate the entire volume inside an open-ocean pen 30 m in diameter was determined by:

$$R_p = \sqrt{\frac{R_{pen}^2}{N}} \tag{4.15}$$

where R_p is the radius of the aerated volume (m), R_{pen} is the radius of the aquaculture pen (m), and N is the number of required diffusers (dimensionless). The radius of the aerated volume using one trilobed diffuser was estimated to be 6.7 m. The spacing using five Pentair trilobed diffusers in a 30 m diameter pen is illustrated in Figure 4.3.
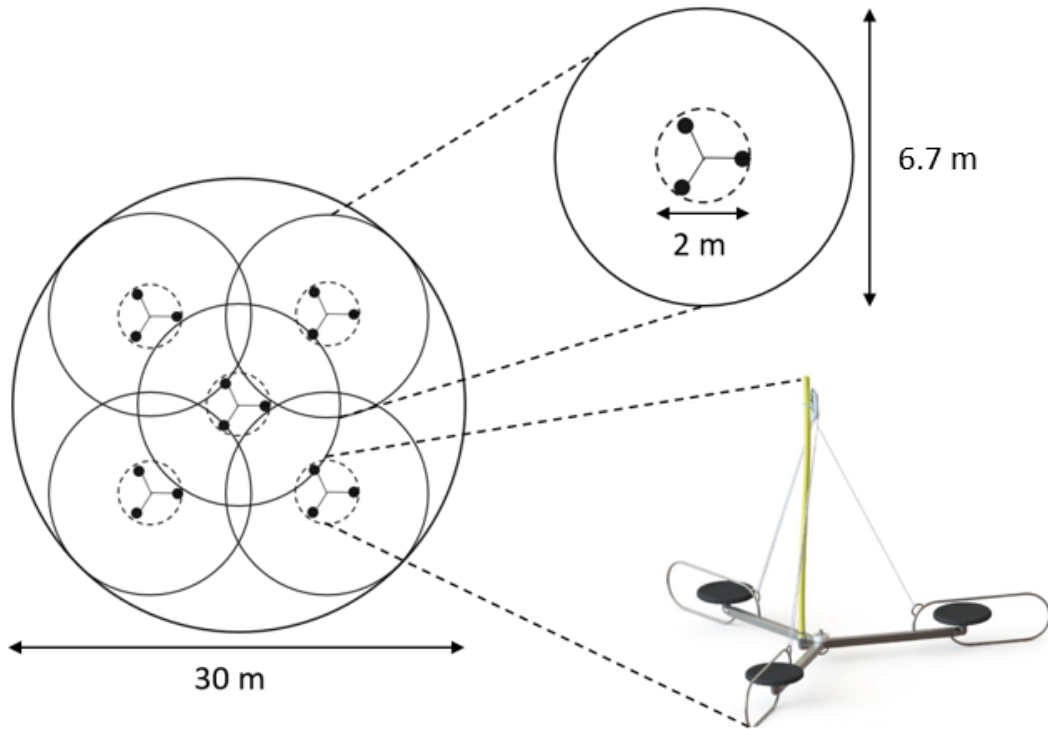
Figure 4.3: Spacing requirements for five Pentair trilobed diffusers fully aerating a 30 m diameter open-ocean pen (Pentair, 2018)

The individual discs used in the trilobed diffusers are a FlexAir® fine bubble membrane disc diffuser illustrated in Figure 4.4.

① Threaded 3/4 inch male NPT connector
② Glass-filled polypropylene diffuser base
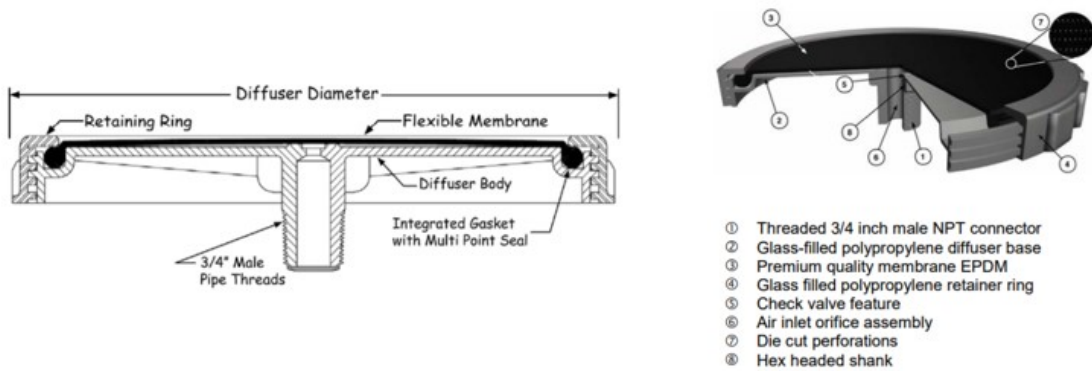③ Premium quality membrane EPDM
④ Glass filled polypropylene retainer ring
⑤ Check valve feature
⑥ Air inlet orifice assembly
⑦ Die cut perforations
⑧ Hex headed shank

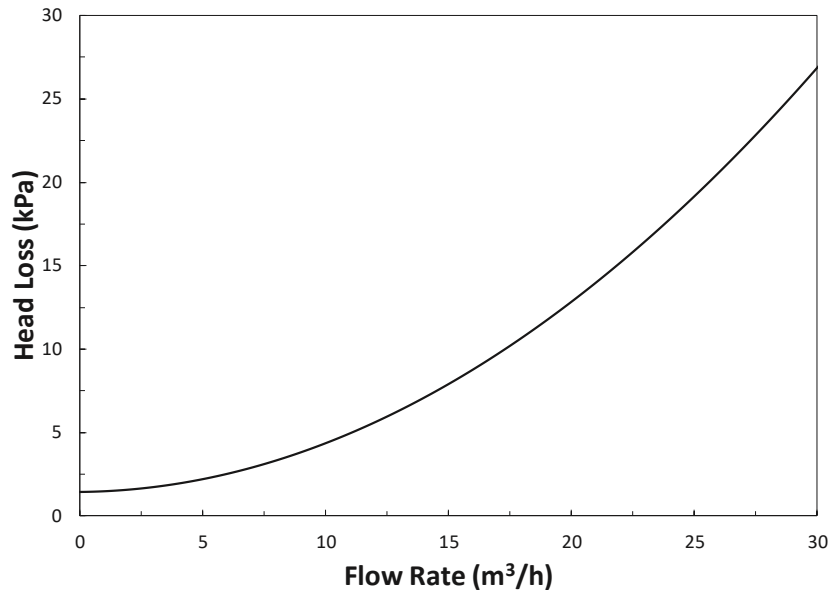**Figure 4.4: FlexAir® fine bubble disc diffuser diagram (FlexAir, 2018)**

The Pentair trilobed diffusers use the high capacity 0.3048 m FlexAir® membrane discs. The high capacity diffuser has a design flow rate between 3.4 and 22.1 m³/h with a peak

flow rate of 28.4 m^3/h. The specifications for the 0.3048 m high capacity FlexAir® disc diffusers are provided in Table 4.1.

Table 4.1: FlexAir® Flexible Membrane Fine Bubble Disc Diffuser Specifications (FlexAir, 2018)

Nominal Disc Size	Peak Airflow (m^3/h)	Design Airflow (m^3/h)	Diffuser Diameter (m)	Active Surface Area (m^2)
0.3048 m High Capacity	28.4	3.4-22.1	328	0.059

The pressure drop through the high capacity disc is 28 kPa for the peak airflow of 28.4 m^3/h. The pressure drop across the 0.3048 m high-capacity FlexAir® fine-bubble membrane disc diffuser for flow rates between 0 and 30 m^3/h is illustrated in Figure 4.5.

Figure 4.5: Pressure drop through the 0.3048 m high capacity FlexAir® fine bubble membrane disc diffuser for the entire range of flow rates (FlexAir, 2018)

To operate the trilobed diffusers with O_2-enriched air (i.e. greater than 21 mol% O_2), an O2 generator is required to produce the enriched stream. The AirSep® O_2 generator is a common system used in aquaculture to produce O_2-enriched streams up to 95 mol% O_2 purity at flow rates between 26.29 and 34.18 m^3/h. The O_2 generator does not have an

internal compressor; therefore, the air feed needs to be compressed to 621 kPa. The AirSep® AS-L PSA O$_2$ generator specifications are provided in Table 4.2.

Table 4.2: AirSep® AS-L PSA O$_2$ Generator Specifications (The Oxygen Store, 2018)

Product Concentration	Product O$_2$ Flow (m^3/h)	Feed Pressure (kPa)	Product Pressure (kPa)
95 ± 1%	28.29 - 36.18	621	310 or 448

The AirSep® O$_2$ generator has a low efficiency because the generator requires significantly larger feed flow rates compared to the product flow rates. The low efficiency of the AirSep® O$_2$ generator is illustrated in Figure 4.6 for discharge pressures of 310 and 448 kPa showing the O$_2$ flow rates in the air feed and the O$_2$ product flow rate.
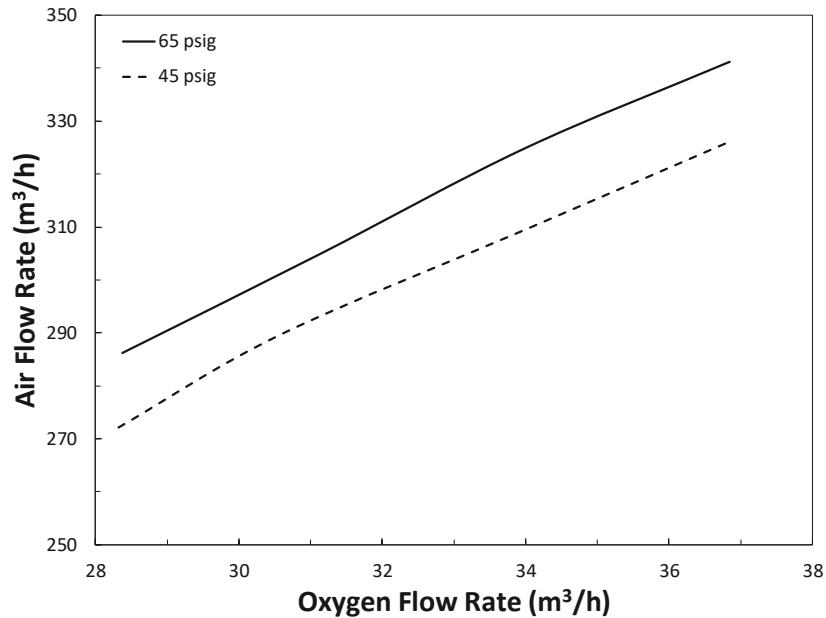
Figure 4.6: AS-L generator O$_2$ flow rate in feed for air and O$_2$ flow rate in product for discharge pressures of 310 and 448 kPa (The Oxygen Store, 2018)

A schematic showing the pressure requirements for pure air (stream A) and blended or pure O$_2$ (stream B) is illustrated in Figure 4.7.
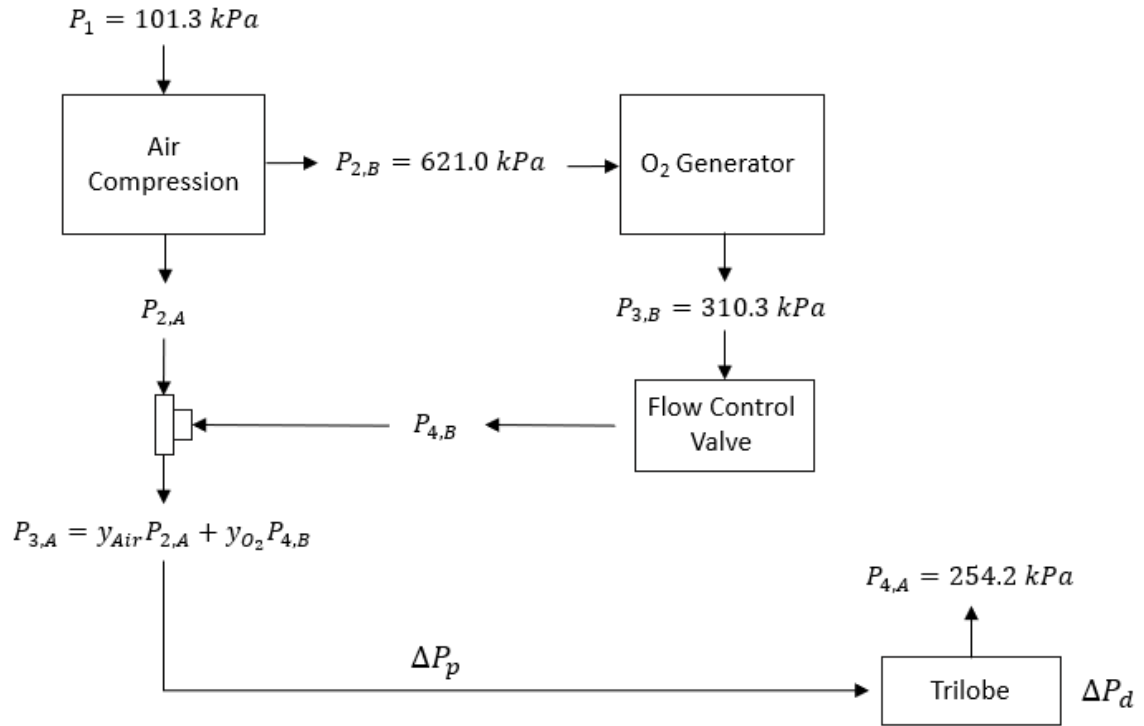
Figure 4.7: Pressure requirements for pure air (stream A) and blended or pure O₂ (stream B)

If air is used for aeration of an open-ocean pen 30 m in diameter, the air is compressed to a pressure ($P_{2,A}$) that overcomes the pressure drop of the length of piping from the compressor to the diffuser (ΔP_p), the pressure drop across the diffuser (ΔP_d), and the hydrostatic pressure of the water ($P_{4,A}$) at a depth of 15 m (254 kPa). If O₂-enriched air is used for aeration of an open-ocean pen 30 m in diameter, the stream is compressed to 621 kPa before entering the O₂ generator. The O₂-enriched stream exits the O₂ generator at a pressure of 310 kPa ($P_{3,B}$) and enters a flow control valve ($P_{4,B}$) that reduces the pressure before blending of streams occur. An air stream and the O₂-enriched stream are blended to the desired composition.

82

4.4 Large-Scale Case Results

4.4.1 Large-Scale Base Case Study

To determine how long it takes one trilobed diffuser aerating into a volume of 2149 m^3 (height of 15 m and radius of 6.7 m) to reach steady state, a base case for 1 mm air bubbles injected at 0.0254 m^3/s was simulated. The criteria for the simulation to reach steady state is when the OTR delivered by the trilobed diffusers is equal to the rate of DO consumption by the Atlantic salmon. The initial conditions used in the base case study are provided in Table 4.3.

Table 4.3: Initial Conditions for the Base Case Study

| Initial Condition	Variable	Case Study 0.0254 m^3/s
Plume radius (m)	$r_{p,0}$	1.00
Centerline plume velocity (m/s)	u_0	0.849
Water temperature (K)	T_0	293
Bubble temperature (K)	$T_{b,0}$	293
Salinity (g/kg)	S_0	34.0
Dissolved O_2 concentration (mol/m^3)	$C_{O_2,0}$	0.188
Bubble diameter (m)	$d_{b,0}$	0.001
Water volumetric flow (m^3/s)	Q_0	2.26
Momentum (m^4/s^2)	M_0	2.26
Dissolved O_2 molar flow (mol/s)	$\dot{N}_{l,0}$	0.425
Gaseous O_2 molar flow (mol/s)	$\dot{N}_{g,0}$	0.238

To ensure the base case reached steady state, the model was simulated for 86 400 s (24 h). Additionally, the minimum OTR for a consumption rate of 2 mgO_2 kgFish^{-1} min^{-1} was calculated to be 2.4 gO_2 m^{-3} h^{-1} and added to the calculated OTR to get the true OTR of the system. One of the main limitations of the model is that the radius at the top of the plume

cannot be greater than the aeration radius. The plume radius for an air flow rate of 0.0254 m^3/s and aeration radius of 6.7 m is illustrated in Figure 4.8.
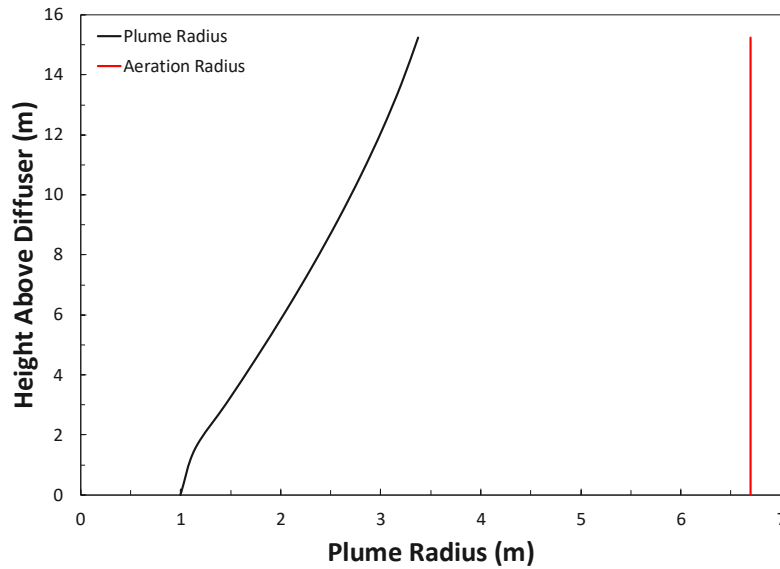
Figure 4.8: Plume radius for an air flow rate of 0.0254 m^3/s and aeration radius for one trilobed diffuser

The plume radius at the top of the plume is much less than the aeration radius; therefore, the base case study results are likely to provide reasonable predictions. To determine if one trilobed diffuser delivering air at a flow rate of 0.0254 m^3/s can meet the O_2 demand from the Atlantic salmon, the OTR and DO concentrations need to be investigated. The steady-state OTR ($gO_2 \ m^{-3} \ h^{-1}$) for a 1 mm air bubble injected at 0.0254 m^3/s is illustrated in Figure 4.9.
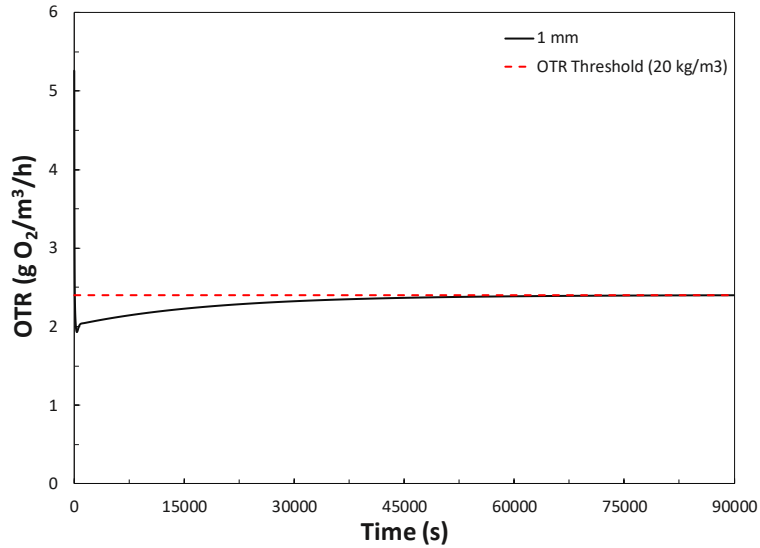
Figure 4.9: OTR for a 1 mm air bubble delivered at 0.0254 m³/s approaching the steady state OTR for an Atlantic salmon stocking density of 22 kg/m³

When the OTR rate approaches the threshold OTR, the simulation is at steady state. This occurs within 86 400 s (24 h) for a 1 mm air bubble delivered at 0.0254 m³/s. The OTR for a 1 mm air bubble delivered at 0.0254 m³/s for 0 and 24 h at various heights above the diffuser is illustrated in Figure 4.10.
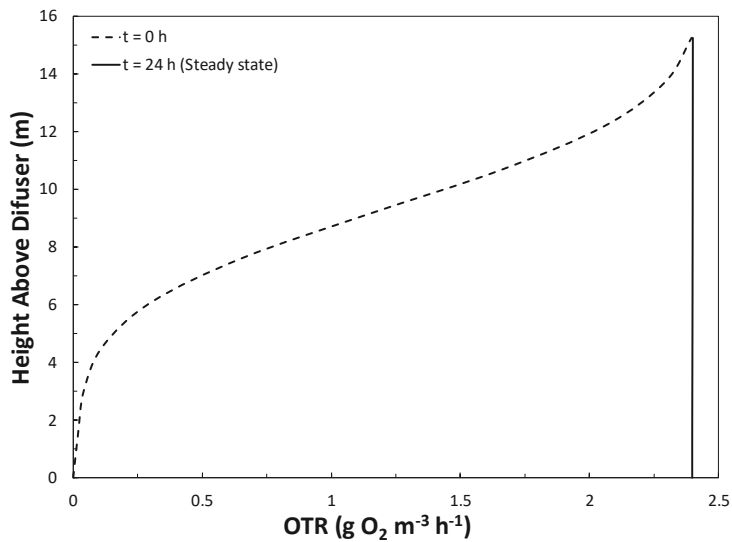
Figure 4.10: OTR for a 1 mm air bubble delivered at 0.0254 m³/s for 0 and 24 h at heights between 0 and 15 m above the trilobed diffuser

The OTR varies significantly for the different heights above the diffuser but approaches the value of 2.4 gO$_2$ m^{-3} h^{-1} at steady state. The concentrations in the plume and the ambient

environment are expected to be different as the mass transfer occurs in the plume and mixes over time in the ambient environment. The DO concentration in the plume and ambient environment for 0, 6, and 24 h for various heights above the trilobed diffuser are illustrated in Figure 4.11.
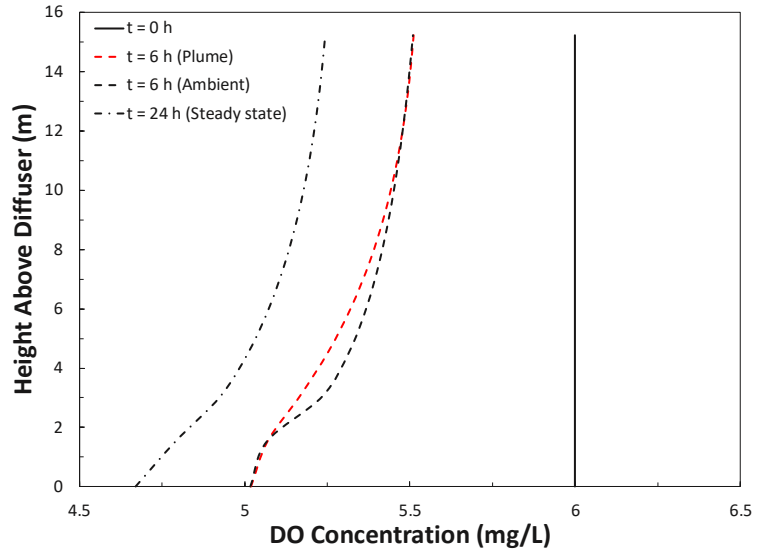
Figure 4.11: DO concentration in the plume and ambient environment for 0, 6, and 24 h for heights between 0 and 15 m above the trilobed diffuser

The DO concentration in the plume is greater than the ambient initially, but both concentration profiles approach each other at steady state. The change of the volume-averaged DO concentration in the ambient environment for a total of 24 h is illustrated in Figure 4.12.
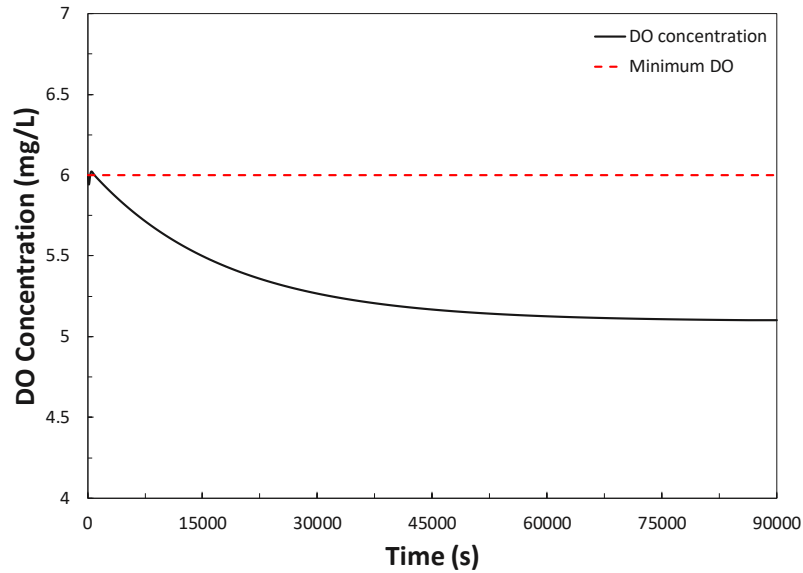
Figure 4.12: Volume-averaged DO concentration profile in the ambient environment for a 24 h period with the minimum DO

Although the OTR approaches the threshold OTR in Figure 4.12, the DO concentration profile indicates a trilobed diffuser delivering 0.0254 m^3/s of air into a 6.7 m aeration radius is not enough to maintain the minimum DO concentration of 6 mg/L to keep Atlantic salmon healthy. This implies that the driving force between the saturated DO concentration and 6 mg/L was insufficient to deliver the required OTR for the given aeration volume and conditions. There are several ways to overcome this limitation (e.g. smaller bubble sizes, higher gas flow rates, smaller aeration volumes, and O_2-enriched gas). Therefore, the analysis in the following sections focuses on determining the conditions for which both the minimum concentration and OTR can be achieved.

4.4.2 Diffuser Spacing Case Study

To determine the maximum aeration radius for a trilobed diffuser delivering 0.0254 m^3/s of air, a diffuser spacing case study was completed for aeration radii between 4 and 6.7 m. The initial conditions used for the diffuser spacing study are the same as Table 4.3 The OTR and DO concentration for aeration radii between 4 and 6.7 m are illustrated in Figure 4.12.
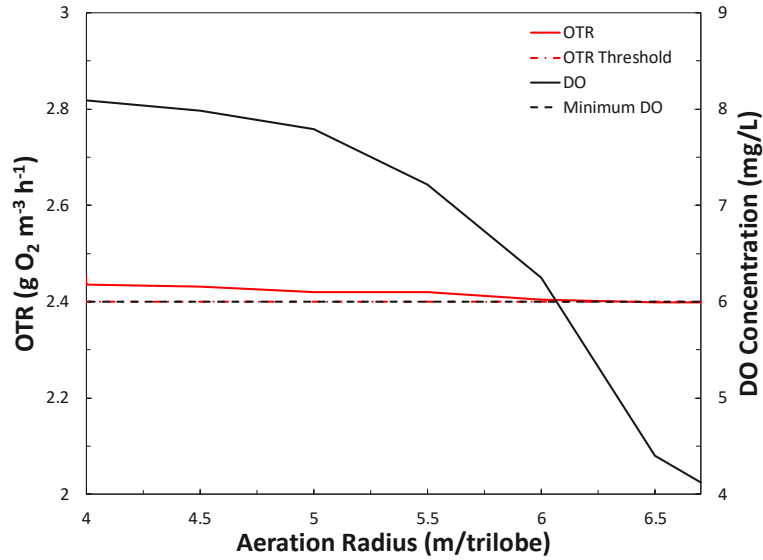
Figure 4.13: OTR and DO concentration for aeration radii between 4 and 6.7 m, and minimum OTR of 2.4 gO$_2$ m^{-3} h^{-1} and minimum DO of 6 mg/L

Based on a maximum air flow rate of 0.0254 m^3/s from a trilobed diffuser, the maximum aeration radius is approximately 6 m to meet the minimum OTR rate of 2.4 gO$_2$ m^{-3} h^{-1} and DO concentration of 6 mg/L. It should be noted that the OTR for aeration radii less than 6 m are slightly above the minimum of 2.4 gO$_2$ m^{-3} h^{-1} indicating the simulations were close but did not fully reach steady state. Therefore, to reach steady state it takes longer than 24 h for radii below 6 m. The number of trilobed diffusers required to meet the minimum OTR of 2.4 gO$_2$ m^{-3} h^{-1} and DO concentration of 6 mg/L for aeration radii between 4 and 6.7 m are illustrated in Figure 4.14.
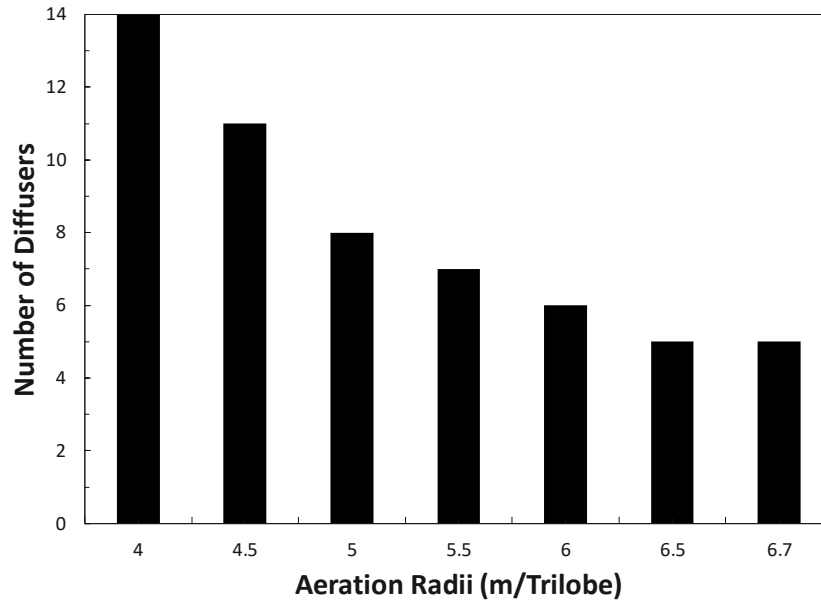
Figure 4.14: Number of trilobed diffusers required to meet the OTR threshold of 2.4 gO$_2$ m^{-3} h^{-1} and DO concentration of 6.0 mg/L for aeration radii between 4 and 6.7 m

Figure 4.14 shows that six trilobed diffusers are required to fully aerate a 30 m pen if each trilobed diffuser is aerating a 6 m radius. The estimated number of diffusers is one more than the recommended number provided by Pentair for an open-ocean pen 30 m in diameter and a maximum diffuser operational depth of 15 m (Pentair, 2018).

4.4.3 Flow Rate Case Study

Using an aeration radius of 6 m, the equivalent flow rates for O$_2$-enriched air concentrations of 40, 60, 80, and 95 mol% to meet the OTR threshold of 2.4 gO$_2$ m^{-3} h^{-1} and DO concentration of 6 mg/L were investigated. The initial conditions used in the flow rate case study are provided in Table 4.4.

Table 4.4: Initial Conditions for the Flow Rate Case Study

	Flow rate case study				
Variable	**0.0254 m³/s**	**0.00759 m³/s**	**0.00380 m³/s**	**0.00242 m³/s**	**0.00190 m³/s**
	(21% O₂)	**(40% O₂)**	**(60% O₂)**	**(80% O₂)**	**(95% O₂)**
$r_{p,0}$	1.00	1.00	1.00	1.00	1.00
u_0	0.849	0.556	0.435	0.370	0.339
T_0	293	293	293	293	293
$T_{b,0}$	293	293	293	293	293
S_0	34.0	34.0	34.0	34.0	34.0
$C_{O_2,0}$	0.188	0.188	0.188	0.188	0.188
$d_{b,0}$	0.001	0.001	0.001	0.001	0.001
Q_0	2.26	0.971	0.594	0.430	0.361
M_0	2.26	0.971	0.594	0.430	0.361
$\dot{N}_{l,0}$	0.425	0.183	0.112	0.0809	0.0679
$\dot{N}_{g,0}$	0.238	0.136	0.102	0.0864	0.0804

When using enriched air streams it is essential to know the O₂ uptake efficiency using

$$\text{O}_2 \text{ Uptake Efficiency} = \frac{\dot{V}_{std,in} y_{O_2,in} - \dot{V}_{std,out} y_{O_2,out}}{\dot{V}_{std,in} y_{O_2,in}} \qquad (4.16)$$

where $\dot{V}_{std,in}$ is the gas volumetric flow rate at the diffuser in standard conditions (m³/s), $\dot{V}_{std,out}$ is the gas volumetric flow rate leaving the top of the plume in standard conditions (m³/s), $y_{O_2,in}$ is the mol fraction of O₂ in the initial gas stream, and $y_{O_2,out}$ is the mol fraction of O₂ in the final gas stream. The equivalent air flow rates (m³/s) and the O₂ uptake efficiency for gas phase O₂ compositions between 21 and 95 mol% required to maintain a DO concentration of 6 mg/L in an aeration radius of 6 m are illustrated in Figure 4.15.
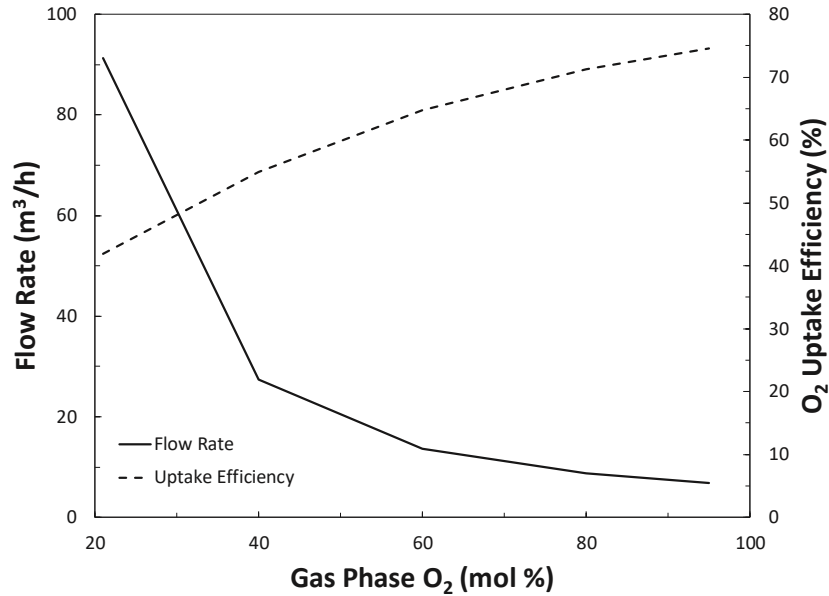
Figure 4.15: Equivalent air flow rates and O₂ uptake efficiency for gas phase O₂ compositions between 21 and 95 mol% to maintain a DO concentration of 6 mg/L in an aeration radius of 6 m

The required flow rate decreases significantly as the concentration of O_2 in the enriched air stream becomes larger, which is expected. The O_2 uptake efficiency increases while the O_2 concentration in the enriched air stream increases. The gas phase O_2 compositions between 21 and 95 mol% for various heights above the diffuser are illustrated in Figure 4.16.
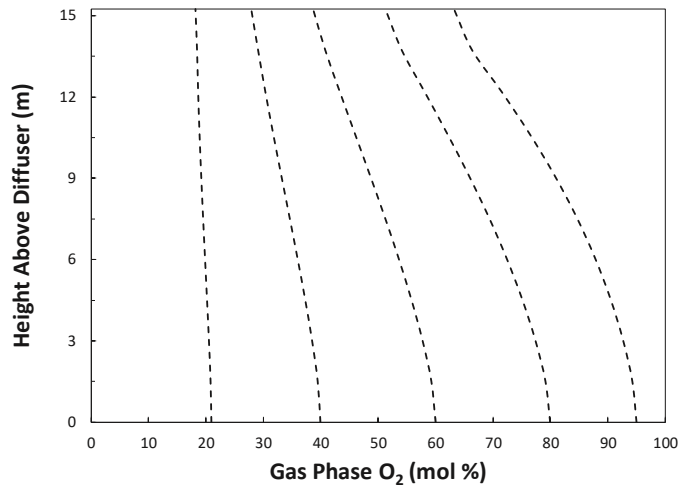
Figure 4.16: The gas phase O₂ composition between 21 and 95 mol% for various heights above the diffuser

4.4.4 Power Requirements of the Aeration System

To estimate the power requirements to aerate a 6 m aeration radius to a OTR threshold of 2.4 gO_2 m^{-3} h^{-1} and DO concentration of 6 mg/L, the total pressure drop (Pa) required for each of the flow rates at standard conditions is required. The pressure drop for the diffuser, the pressure drop for the length of piping between the compressor and diffuser, and the hydrostatic pressure at a depth of 15 m for the optimal flow rates of gas phase O_2 compositions between 21 and 95 mol% are provided in Table 4.5.

Table 4.5: Total Pressure Requirements for the Optimal Flow Rates of Gas Phase O_2 Compositions Between 21 and 95 mol%

Flow Rate (m³/h)	O_2 Composition (mol%)	Diffuser ΔP (kPa)	Pipe ΔP (kPa)	Hydrostatic Pressure (kPa)	Total Pressure (kPa)
6.83	95.0	1.89	0.0780	254	256
8.71	80.0	2.17	0.118	254	256
13.7	60.0	3.21	0.261	254	258
27.3	40.0	8.29	0.266	254	263
91.4	21.0	27.9	0.0376	254	281

Table 4.5 shows that the largest pressure drop occurs across the diffuser and decreases with decreasing gas flow rate. The largest minimum pressure requirement is seen at the highest air flow rate of 91.4 m³/h. Using the total pressure requirements, the compression and O_2 generation power can be estimated. The O_2 generator has an operating power requirement of 0.36 kW that is expected to be insignificant compared to the power required to compress the air feed. The power required to compress, and the power required to generate the O_2 for the optimal flow rates of gas phase O_2 compositions between 21 and 95 mol% are provided in Table 4.6.

Table 4.6: Total Power Required to Compress and Generate the Optimal Flow Rates of Gas Phase O_2 Compositions Between 21 and 95 mol%

Flow Rate (m³/h)	O_2 Composition (mol%)	Compression Power (kW)	O_2 Generator Power (kW)	Total Power (kW)
6.83	95.0	5.22	0.36	5.58
8.71	80.0	5.32	0.36	5.68
13.7	60.0	6.28	0.36	6.64
27.3	40.0	8.34	0.36	8.69
91.4	21.0	5.54	-	5.54

The largest power requirement to aerate a 6 m aeration radius to meet the OTR threshold of 2.4 gO_2 m^{-3} h^{-1} and DO concentration of 6 mg/L is a 40 mol% O_2 stream at a flow rate of 27.3 m^3/h. The power requirements for an air stream at 91.4 m^3/h is approximately equivalent to the power requirements for an 80 mol% O_2 stream at 8.71 m^3/h and a 95 mol% O_2 stream at 6.83 m^3/h. The required air and 95 mol% O_2 flow rates necessary to create the blended gas phase O_2 streams between 21 and 95 mol% are illustrated in Figure 4.17.
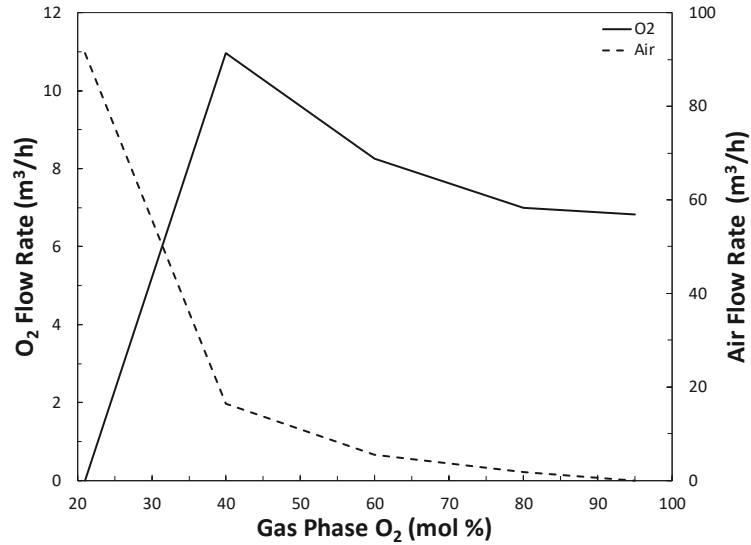
Figure 4.17: The required air and 95 mol% O_2 flow rates necessary to create the blended gas phase O_2 streams between 21 and 95 mol%

Figure 4.17 shows that the 40 mol% O_2 stream has a large power requirement because of the compression costs associated with generating the amount of 95 mol% O_2 required to blend with air to create a 40 mol% O_2 stream. The power lost by losing gaseous O_2 from the open-ocean pen (undissolved O_2 to atmosphere) can be estimated using

$$\dot{W}_L = \dot{W}_t(1 - O_2 \text{ Uptake Efficiency})$$

(4.17)

where $\dot{W}_L$ is the individual power loss in the system for one trilobed diffuser (kW), and $\dot{W}_t$ is the total power requirements one trilobed diffuser (kW). The total power and power lost for the different gas phase O_2 compositions are illustrated in Figure 4.18.

93
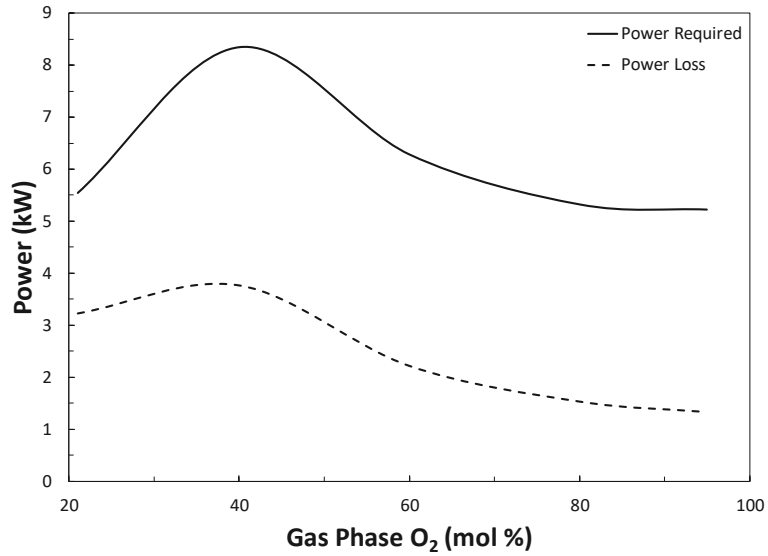
Figure 4.18: Power requirements and power loss for gas phase O₂ compositions between 21 and 95 mol%

The power requirements are almost identical for the air, 80 mol% O_2, and 95 mol% O_2 streams; however, the power loss is much less for the 80 and 95 mol% O_2 streams compared to the air stream. The aeration cost ($/kgO₂) for a 6 m aeration radius can be estimated using

$$E_c = E_r \dot{W}_I \tag{4.18}$$

where E_c is the energy cost ($/h), E_r is the energy rate ($/kWh), and $\dot{W}_I$ is the individual power requirement for one trilobed diffuser (kW). The average energy rate for Nova Scotia during the summer months (June to September) is $0.130/kWh (Nova Scotia Power, 2018). The aeration cost and the SAE for gas phase O_2 concentrations between 21 and 95 mol% at the minimum flow rate required to maintain DO concentration at 6 mg/L are illustrated in Figure 4.19.
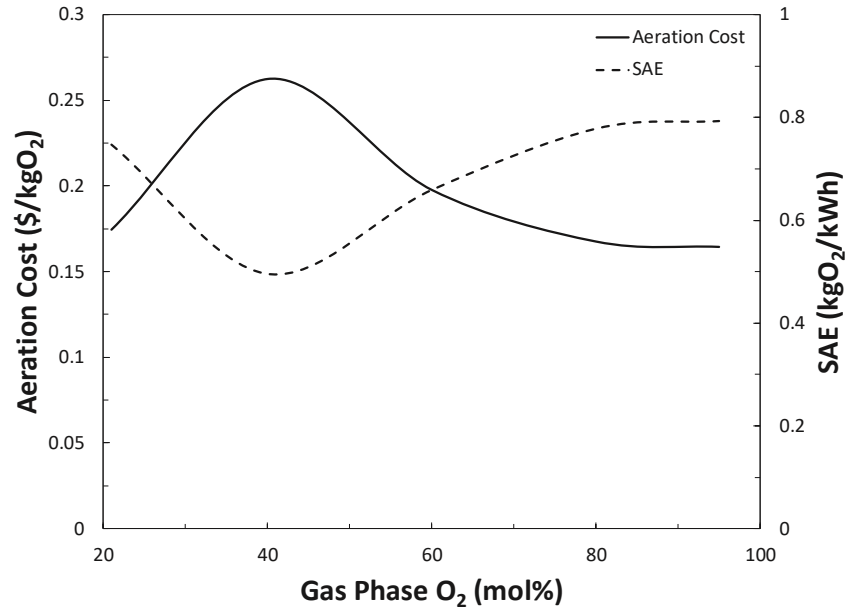
Figure 4.19: Aeration cost and SAE for gas phase O₂ concentrations between 21 and 95 mol% at the minimum flow rate for a 6 m aeration radius to maintain DO concentration at 6 mg/L

Note that as expressed in Figure 4.19, the SAE has been determined using the total energy requirement including compression and line losses, not just the energy dissipation across the aeration head. The SAE and the aeration cost for air, 80 mol% O_2, and 95 mol% O_2 streams are almost identical. To get the total cost of aeration in a 30 m diameter pen, Eq. 4.18 is multiplied by the number of diffusers required. For the case study, the number of diffusers required was determined to be six. It should be noted that the total aeration cost does not include the capital investment for the trilobed diffusers. The total aeration cost ($/h) for gas phase O_2 concentrations between 21 and 95 mol% at the equivalent air flow rates for a 30 m open-ocean pen to maintain a DO concentration at 6 mg/L are illustrated in Figure 4.20.
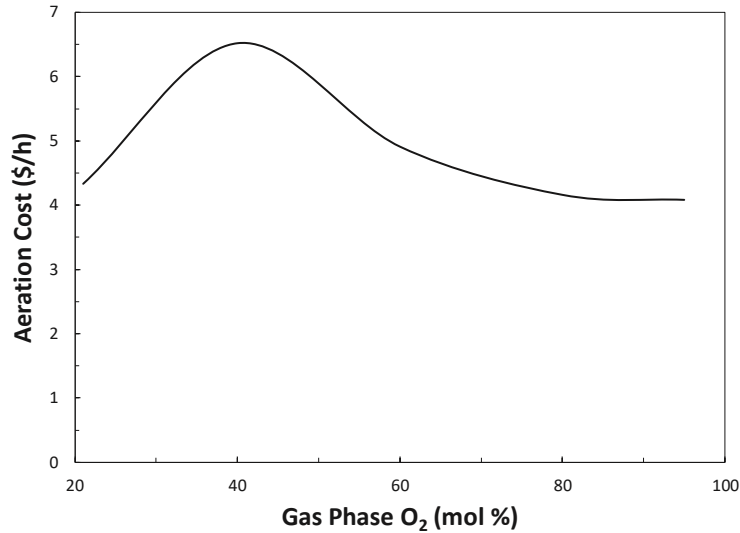
Figure 4.20: Aeration cost for the total number of diffusers required to maintain the DO concentration above 6 mg/L for O$_2$ concentrations between 21 and 95 mol% in a 30 m diameter open-ocean pen

4.5 Discussion

Using the validated model, a large-scale case study was completed to investigate the number of diffusers, the placement of diffusers, and the volume of air or O$_2$-enriched air required to keep the DO concentration in the open-ocean pens above the recommended minimum of 6 mg/L. The maximum spacing for a Pentair trilobed diffuser aerating at a maximum air flow rate of 0.0254 m^3/s to maintain a DO concentration at 6 mg/L with a DO consumption rate of 2 mgO$_2$ kgFish^{-1} min^{-1} by Atlantic salmon was found to be 6 m. If one trilobed diffuser can aerate a 6 m radius, then six trilobed diffusers would be needed to completely aerate a 30 m diameter and 15 m deep open-ocean pen. Using equivalent air flow rates for gas phase O$_2$ compositions between 40 and 95 mol% it was found that streams having 80 and 95 mol% O$_2$ required approximately the same amount of power and cost approximately the same as air on a dollar per hour basis. However, one limitation of the integral model is that it cannot predict whether any dissolved O$_2$ supersaturation zones occur. As discussed in Chapter 2, supersaturation can also have a detrimental effect on the health and wellbeing of Atlantic salmon. Additionally, generation of O$_2$ concentrations greater than 23 mol% should be carried out in a well-ventilated area with no fire hazards.

The use of air does appear able to provide sufficient aeration with increased numbers of diffusers, but cannot maintain OTR's significantly higher than 2.4 gO_2 $m^{-3}h^{-1}$ for a single an average DO concentration approaching 6 mg/L. This OTR rate is based on an average initial bubble size of 1mm and would reduce for larger bubble sizes introduced at the diffuser. Increasing the number of diffusers to 8 (aeration radius of 5 m) would provide additional capacity for management of increased biological oxygen demand or water exchange due to tidal flow. The increased gas volume present in aeration systems would also potentially provide greater entrainment-based flow of water through the thermocline, where colder waters have greater saturation capacity for dissolved oxygen.

The use of oxygen enriched strategies suggests that partial enrichment is not a favorable approach, with O_2 concentrations greater than 80 mol% preferred. Under these conditions, similar OTR's can be achieved at approximately 10% of the total nominal volumetric flow rate as air-based systems to each diffuser head, but with comparable inlet air volumetric flow rates and compression requirements due to the feed specifications and separation efficiency of the O_2 generators. Oxygen-enriched aeration does have the potential to enable higher OTR in emergency situations with less diffusers installed in the pens, but only if an over-sized O_2 generator and compressor chain is initially installed to manage these situations.

Due to the safety requirements inherent to oxygen-enriched systems, and the comparable energy demand relative to air-based systems, it is recommended that air be used for continuous aeration strategies with the option of installing additional diffusers, while Oxygen be limited to emergency aeration strategies or regions where total oxygen demand is expected to greatly exceed 2.4 gO_2 $m^{-3}h^{-1}$.

The coastal regions of Nova Scotia are prone to natural fluctuations in both water temperature and DO levels, which can have an impact on the health and growth of Atlantic salmon in open-ocean pens. The fluctuating temperature and DO level have created a need for mitigation strategies in the Nova Scotian aquaculture industry. An aeration system that allows for the delivery of supplemental O_2 to aquaculture pens during conditions of low DO has the potential to improve key performance indicators significantly, reduce episodic stress and mortality due to low O_2, and increase production efficiency, stability, and environmental sustainability of the aquaculture industry in Nova Scotia. The purpose of this dissertation was to develop heuristics for aerating Atlantic salmon open-ocean aquaculture pens during times of low DO (i.e., below 6 mg/L). The purpose of the dissertation was accomplished through the following objectives (1) identify key performance indicators to characterize the beneficial effects of O_2 supplementation for Atlantic salmon and parameters that will affect DO concentration in open-ocean pens, (2) evaluate technical approaches for efficiently distributing DO to open-ocean aquaculture pens, (3) develop a detailed model that can predict the hydrodynamics and mass transfer of bubble plumes generated by diffusers and validates the hydrodynamics and mass transfer using representative data, and (4) determine the best methods to maximize DO delivery through the timing of aeration, placement, and configuration of diffusers through detailed modeling.

The key performance indicators that characterize the beneficial effects of O_2 supplementation include DO and temperature. Dissolved O_2 and temperature are two of the most important environmental variables that determine every Atlantic salmon's environmental niche. The level of DO in seawater is dependent on several biological and chemical processes; however, photosynthesis is the primary source of DO in open-ocean pens. A minimum DO concentration of 6 mg/L is recommended for Atlantic salmon to protect them from adverse health effects such as acute stress responses, reduced feed conversion, and growth. Technical approaches for efficiently distributing DO to open-ocean aquaculture pens include surface and subsurface aeration systems. Fine bubble

diffusers are the recommended method for aerating in open-ocean pens because these diffusers have a high SAE compared to other methods, the diffusers are versatile and capable of delivering a range of low to high flow rates of both air and enriched air. The timing and placement of aeration and the use of air and O_2-enriched air were evaluated based on the need, the cost of compression, and the volume of gas required to reach the desired DO levels.

To predict the timing of aeration, the placement and number of diffusers required, and the volume of air or enriched air required to maintain a minimum DO concentration of 6 mg/L, a detailed model was developed. A bubble plume model using an integral approach was coupled with an ambient environment model and solved using a novel method in MATLAB® and Simulink®. The integral model differed from previous approaches by incorporating a relationship for the bubble terminal velocity as a function of the Schiller-Naumann drag coefficient and Lockett-Kirkpatrick swarm correction. The model was validated using hydrodynamic studies from Fanneløp & Sjøen (1980) and Milgram (1983), and mass transfer studies from DeMoyer et al. (2003) and Buscaglia et al. (2002).

Using the validated model, a large-scale case study was completed. The maximum spacing for a trilobed diffuser aerating at a maximum air flow rate of 0.0254 m^3/s to maintain a DO concentration at 6 mg/L with a DO consumption rate of 2 mgO_2 $kgFish^{-1}$ min^{-1} was found to be 6 m. An aeration radius of 6 m corresponds to six diffusers for a 30 m diameter pen. Using equivalent flow rates for gas phase O_2 compositions between 21 and 95 mol% it was found that 80 and 95 mol% O_2 required approximately the same power input and cost about the same in terms of \$/kg O_2 delivered. Based on safety concerns with respect to the generation of O_2 concentrations greater then 23 mol%, it is recommended that air be used to maintain a 30 m diameter, 15 m deep open-ocean pen at a DO concentration at 6 mg/L.

A transient one-dimensional bubble plume model coupled with an ambient environment mixing model is sufficiently accurate to develop heuristics for aeration in Atlantic salmon open-ocean aquaculture pens during times of low DO. The model is able to predict the number of diffusers, the placement of diffusers, and the volume of air or O_2-enriched air required to keep the DO concentration in Atlantic salmon open-ocean pens above the

recommended minimum of 6 mg/L. The heuristics for diffuser spacing, the number of diffusers required, and the use of air or O_2-enriched air will allow engineers and operators in the aquaculture industry to quickly make decisions on aeration and oxygenation. The developed model can also be applied to other applications of aeration and oxygenation or any application where there is a bubble plume release from a point source.

References

Applied Membranes Inc. (2018). *AMI membrane contactor degasifier systems* [Digital image]. Retrieved from https://www.appliedmembranes.com/degasifier-systems-membrane-contactors.html

Benson, B. B. & Krause, D. (1980). The concentration and isotopic fractionation of gases dissolved in freshwater in equilibrium with the atmosphere. *Limnology and Oceanography*, *25*(4), 662-671.

Benson, B. B. & Krause, D. (1984). The concentration and isotopic fractionation of oxygen dissolved in freshwater and seawater in equilibrium with the atmosphere. *Limnology and Oceanography*, *29*(3), 620-632.

Bergheim, A. & Fivelstad, S. (2014). *Atlantic Salmon (Salmo Salar L.) in aquaculture: Metabolic rate and water flow requirements* [PDF file]. Retrieved from https://www.researchgate.net/profile/Asbjorn_Bergheim3/publication/316619760_Atlantic_salmon_Salmo_salar_L_in_aquaculture_metabolic_rate_and_water_flow_requirements/links/59082a240f7e9bc0d59a885b/Atlantic-salmon-Salmo-salar-L-in-aquaculture-metabolic-rate-and-water-flow-requirements.pdf

Berillis, P., Mente, E., Nikoui, E., Makridis P., Grundvig, H., Bergheim, A., & Gausen, M. (2016). Improving aeration for efficient oxygenation in sea bass sea cages: Blood, brain and gill histology. *Open Life Sciences*, *11*, 270-279.

Buscaglia, G. C., Bombardelli, F. A., & Garcia, M. H. (2002). Numerical modeling of large-scale bubble plumes accounting for mass transfer effects. *International Journal of Multiphase Flow*, *28*, 1763-1785.

Chase, M. W. (1998). NIST-JANAF themochemical tables (4th ed.). *Journal of Physical Chemistry*, *9*, 1-1951.

Clift, R., Grace, J. R., & Weber, M. E. (1978). *Bubbles, drops, and particles*. New York, NY: Academic Press.

Crounse, B. C., Wannamaker, E. J., & Adams, E. E. (2007). Integral model of a multiphase plume in quiescent stratification. *Journal of Hydraulic Engineering*, *133*, 70-76.

Davidson, G. A. (1986). Gaussian versus top-hat profile assumptions in integral plume models. *Atmospheric Environment*, *20*(3), 471-478.

DeMoyer, C. D., Schierholz, E. L., Gulliver, J. S., & Wilhelms, S. C. (2003). Impact of bubble and free surface oxygen transfer on diffused aeration systems. *Water Research*, *37*, 1890-1904.

Department of Fisheries & Aquaculture. (2017). *Aquaculture*. Retrieved from
      https://novascotia.ca/fish/aquaculture/

Ditmars, J. D. & Cederwall, K. (1974). Analysis of air-bubble plumes. *In proceedings,
      14th Coastal Engineering Conference*, Copenhagen.

Dymond, J. H & Smith, E. B. (1980). *The virial coefficients of pure gases and mixtures:
      A critical compilation*. Oxford, UK: Clarendon Press.

EPA. (1999). *Wastewater technology fact sheet: Fine bubble aeration*. Retrieved from
      https://www3.epa.gov/npdes/pubs/fine.pdf

Espmark, A. M., Hjelde, K., & Baevefjord, G. (2010). Development of gas bubble
      disease in juvenile Atlantic salmon exposed to water supersaturated with oxygen.
      Aquaculture, *306*(4), 198-204.

Fanneløp, T. K. & Bettelini, M. (2007). Very large deep set bubble plume from broken
      gas pipelines. *Engineering and Environmental Flow Analysis*, *11*, 270-279.

Fanneløp, T. K. & Sjøen, K. (1980). Hydrodynamics of underwater blowouts. *In
      Proceedings of AIAA 18th Aerospace Science Meeting*.

FAO. (2017). *Salmo Salar*. Retrieved from http://www.fao.org/fishery/cultured
      species/Salmo_salar/en

Fisheries Research Services. (2005). *Scottish fish farms annual production survey* [PDF
      file]. Retrieved from www.marlab.ac.uk

Fraga, B. & Stoesser, T. (2016). Influence of bubble size, diffuser width, and flow rate on
      the integral behavior of bubble plumes. *Journal of Geophysical Research Oceans*,
      121, 3887-3904.

Fresh by Design. (2016). *Oxygen cone* [Digital image]. Retrieved from https://freshbydes
      ign.com.au/aquaponic-aquaculture-products/oxygen-ozone/oxygen-cone/

Gardner Pinfold. (2016). *Socio-economic impact of aquaculture in Canada* [PDF file].
      Retrieved from http://www.dfo-mpo.gc.ca/aquaculture/sector-secteur/socio/index
      -eng.htm

Hughmark, G. A. (1967). Liquid-liquid spray column drop size, holdup, and continuous
      phase mass transfer. *Industrial and Engineering Chemistry Fundamentals*, *6*, 408-
      413.

Isdale, J. D., Spence, C.M., & Tudhope, J. S. (1972). Physical properties of sea water
      solutions: Viscosity. *Desalination, 10*(4), 319–328.

Johansen, O. (2000). DeepBlow: A lagrangian plume model for deep-water blowouts. *Spill Science and Technology*, *6*, 103-111.

Kirkpatrick, R. D. & Lockett, M. J. (1974). The influence of approach velocity on bubble coalescence. *Chemical Engineering Science*, *29*(12), 2363-2373.

Kumar, A, Moulick, S., & Chandra Mal, B. (2013). Selection of aerators for intensive aquacultural pond. *Aquacultural Engineering*, *56*, 71-78.

Lawson, T. B. (2012). *Fundamentals of aquacultural engineering*. Norwell, Ma: Kluwer Academic Publishers.

Li, Y. H. & Gregory, S. (1974). Diffusion of ions in sea water and in deep-sea sediments. *Geochimica et Cosmochimica Acta*, *38*, 703-714.

Lima Neto, I. E. (2012). Bubble plume modelling with new functional relationships. *Journal of Hydraulic Research*, *50*(1), 134-137.

Lima Neto, I. E. & Parente, P. A. B. (2016). Influence of mass transfer on bubble plume hydrodynamics. *Annals of the Brazilian Academy of Sciences*, *88*(1), 411-422.

McCabe, W. L., Smith, J. C., & Harriott, P. (2004). *Unit operations of chemical engineering* (7th ed.). New York, NY: McGraw-Hill.

McGinnis, D. F. & Little, J. C. (1998). Bubble dynamics and oxygen transfer in a Speece cone. *Water Science Technology*, *37*(2), 285-292.

Milgram, J. H. (1983). Mean flow in round bubble plumes. *Journal of Fluid Mechanics*, *133*, 345-376.

Morton, B. R., Taylor, G., & Turner, J. S. (1956). Turbulent gravitational convection from maintained and instantaneous sources. *Proceedings of The Royal Society of London*, A234, 1-23.

National Oceanic and Atmospheric Administration. (2018). *Ocean Coasts*. Retrieved from http://www.noaa.gov/oceans-coasts

Nayar, K. G., Sharqawy, M. H., Banchik, L. D., & Lienhard, J. H. (2016). Thermophysical properties of seawater: A review and new correlations that include pressure dependence. *Desalination*, *390*, 1-24.

Nayar, K. G., Sharqawy, M. H., & Lienhard, J. H. (2016). *Seawater thermophysical properties library*. Retrieved from http://web.mit.edu/seawater

Nova Scotia Power. (2018). *Time-of-day rates*. Retrieved from
https://www.nspower.ca/en/home/for-my-home/heating-solutions/electric-
thermal-storage/tod-rates/default.aspx

Olsen, J. E., Skjetne, P., & Johansen, S. T. (2017). VLES turbulence model for a
Eulerian-Lagrangian modeling concept for bubble plumes. *Applied Mathematical
Modelling*, *44*, 61-71

Oppedal, F., Dempster, T., & Stien, L. H. (2010). Environmental drivers of Atlantic
salmon behaviour in sea-cages: A review. *Aquaculture*, *311*, 1-18.

OxyVision. (2018). *AirX: A new diffuser hose for adding air to water* [Digital image].
Retrieved from http://www.oxyvision.com/index.php/airx

Pentair. (2018a). *FlexAir® 9″ disc air diffuser* [Digital image]. Retrieved from
https://pentairaes.com/flexairr-9-disc-diffuser.html

Pentair. (2018b). *Paddlewheel aerators for aquaculture and wastewater* [Digital image].
Retrieved from https://pentairaes.com/paddlewheel-aerators-for-aquaculture-
waste-water.html

Peters, M. S., Timmerhaus, K. D., & West, R. E. (2003). *Plant design and economics for
chemical engineers*. New York, NY: McGraw-Hill.

Ramsing, N. & Gundersen, J. (n.d.). *Seawater and gases: Tabulated physical parameters
of interest to people working with microsensors in marine systems* [PDF file].
Retrieved from http://www.unisense.com/files/PDF/Diverse/Seawater%20&%20
Gases%20table.pdf

Ranz, W. E. & Marshall, W. R. (1952). Evaporation from drops. *Chemical Engineering
Progress*, *48*(3), 141-146.

Rao, P. & Muller, M. (2007). Industrial oxygen: Its generation and use. *American
Council for an Energy-Efficient Economy, Summer Study on Energy Efficiency in
Industry*.

Royal Society for the Prevention of Cruelty to Animals. (2017). *Farmed Atlantic salmon:
Information notes* [PDF file]. Retrieved from
https://rspcaapproved.org.au/wpcontent/uploa ds/2017/03/2017-
03_SALMON_InformationNotes.pdf

Sander, R. (2015). Compilation of Henry's law constants for water as a solvent (4th ed.).
Atmospheric Chemistry and Physics, *15*, 4399-4981.

Schiller, V. L. & Naumann, A. (1933). Über die grundlegenden Berechnungen bei der
Schwerkraft aufbereitung. *ZVDI*, *77*, 318-320.

Shampine, L. F., Reichelt, M. W., & Kierzenka, J. A. (1999). Solving Index-1 DAEs in MATLAB and Simulink. *Society for Industrial and Applied Mathematics Review*, *41*, 538–552.

Sharqawy, M. H. (2013). New correlations for seawater and purewater thermal conductivity at different temperatures and salinities. *Desalination*, *313*, 97–104.

Sharqawy, M. H., Lienhard, J. H., & Zubair, S. M. (2010). Thermophysical properties of seawater: A review of existing correlations and data. *Desalination and Water Treatment*, *16*, 354-380.

Singleton, V. L. & Little, J. C. (2006). Designing hypolimnetic aeration and oxygenation systems: A review. *Environmental Science & Technology*, *40*(24), 7512-7520.

Smith, A. R. & Klosek, J. (2001). A review of air separation technologies and their integration with energy conversion processes. *Fuel Processing Technology*, *70*, 115-134.

Stevenson, P. (2007). *Closed waters: The welfare of farmed Atlantic salmon, rainbow trout, Atlantic cod, and Atlantic halibut* [PDF file]. Retrieved from https://www.ciwf.org.uk/media/ 3818650/closed-waters-welfare-of-farmed-atlantic-salmon.pdf

The Oxygen Store. (2018). AirSep AS-L PSA oxygen generator. Retrieved from https://www.theoxygenstore.com/airsep-as-l-oxygen-generator.html

United Nations. (2015). *World population projected to reach 9.7 billion by 2050*. Retrieved from http://www.un.org/en/development/desa/news/population/ 2015-report.html

University of California. (2018). *Lifecycle of the salmon* [Digital image]. Retrieved from http://sns.ucdavis.edu/public/user/images/lifecycle_of_salmon.jpg

Water Online. (2018). *PMSL's Raptor™ directional aeration system* [Digital image]. Retrieved from https://www.wateronline.com/doc/pmsls-raptor-directional-aeration -system-0001

Weiss, R. F. (1970). The solubility of nitrogen, oxygen and argon in water and seawater. *Deep-Sea Research*, *17*, 721-735.

Whitman, W. G. (1923). The two-film theory of gas absorption. *Chemical and Metallurgical Engineering*, *29*(4), 146-148.

Wüest, A., Brooks, N. A., & Imboden, D. M. (1992). Bubble plume modeling for lake restoration. *Water Resources Research, 28*(12), 3235-3250.

Yapa, P. D. & Chen, F. (2004). Behaviour of oil and gas from deepwater blowouts. *Journal of Hydraulic Engineering*, *130*, 540-553.

Yaws, C. L. (2009). *Yaws' Handbook of Antoine coefficients for vapor pressure* (2nd ed.). New York, NY: McGraw-Hill.

Yaws, C. L. (2015). *Yaws' Handbook of Thermodynamic and Physical Properties of Chemical Compounds*. New York, NY: McGraw-Hill

Appendix A: Property Correlations

Weiss (1970) proposed a set of equations to compute oxygen solubility in water as a function of temperature and salinity. The Weiss (1970) equations were based on the best measurements of DN solubility available at the time according to

$$[\text{DN}] = DN_0 F_s F_p \tag{A1}$$

where the DN concentration (mg/L) is represented as a baseline concentration in freshwater (DN_0) multiplied by a salinity correction factor (F_s) and a pressure correction factor (F_p). The Weiss (1970) baseline DN concentration at 0 salinity and 101 325 Pa can be evaluated using

$$
\begin{aligned}
DN_0 = \rho_{N_2} \Big[&-172.4965 + 248.4262 \left(\frac{100}{T} \right) + 143.0738 \ln \left(\frac{T}{100} \right) \\
&- 21.712 \left(\frac{T}{100} \right) \Big]
\end{aligned}
\tag{A2}
$$

where T is the water temperature (K), and ρ_{N_2} is the density of N$_2$ at standard conditions (kg/m^3). The Weiss salinity factor can be evaluated using

$$F_S = e^{\left\{ S \left[-0.049781 + 0.025018 \left(\frac{T}{100} \right) - 0.0034861 \left(\frac{T}{100} \right)^2 \right] \right\}} \tag{A3}$$

where S is the salinity (g/kg) and T is water temperature (K). This salinity factor was derived with the assumption that the dissolved ions in the water are identical to those present in seawater using

$$F_P = \frac{P - P_w}{760 - P_w} \tag{A4}$$

where P is the barometric pressure (Pa) and P_w is the vapour pressure of water (Pa). The vapour pressure of water can be estimated using the Antoine equation according to

$$P_w = e^{\left[11.8571 - \frac{3840.70}{T} - \frac{216961}{T^2} \right]} \tag{A5}$$

The solubility equations for N_2 apply to a temperature range between 273 and 313 K, a salinity range between 0 and 40 g/kg, and a pressure range of 50 662 to 111 457 Pa (Weiss, 1970).

Thermophysical properties of seawater as functions of temperature, salinity, and pressure are calculated using correlations from Nayar et al. (2016). The density of seawater (ρ_{sw}) as a function of temperature, salinity, and pressure can be calculated using

$$\rho_{sw}(T, S, P) = \rho_{sw}(T, S, P_o)F_P \tag{A6}$$

where T is temperature (K), S is salinity (g/kg), P_o is atmospheric pressure (Pa), F_P is the pressure factor to account for increasing water depth, $\rho_{sw}(T, S, P_o)$ is the density of seawater at standard conditions. The density of seawater at standard conditions can be calculated using

$$\begin{aligned}
\rho_{sw}(T, S, P_o) = &(a_1 + a_2(T - 273.15) + a_3(T - 273.15)^2 + a_4(T - 273.15)^3 \\
&+ a_5(T - 273.15)^4) \\
&+ (b_1 S + b_2 S(T - 273.15) + b_3 S(T - 273.15)^2 \\
&+ b_4 S(T - 273.15)^3 + b_5 S^2(T - 273.15)^2)
\end{aligned} \tag{A7}$$

where a_1, a_2, a_3, a_4, a_5, b_1, b_2, b_3, b_4, and b_5 are empirical constants (Table A1) developed by Nayar et al. (2016). The pressure factor can be calculated using

$$F_P = \exp\left(\int_{P_o}^{P} \kappa_{T,sw} \, dP\right) \tag{A8}$$

where $\kappa_{T,sw}$ is the isothermal compressibility of seawater (MPa). The pressure factor can be expanded to

$$F_P = \exp\left[(P - P_o) + \left(\begin{array}{c} c_1 + c_2 t + c_3 t^2 + c_4 t^3 + c_5 t^4 + c_6 t^5 \\ + S(d_1 + d_2 t + d_3 t^2) \end{array} \right) + \frac{P^2 + P_o^2}{2}(c_7 + c_8 t + c_9 t^3 + d_4 S) \right] \tag{A9}$$

where c_1, c_2, c_3, c_4, c_5, c_6, c_7, c_8, c_9, d_1, d_2, d_3, and d_4 are empirical constants (Table A1) developed by Nayar et al. (2016).

Table A1: Temperature, Salinity, and Pressure Dependent Seawater Density Correlation Empirical Constants

$a_1 = 9.999 \times 10^2, a_2 = 2.034 \times 10^{-2}, a_3 = -6.162 \times 10^{-3}, a_4 = 2.261 \times 10^{-5},$

$a_5 = -4.657 \times 10^{-8}$

$b_1 = 8.020 \times 10^2, b_2 = -2.001, b_3 = 1.677 \times 10^{-2}, b_4 = -3.060 \times 10^{-5}, b_5 = -1.613 \times 10^{-5}$

$c_1 = 5.0792 \times 10^{-4}, c_2 = -3.4168 \times 10^{-6}, c_3 = 5.6931 \times 10^{-8}, c_4 = -3.7263 \times 10^{-10},$

$c_5 = 1.4465 \times 10^{-12}, c_6 = -1.7058 \times 10^{-15}, c_7 = -1.3389 \times 10^{-6}, c_8 = 4.8603 \times 10^{-9},$

$c_9 = -6.8039 \times 10^{-13}$

$d_1 = -1.1077 \times 10^{-6}, d_2 = 5.5584 \times 10^{-9}, d_3 = -4.2539 \times 10^{-11}, d_4 = 8.3702 \times 10^{-9}$

The temperature, salinity, and pressure dependent seawater density correlation (Eq. A6) is valid for temperatures of 273.15 to 453.15 K, salinities of 0 to 160 g/kg, and pressures of 0 to 12 MPa. The maximum uncertainty of Eq. A6 in the region of experimental data is 0.14%. The density of seawater for salinities between 0 and 30 g/kg and a temperature range of 273.15 to 303.15 K is illustrated in Figure A1 and validated with data sets from Nayar et al. (2016).
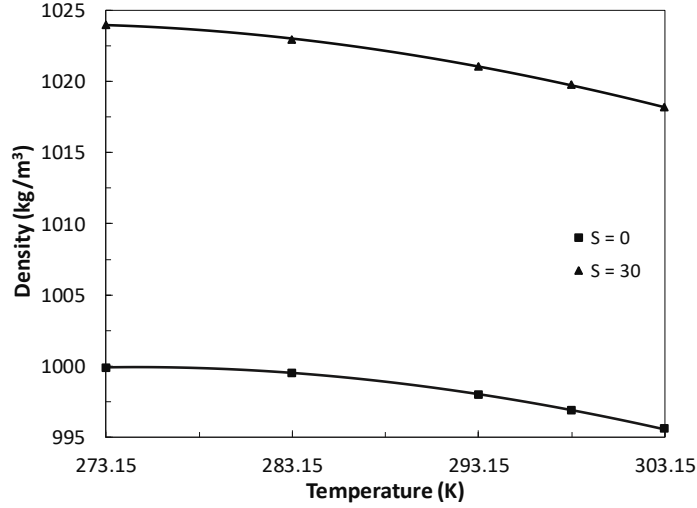
Figure A1: Density of seawater for salinities of 0 and 30 g/kg and a temperature range of 273.15 to 303.15 K and validated with data sets from Nayar et al. (2016).

The dynamic viscosity of seawater (μ) as a function of temperature and salinity (Isadale, Spence & Tudhope, 1972) can be calculated using

$$\mu = \mu_w(1 + AS + BS^2) \tag{A10}$$

where μ_w is the viscosity of pure water at standard conditions (Pa s), S is salinity (g/kg), and A and B are empirical correlations (Table A2). The pure water dynamic viscosity (0 salinity) developed by Dorsey (1940) can be calculated using

$$\mu_w = a_4 + \frac{1}{a_1(T + a_2)^2 + a_3} \tag{A11}$$

where T is temperature (K) and a_1, a_2, and a_3 are empirical constants (Table A2).

Table A2: Temperature and Salinity Dependent Dynamic Viscosity Correlation Empirical Constants

| |
|---|
| $A = a_5 + a_6T + a_7T^2$ |
| $B = a_8 + a_9T + a_{10}T^2$ |
| $a_1 = 1.5700 \times 10^{-1}, a_2 = 6.4993 \times 10^1, a_3 = -9.1296 \times 10^1, a_4 = 4.2844 \times 10^{-5}$, |
| $a_5 = 1.5409$, |
| $a_6 = 1.9981 \times 10^{-2}, a_7 = -9.5204 \times 10^{-5}, a_8 = 7.9739, a_9 = -7.5614 \times 10^{-2}$, |
| $a_9 = 4.7237 \times 10^{-4}$ |

The temperature and salinity dependent dynamic viscosity (Eq. A10) is valid for temperatures of 273.15 to 453.15 K, salinities of 0 to 150 g/kg, and pressures of 0.2 to 12 MPa. The maximum uncertainty of the correlation in the region of experimental data is ±1.50%. The dynamic viscosity of seawater for salinities of 0 and 30 g/kg and a temperature range of 273.15 to 303.15 K is illustrated in Figure A2 and validated with data sets from Nayar et al. (2016).
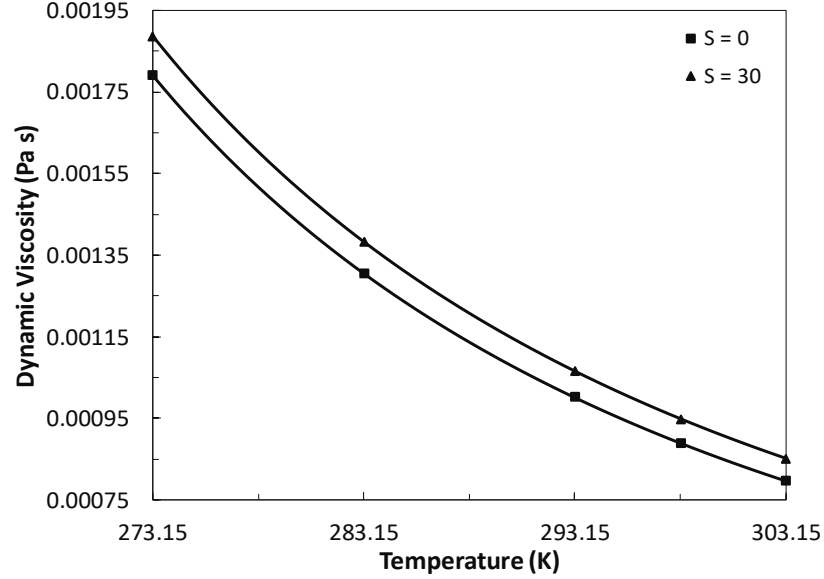
Figure A2: Dynamic viscosity of seawater for salinities of 0 and 30 g/kg and a temperature range of 273.15 to 303.15 K and validated with data sets from Nayar et al. (2016)

The specific heat capacity of seawater ($c_{P,sw}$) as a function of temperature, salinity, and pressure can be calculated using

$$
\begin{aligned}
c_{P,sw}(T, S, P) =\ & c_{P,sw}(T, S, P_o) \\
& + (P - P_o)\big(a_1 + a_2(T - 273.15) + a_3(T - 273.15)^2 \\
& + a_4(T - 273.15)^3 \\
& + S(a_5 + a_6(T - 273.15) + a_7(T - 273.15)^2 \\
& + a_8(T - 273.15)^3)\big)
\end{aligned}
\tag{A12}
$$

where T is temperature (K), S is salinity (g/kg), P_o is atmospheric pressure (Pa), P is pressure (Pa), $c_{P,sw}(T, S, P_o)$ is the specific heat capacity of seawater at standard

conditions, and a_1, a_2, a_3, a_4, a_5, a_6, a_7, a_8 are empirical constants (Table A3). The specific heat capacity of seawater at standard conditions can be calculated using

$$c_{P,sw}\,(T,S,P_o) = A + BT + CT^2 + DT^3 \qquad \text{(A13)}$$

where A, B, C, and D are empirical correlations (Table A3).

Table A3: Temperature, Salinity, and Pressure Dependent Specific Heat Capacity Empirical Constants and Correlations

$a_1 = 9.999 \times 10^2, a_2 = 2.034 \times 10^{-2}, a_3 = -6.162 \times 10^{-3}, a_4 = 2.261 \times 10^{-5},$

$a_5 = -4.657 \times 10^{-8}, a_6 = 8.020 \times 10^2, a_7 = -2.001, a_8 = 1.677 \times 10^{-2}$

$A = 5328 - 9.76 \times 10^1 S + 4.04 \times 10^{-1} S^2$

$B = -6.913 + 7.351 \times 10^{-1} S + 3.15 \times 10^{-3} S^2$

$C = 9.6 \times 10^{-3} - 1.927 \times 10^{-3} S + 8.23 \times 10^{-6} S^2$

$D = 2.5 \times 10^{-6} + 1.666 \times 10^{-6} S - 7.125 \times 10^{-9} S^2$

The temperature, salinity, and pressure dependent specific heat capacity (Eq. A12) is valid for temperatures of 273.15 to 313.15 K, salinities of 0 to 42 g/kg, and pressures of 0.2 to 12 MPa. The maximum uncertainty of the correlation in the region of experimental data is ±1.00%. The specific heat capacity of seawater for salinities of 0 and 30 g/kg and a temperature range of 273.15 to 303.15 K is illustrated in Figure A3 and validated with data sets from Nayar et al. (2016).
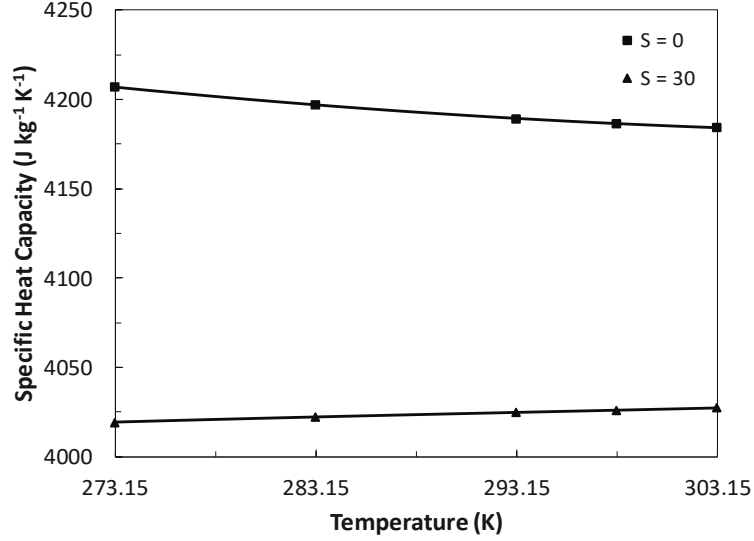
Figure A3: Specific heat capacity of seawater for salinities of 0 and 30 g/kg and a temperature range of 273.15 to 303.15 K and validated with data sets from Nayar et al. (2016)

The thermal conductivity of seawater (k_{SW}) as a function of temperature, salinity, and pressure (Sharqaway, 2013) can be calculated using

$$k_{SW}(T,S,P) = \frac{k_w(T,P)}{1 + 0.00022S} \tag{A14}$$

where T is temperature (K), S is salinity (g/kg), P is pressure (Pa), $k_w(T,P)$ is the thermal conductivity of fresh water (W m^{-1} K^{-1}) developed by Sharqaway (2013). The thermal conductivity of fresh water (Sharqaway, 2013) can be calculated using

$$k_w(T,P) = k_w(T,P_o)\left[1 + P^*\left(a_1 + a_2T^* + a_3T^{*2} + a_4T^{*3} + a_5T^{*4}\right)\right] \tag{A15}$$

where P_o is atmospheric pressure (Pa), T^* is a dimensionless temperature given by $\frac{T}{300}$, P^* is a dimensionless pressure given by $\frac{P-0.1}{139.9}$, $k_w(T,P_o)$ is the thermal conductivity (W m^{-1} K^{-1}) of fresh water at standard conditions, and a_1, a_2, a_3, a_4, and a_5 are empirical constants (Table A4). The thermal conductivity of fresh water at standard conditions can be calculated using

$$k_w(T,P_o) = b_1T^{*-0.194} + b_2T^{*-4.717} + b_3T^{*-6.385} + b_4T^{*-2.134} \tag{A16}$$

113

where b_1, b_2, b_3, and b_4 are empirical constants (Table A4).

Table A4: Temperature, Salinity, and Pressure Dependent Thermal Conductivity Constants and Correlations

$a_1 = 21.942, a_2 = -77.387, a_3 = 102.81, a_4 = -60.727, a_5 = 13.464$

$b_1 = 0.797015, b_2 = -0.251242, b_3 = 0.096437, b_4 = -0.032696$

Range of validity (±2.57%)

$0 \leq t \leq 60°C; \ 0 \leq S \leq 35 \ g/kg; \ 0.1 \leq P \leq 12 \ MPa$

The temperature, salinity, and pressure dependent thermal conductivity (Eq. A14) is valid for temperatures of 273.15 to 333.15 K, salinities of 0 to 35 g/kg, and pressures 0.1 to 12 MPa. The maximum uncertainty of the correlation in the region of experimental data is ±2.57%. The thermal conductivity of seawater for salinities of 0 and 30 g/kg and a temperature range of 283.15 to 303.15 K is illustrated in Figure A4 and validated with data sets from Nayar et al. (2016).
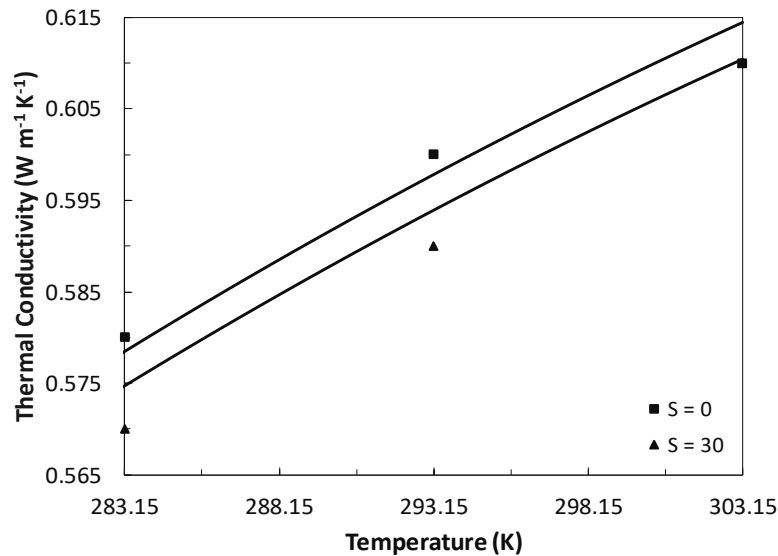
Figure A4: Thermal conductivity of seawater for salinities of 0 and 30 g/kg and a temperature range of 283.15 to 303.15 K

Thermophysical properties of O_2 and N_2 gas as functions of temperature and pressure are calculated using correlations from Yaws (2015) and Yaws (2014). The specific heat capacity (C_p) of O_2 and N_2 can be calculated using Eq. A17 and Eq. A18 respectively.

$$C_{p,O_2} = A + BT_b + CT_b^2 + DT_b^3 \tag{A17}$$

$$C_{p,N_2} = A + BT_b + CT_b^2 + DT_b^3 \tag{A18}$$

where T_b is the bubble temperature (K) and A, B, C, and D are empirical constants (Table A6).

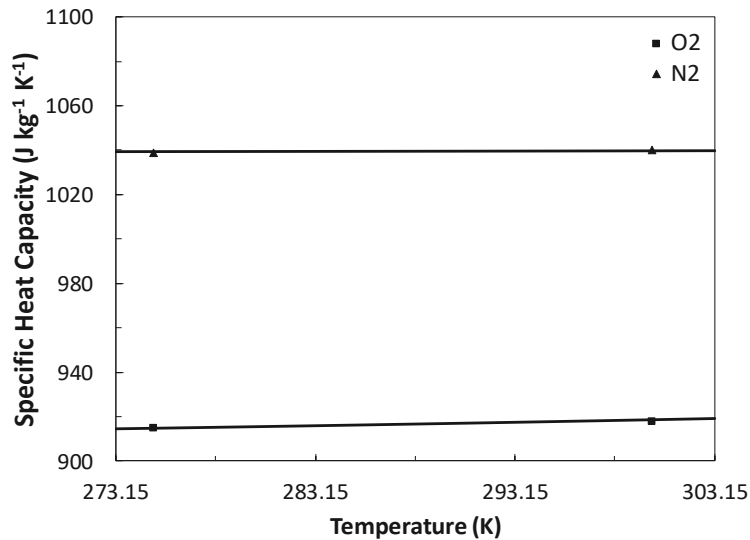**Table A6: Oxygen and Nitrogen Property Correlations for Specific Heat Capacity**

O_2 specific heat capacity:

$A = 2.910 \times 10^{-2}; B = 1.158 \times 10^{-5}; C = -6.076 \times 10^{-9}; D = 1.311 \times 10^{-12}$

N_2 specific heat capacity:

$A = 2.900 \times 10^{-2}; B = 2.199 \times 10^{-6}; C = 5.723 \times 10^{-9}; D = -2.871 \times 10^{-12}$

The O_2 and N_2 specific heat capacity polynomials are valid for temperatures of 150 to 1500 K. The O_2 and N_2 specific heat capacity for a temperature range of 273.15 to 303.15 K is illustrated in Figure A7 and validated with data from Yaws (2015).

Figure A7: Oxygen and nitrogen specific heat capacity for temperature range of 273.15 to 303.15 K validated with data from Yaws (2015)

The dynamic viscosity (μ) of O_2 and N_2 can be calculated using the polynomials in Eq. A19 and Eq. A20 respectively

$$\mu_{,O_2} = A + BT_b + CT_b^2 + DT_b^3 \tag{A19}$$

$$\mu_{,N_2} = A + BT_b + CT_b^2 + DT_b^3 \tag{A20}$$

where T_b is temperature (K) and A, B, C, and D are empirical constants (Table A7).

**Table A7: Oxygen and Nitrogen Property Correlations for Viscosity**

O_2 viscosity:

$A = -4.943; B = 0.8067; C = -4.042 \times 10^{-4}; D = 1.011 \times 10^{-7}$

N_2 viscosity:

$A = 4.466; B = 0.6381; C = -2.660 \times 10^{-4}; D = 5.411 \times 10^{-8}$

The O_2 and N_2 dynamic viscosity polynomials are valid for temperatures of 54 to 1500 K. The O_2 and N_2 dynamic viscosity for a temperature range of 273.15 to 303.15 K is illustrated in Figure A8 and validated with data from Yaws (2014).
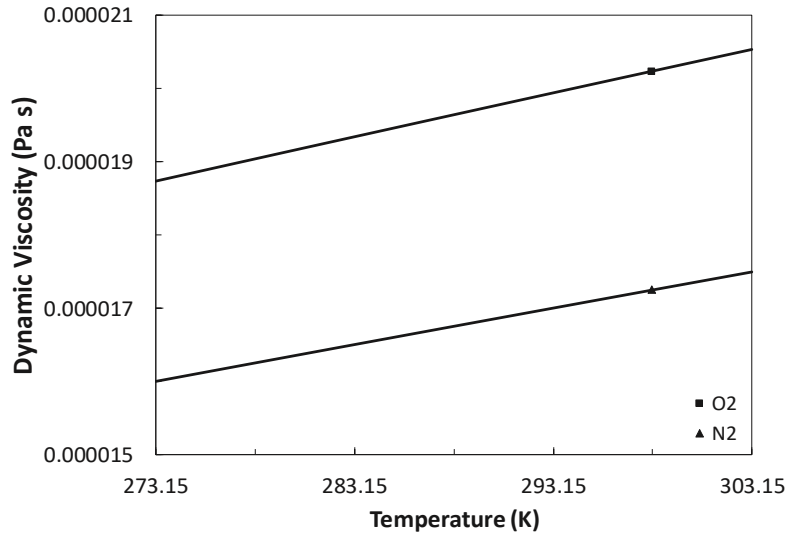
Figure A8: Oxygen and nitrogen dynamic viscosity for temperature range of 273.15 to 303.15 K validated with data from Yaws (2014)

The density (ρ) of O_2 and N_2 can be calculated by using the ideal gas law with a compressibility factor that is a correction factor that describes the deviation of the gas from ideal behavior by

$$PV = ZnRT \tag{A21}$$

where P is pressure (Pa) of the gas, V is volume (m³) of the gas, Z is the compressibility factor (dimensionless), n is amount of gas (moles), R is the universal gas constant (Pa m³ K⁻¹), and T is temperature (K). The ideal gas law can be rearranged by using $n = \frac{m_g}{MW}$ where m_g is the total mass of the gas (kg) and MW is the molecular weight of the gas (kg/mole). The compressibility factor of O_2 and N_2 mixture are negligible at the pressure in this work; therefore, it can be ignored for the purposes of these calculations. The ideal gas law can further be arranged by $\rho = \frac{m_g}{V}$ providing Eq. A22 and Eq. A23 respectively.

$$\rho_{O_2} = \frac{P}{RT_b MW_{O_2}} \tag{A22}$$

$$\rho_{N_2} = \frac{P}{RT_b MW_{N_2}} \tag{A23}$$

The O_2 and N_2 density for temperature range of 273.15 to 303.15 K is illustrated in Figure A9 and validated with data from Yaws (2015).
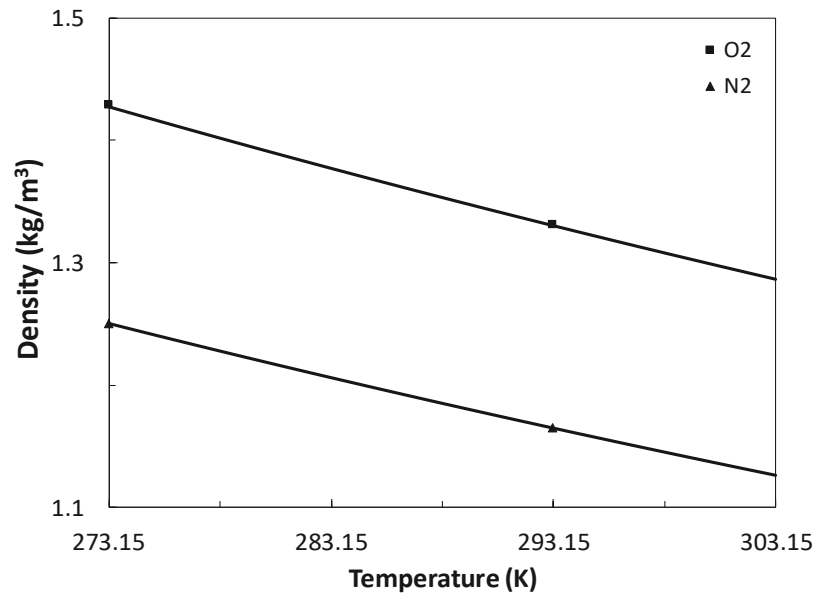
Figure A9: Oxygen and nitrogen density for temperature range of 273.15 to 303.15 K validated with data from Yaws (2015)